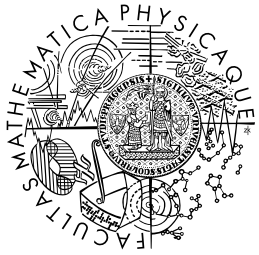

FACULTY
OF MATHEMATICS
AND PHYSICS
Charles University

MASTER THESIS

Lucia Mravcová

Multi-wavelength study of white-light flares

Astronomical Institute of Charles University

Supervisor of the master thesis:	doc. Mgr. Michal Švanda, Ph.D.
Advisor of the master thesis:	Mgr. Jana Kašparová, Ph.D.
Study programme:	Physics
Study branch:	Astronomy and Astrophysics

Prague 2019

I declare that I carried out this master thesis independently, and only with the cited sources, literature and other professional sources.

I understand that my work relates to the rights and obligations under the Act No. 121/2000 Sb., the Copyright Act, as amended, in particular the fact that the Charles University has the right to conclude a license agreement on the use of this work as a school work pursuant to Section 60 subsection 1 of the Copyright Act.

In ..... date ..... signature of the author

I would like to thank my supervisor Michal Švanda and my advisor Jana Kašparová for their comments, insights, and the time that they invested. I would also like to thank my friends and family who supported me during my master studies.

Title: Multi-wavelength study of white-light flares

Author: Lucia Mravcová

Institute: Astronomical Institute of Charles University

Supervisor: doc. Mgr. Michal Švanda, Ph.D., Astronomical Institute of Charles University

Advisor: Mgr. Jana Kašparová, Ph.D., Astronomical Institute of the Czech Academy of Sciences

Abstract: Solar flares are common and strong demonstrations of solar activity. They are observable throughout the whole electromagnetic spectrum. If they show a broadband emission in the visible continuum, then we speak of white-light flares. The origin of white-light flares is not fully understood. We detected 24 white-light flares in SDO/HMI data and analyzed them using SDO/AIA wavelength bands at 1 700 Å and 304 Å and GONG Hα observations. According to our work, the emission in the 1 700 Å band is similar to the white-light emission but usually starts sooner. The positions of intensity enhancements in the 1 700 Å band are similar to the positions of the white-light flares and are connected by ribbons visible in the 304 Å band and in the Hα line. Then we studied the decay time of white-light flares and found that for most of the white-light flare points the typical decay time ranges in 2 – 3 min.

Keywords: the Sun, solar activity, flares, white-light flares

Contents

Introduction

Solar flares are common solar phenomena where a huge amount of energy is released through the process of magnetic reconnection. The released energy takes many forms and we are able to observe solar flares across the whole electromagnetic spectrum [1]. A significant part of the energy that is released during solar flares is in the visible or the near ultraviolet continuum [2].

We speak of white-light flares if during a solar flare we observe a broadband emission in the visible continuum. The standard solar flare model has difficulties with explaining the emission in the visible continuum. There have been suggested some mechanisms that could explain where and how white-light flares occur. However, research results are inconclusive in terms of what exactly is responsible for emissions in the visible continuum [2].

By studying emissions in hard X-rays, it was suggested that electrons accelerated during the magnetic reconnection were somehow responsible for the white-light flare emission. As white-light flares should occur in the lower solar atmosphere they were for a long time considered to be phenomena that only concerns strong solar flares. It was believed that only during strong solar flares the energy of the electrons would be high enough to reach deep parts of the solar atmosphere [3]. Recently, white-light flares were detected even for weaker flares, for example in the study [4].

There have been many studies of white-light flares, such as the work [3] or [5]. They usually study one or a few solar flares. In this thesis, we want to study a larger number of solar flares so we need a program to detect white-light flares. We developed a program to detect them [6]. We applied this program to a large set of solar flare regions. We compare emissions in the visible continuum with other wavelengths and study the typical decay time of white-light flares. For only one flare, we also study the measurements (i.e. low-level data not usually available) that were used to create advanced data products which we use for our white-light flare detection.

1. The Sun

1.1 Fundamental information

The Sun is our nearest star, so it can be studied in great detail. It has been observed by not only multiple stations on the Earth but also by a great number of satellites from space. These observations allow us to study the Sun in a wide range of wavelengths with a resolution high enough to see the detailed structure of its atmosphere and surface. As it is the only star that this is possible for, it helps us to learn more about processes and the structure of other stars. Also, solar phenomena can have a direct impact on life on the Earth [7].

1.1.1 The solar interior

The interior of the Sun consists of four layers – the core, the radiative zone, the tachocline, the convection zone. The model of the Sun's interior is shown in Figure 1.1.

The core

The core reaches up to 25 % of the solar radius. The temperature at the center of the Sun reaches 15 MK and the density is about 150 g/cm^3. Both quantities decrease with an increasing radius and at the outer edge of the core the temperature is only 7.5 MK and the density drops to 20 g/cm^3 [8]. In the core, hydrogen is transformed into helium mostly by a process called the proton-proton chain. These nuclear reactions are the main source of solar energy [9].

The radiative zone

The radiative zone extends from the outer edge of the core up to 70 % of the solar radius. The temperature drops to 2 MK and the density drops to 0.2 g/cm^3 at the outer edge of the radiative zone [8]. The radiative zone is named after its main process of energy transport – the radiative diffusion. It means that photons are constantly being absorbed, emitted, and scattered by atoms, ions, and electrons. In this zone, the Sun rotates as a solid body [9].

The tachocline

It is a thin layer that lies between the radiative and the convection zone. The magnetic field of the Sun is generated in this layer [8].

The convection zone

The convection layer extends from the tachocline up to the surface of the Sun. The temperature at the inner edge of the convection zone is about 2 MK, which is cool enough for some ions to at least partially recombine. As a result, the material becomes more opaque and the radiative diffusion becomes less effective. Thus in the convection zone, the energy is transferred by convection to the surface, where

the temperature falls down to 5 700K [8]. In this zone, the rotation of the Sun is differential and the differential rotation is also observable on the surface [9].

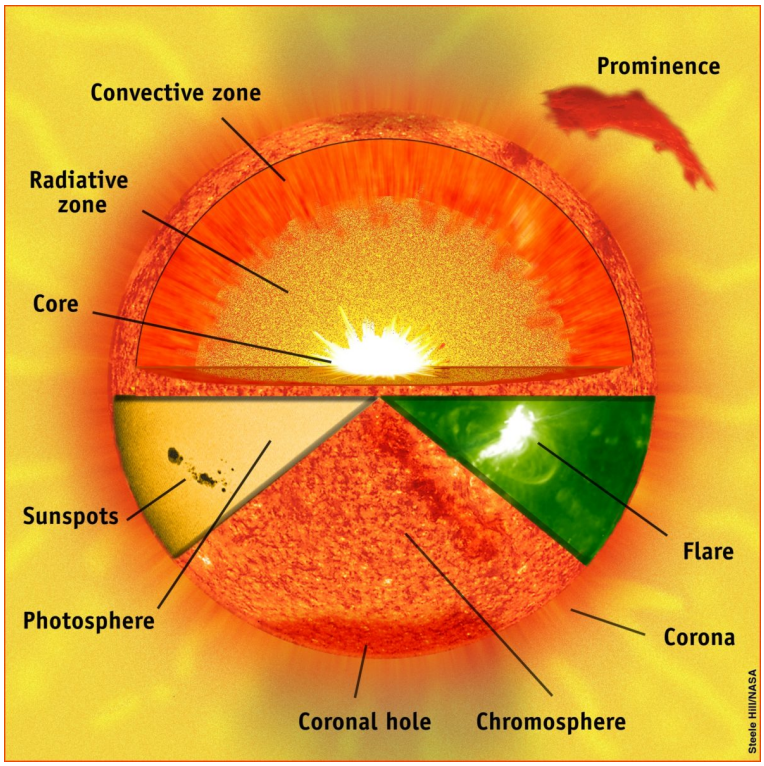

Figure 1.1: The interior and the atmosphere of the Sun along with some demonstrations of solar activity [10].

1.1.2 The solar atmosphere

The solar atmosphere consists of four layers – the photosphere, the chromosphere, the transition region, and the corona [9]. They are shown in Figure 1.1.

The photosphere

The photosphere is a 300 km thick layer in the lowest part of the solar atmosphere [9]. The photospheric temperature is about 5 800 K [11]. It is the source of most of the visible light that we observe. In the photosphere, the negative hydrogen ion H^- plays an important role. Its ionization energy is very low, so it can be ionized by visible or infrared photons. The process of the ionization of H^- to the neutral hydrogen is the main source of the opacity in the photosphere [9].

In the photosphere, we also observe a phenomenon called the limb darkening. The limb of the solar disk appears darker than the center. We observe the whole solar disk at approximately the same optical depth. Therefore, we see deeper parts of the solar photosphere in the center of the disk than at the limb. Deeper parts of the solar photosphere are hotter, hence they appear brighter [12].

The chromosphere

The chromosphere is a 2 000 km thick layer above the photosphere. The temperature ranges from the temperature minimum at 4 400 K up to 20 000 K. It can be observed in many spectral lines, for example in a hydrogen line Hα (656.3 nm) [9]. It is also visible in a line of calcium Ca II (393.4 nm). We can see this emission in other solar-type stars and it provides important information about their chromospheric activity [13].

The transition region

The transition region is a very thin layer. It separates the corona from the chromosphere. The temperature changes rapidly from 20 000 K to 1 MK. Hydrogen is ionized at these temperatures and we are not able to observe hydrogen lines. The light observed from the transition region is mainly emitted by ions C IV, O IV or Si IV. They emit in the ultraviolet (UV) region of the spectrum so it can be observed only from space [14].

The corona

The corona is a vast and extensive layer with temperatures around 1 MK [9]. At this temperature, hydrogen, helium, and minor elements like carbon, nitrogen or oxygen are completely ionized. Only the elements like iron or calcium are capable of retaining some of their electrons and produce coronal emission lines [15].

Contrary to the photosphere, the corona shines brightly in X-rays due to its high temperature. Thus observing the Sun in X-rays allows us to study the corona across the whole solar disk [15].

1.1.3 Solar activity

The Sun generates energy in many forms such as light, solar wind or energetic particles. The amount of generated energy is not constant and changes in time. These changes are called solar activity [16].

Demonstrations of solar activity:

- *sunspots* – dark spots on the surface of the Sun with the temperature about 3 700K. They usually last for days, large ones can last for weeks [17]. They are magnetic regions with strong magnetic fields of the order of 10^{-1} T [9]. Sunspots typically form in groups. Some parts of the group have a positive or north magnetic polarity and others have a negative or south magnetic polarity. The magnetic field is strongest in the darker parts of sunspots that are called the umbra. The lighter parts are called the penumbra and the magnetic field is weaker and almost horizontal there [17]. Motions of sunspots were crucial for discovering the differential rotation of the Sun [12]. Sunspots are shown in Figure 1.1 and in Figure 1.2.

- *faculae* – bright areas typically seen near the limb of the solar disk. They are magnetic areas but with weaker magnetic fields than sunspots. The total area of faculae on the solar disk is larger than the total area of sunspots,

so the influence on the solar brightness of faculae is dominant. As a result, the Sun is brighter during the maxima of solar activity even though there are more sunspots than during the minima [17].

- *granules* – small cellular features that cover the entire solar disk except for sunspots. Their typical size is about 1 000 km across. They are the tops of convection cells, where hot fluid rises up from the convection zone in the bright areas. The fluid spreads across the surface, cools down and sinks inwards along the dark lanes. The granulation of solar surface is constantly evolving, old granules disappear and new ones emerge. Individual granules last for about 20 minutes [17]. Solar granulation can be seen in Figure 1.2.

- *supergranules* – structures that look like a much larger version of granules measuring about 35 000 km across. They are best seen in Doppler-shift images and they cover the entire solar disk. Individual supergranules last for a day or two. The supergranulation pattern is constantly evolving [17].

- *prominences, filaments* – dense clouds of the material above the solar surface that are supported by magnetic loops. Prominences and filaments are the same features. Prominences are observed above the limb of the Sun, whilst filaments are prominences projected on the solar surface where they appear as dark, thread-like features in the Hα line [18]. Filaments or prominences are composed of relatively cool plasma with the temperature around 10^4 K floating in the corona occupied by plasma with the temperature at least 10^6 K[1]. A prominence can be seen in Figure 1.1.

- *plages* – bright patches surrounding sunspots where magnetic field is also concentrated. They are seen in the Hα line [18].

- *spicules* – narrow jets of plasma reaching up to 10 000 km above the photosphere. They are concentrated in areas with stronger magnetic fields [9]. They last for a few minutes and eject material to the corona at a speed of 20 – 30 km/s [18].

- *coronal loops* – structures following magnetic field lines that are anchored in the photosphere and connect magnetic regions on the solar surface [9]. They are found around sunspots. They can last up to days or weeks [19].

- *coronal holes* – darker, cooler and less dense parts of the corona. They are associated with "open" magnetic field lines that are connected to the interplanetary magnetic field [9]. They were discovered by X-ray telescopes that were the first to reveal the structure of the corona [19].

- *solar flares* – huge explosions that are accompanied by a sudden transformation of the magnetic field energy into the kinetic or the inner energy of the plasma. They can release the energy of the order of 10^{25} J [9]. Solar flares are discussed in detail in Section 1.2.

- *coronal mass ejections (CMEs)* – huge clouds of plasma with magnetic field that are ejected from the Sun [20]. They are usually associated with solar flares and can cause auroras in the planetary atmospheres [9].

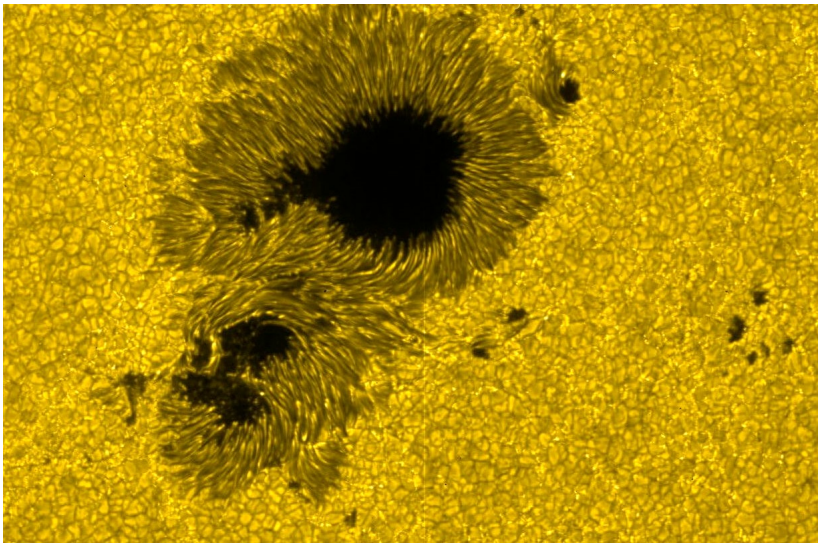

Figure 1.2: Visible light image of a sunspot and granulation [21].

1.2 Solar flares

Solar flares are explosive phenomena in the solar atmosphere with the total energy released in the range of 10^{22}–10^{25} J. The energy is released in various forms: radiative energy, kinetic bulk energy, thermal and non-thermal energy. The spatial size of flares varies, the height of a flaring loop can be less than 10^4 km or can reach up to 10^5 km in the largest events. Flares last for 10^3–10^4 s. Their duration, as well as the amount of energy released, depends on their size. Flares can be observed across the whole electromagnetic spectrum from radio, microwaves, visible light, UV, X-rays to gamma rays. Flares can also produce high-energy particles that can travel through the interplanetary space. If they reach the Earth, they can have a severe impact on its environment [1].

1.2.1 Flare Observations

The first solar flare was observed by R. C. Carrington and R. Hodgson in 1859 [22]. They observed a strong brightening in the white-light continuum in a complex sunspot group [22][23]. After the discovery of the spectroscope, it became possible to observe the Sun in the Hα line, which has its origin in the chromosphere. Many flares were observed in the Hα line. It led to the discovery that flares are frequent phenomena on the Sun [22]. In the Hα line, we often see two bright ribbons whose distance increases with time. Flares were then considered to be chromospheric phenomena [1].

In 1942 solar radio emissions were detected [22]. The solar irradiance in radio waves increased by several orders of magnitude during observed radio bursts. These radio emissions revealed the presence of non-thermal electrons in the corona. At the same time, S .E. Forbush noticed that detected enhancements in cosmic rays are correlated with major solar flares. These discoveries mean that flares are not confined to the thermal plasma but also include high-energy particles and extend to the corona [22].

In the late 1950s, it became possible to observe the Sun in hard X-rays (HXR), which correspond to the energy of at least 10 keV. It led to the first observation of an HXR emission during a flare in 1958. Observations in microwaves and HXRs suggested that the radiating energetic particles may contain a large amount of the initial energy release. HXRs are caused by the bremsstrahlung of electrons colliding with the surrounding plasma. The gyration of mildly relativistic electrons in magnetic fields is the source of some of the broadband radio emission with frequency from 1 GHz to beyond 100 GHz [22].

By observing thermal millimeter, extreme ultraviolet (EUV), and soft X-rays (SXR) (with energy lower than 10 keV) emissions, it was discovered that the flare energy heats the plasma of coronal loops from 1.5 MK up to 30 MK. Within minutes some active-region loops can outshine the rest of the corona in SXRs. High temperatures and acceleration of non-thermal particles imply that flares are coronal phenomena. Manifestations in the white light and in Hα seem like secondary phenomena. However, a large fraction of the released energy is emitted in the white light. Flares connect the corona with the chromosphere and they should be considered as an interactive system [22].

1.2.2 The standard flare model

The magnetic field provides the main energy source for solar activity including solar flares. It has its origin in the solar interior and it has to rise through the convection zone where it is surrounded by a high-pressure plasma doing convective motions. As a result, the magnetic field takes the form of a thin flux tube with some twist. After such a flux tube emerges onto the surface, the background gas pressure suddenly decreases which causes a rapid expansion of the magnetic field that forms a magnetic structure in the solar atmosphere. During this process, the magnetic field loses a part of the energy stored in the flux tube, some of the energy remains in the magnetic structure as the field-aligned electric current which does not produce the Lorentz force. This current is stored as free energy unless it is dissipated. It also introduces distortion into the magnetic structure, which can be observed as a sheared arcade or a twisted flux rope. The formation of a distorted magnetic structure is important for the understanding of the onset of a flare [1].

There are certain events preceding the onset of a flare. They are called precursors. One of the important precursors is a newly emerging bipolar sunspot region. It may interact with the preexisting magnetic field in the corona and trigger a flare. Another important precursor is the eruption of a filament. There has to be some destabilization in a magnetic structure containing the filament. The main forces responsible for such destabilization are the gradient force of magnetic pressure, magnetic tension force and gravitational force. Therefore, it is essential to know how these forces keep balance during the pre-eruptive phase of a filament, and what conditions undermine the balance [1].

The most promising mechanism for producing a flare is a process called the magnetic reconnection. During the magnetic reconnection, the magnetic field changes its configuration while a huge amount of energy is released. Several models of solar flares based on the magnetic reconnection were proposed. They assume a very similar configuration of the magnetic field and are called by a single

name – the CSHKP model [1]. A schematic picture of the CSHKP model and the magnetic reconnection is shown in Figure 1.3.

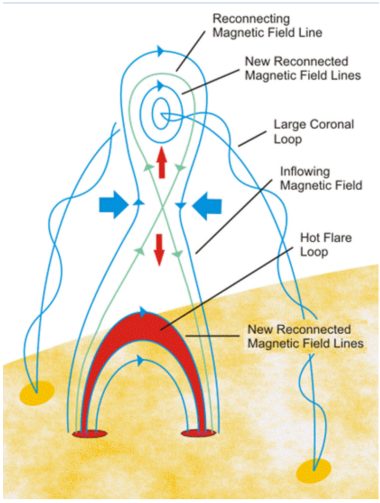

Figure 1.3: The CSHKP model of a solar flare [24].

The process of a solar flare can be divided into three phases – the preflare phase, the impulsive phase, and the gradual phase [23]. The development of a flare intensity in time at different wavelengths is shown in Figure 1.4.

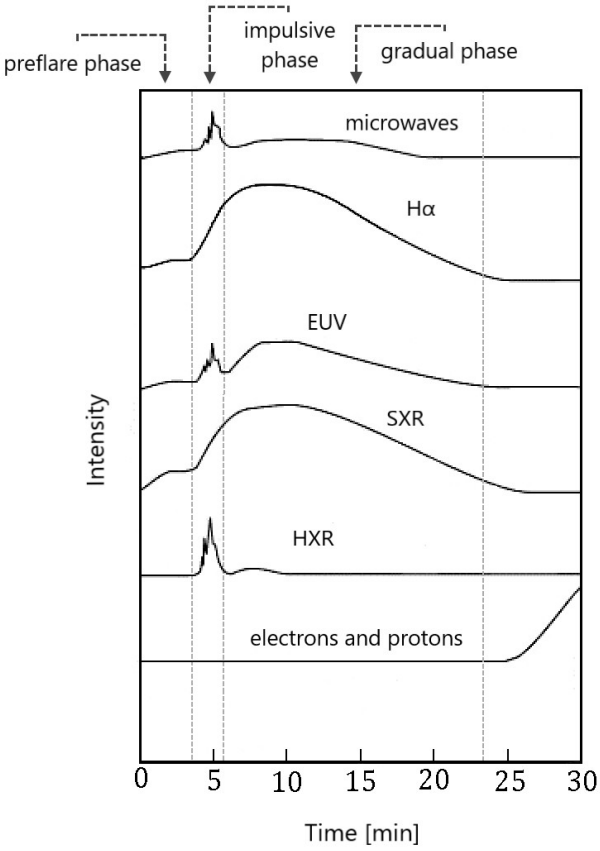

Figure 1.4: The evolution of flare intensity for different wavelengths. Inspired by [25].

The preflare phase

It is possible to observe an increase in emissions in some part of the active region. Several minutes before the onset of the HXR emission in the impulsive phase, we can see an increasing SXR emission in the preflare phase [23]. A slight increase in the SXR emission is also shown in Figure 1.4. It suggests that plasma heating occurs even before the onset of a flare [1]. The EUV emission can also increase in the preflare phase [22].

The impulsive phase

For the impulsive phase, the rapid increase of HXR and microwave emissions is characteristic. It can be seen in Figure 1.4. Also, high-energy particles are generated [1]. The impulsive phase usually lasts from tens of seconds up to several minutes [23].

During this phase, the most violent energy release occurs by the process of magnetic reconnection. The energy is then rapidly transported from the reconnection point by radiation, thermal conduction, high-energy particles, and plasma blobs. Part of the energy is transported downward along the magnetic field lines via thermal conduction and high-energy particles. It causes the heating of the chromospheric plasma. The gas pressure of the heated chromospheric plasma increases and the plasma evaporates into the corona and fills a magnetic loop with hot plasma. Such a loop is observed in the SXR, so it is called an SXR loop. High-energy electrons generated by the magnetic reconnection move downwards along the SXR loop and form a source of HXR emissions at the chromospheric footpoints of the SXR loop. This HXR source is called an HXR footpoint source. While moving downwards along the SXR loop, high-energy electrons also produce microwave emissions by gyro-synchrotron radiation. Another HXR source is created above the top of the SXR loop and it may be formed by a downward high-speed flow produced by the magnetic reconnection which collides with the top of the SXR loop. It is called an HXR loop-top source. At the footpoints of the SXR loop, bright kernels are observed in Hα. It is another indication of the chromospheric heating by thermal conduction and high-energy electrons. The Hα kernels are observed as two ribbons which are referred to as the Hα ribbons [1].

Another part of the released energy is transported upwards in the form of an ejecting plasma blob called a plasmoid [1].

The gradual phase

The duration of the gradual phase depends on the flare size. The gradual phase lasts for tens of minutes up to several hours [23]. Contrary to the HXR and microwave emission that are significant only in the impulsive phase, the SXR and Hα emission continue to increase and are dominant in the gradual phase [1], as it is shown in Figure 1.4.

The main contribution to the Hα emission comes from loops filled with cool plasma with the temperature about 10^4 K. They are called Hα loops. Hα loops appear when the SXR loops cooled enough via radiation and can be observed in Hα. The magnetic reconnection, however, proceeds in the corona and new SXR

loops pile up on the preexisting SXR loop. Therefore, the apparent height of the observed SXR loop increases in time. It is also responsible for the increase of the distance between the Hα ribbons. We are capable to observe flare loops on the solar disk in Hα only if they are dense enough. It happens only for very powerful flares, so it is considered to be a rare phenomenon [1].

In Hα loops, the pressure gradient cannot compensate the gravitational force, so the plasma moves downwards to the solar surface along the loops. In the upper parts, the motion of the plasma can be considered as a free fall in the solar gravitational field. However, near the surface, the plasma speed does not increase because the plasma is decelerated in the denser parts of the loops [23].

1.2.3 The classification of solar flares

Solar flares can be classified into five classes according to their X-ray peak flux in the wavelength range 1 – 8 Å. It is measured by the satellite GOES[1] (Geostationary Operational Environmental Satellite). Fluxes associated with each class are stated in Table 1.1. Each class is divided in a scale from 1 to 9 with an exception for the class X that is not limited to X9 but continues further [26]. In Figure 1.5, we show fluxes of some solar flares and their GOES classes. The red curve represents the solar flare flux in the range of 1 – 8 Å.

Class	Flux [W/m^2]
A	$< 10^{-7}$
B	$\langle 10^{-7}, 10^{-6})$
C	$\langle 10^{-6}, 10^{-5})$
M	$\langle 10^{-5}, 10^{-4})$
X	$\geq 10^{-4}$

Table 1.1: X-ray fluxes of flare classes [26].

1.3 White-light flares

White-light flares (WLFs) are solar flares with a broadband emission in the visible continuum. Enhancements in the optical continuum are typically a few tens of percent compared to the photospheric background. However, the WLF observed by Carrington probably had its intensity twice as high as that of the quiet photosphere [3].

Despite the fact the first solar flare ever observed was a WLF, the origin of WLFs is not fully understood. Nevertheless, the understanding of the origin of WLFs and the related near UV continuum is essential. A significant part of the energy released during a solar flare is via the white light (WL) and near UV continuum [2].

It is relatively difficult to observe WLFs, as the enhancement in the WL is quite small and localized. It led to the conclusion that WLFs are rare phenomena

[1] `https://www.nasa.gov/content/goes-overview/index.html`

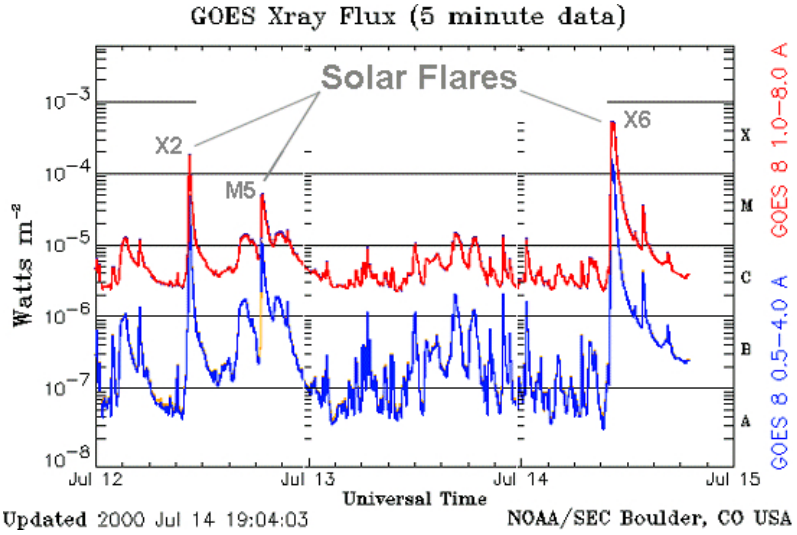

Figure 1.5: Solar flare classification by their X-ray flux in the range of 1 – 8 Å, which is plotted in red [27].

and occur only during strong solar flares [3]. However, WLF enhancements were observed even for weak solar flares. In [28] they observed a WL emission for a class C2.0 solar flare and in [4] it was observed for a class C1.6 solar flare. It was then suggested that all solar flares are accompanied by some emission in the WL continuum [29].

WLFs have enhancements in the continuum at wavelengths greater than 3 600 Å. So it was suggested that WLFs enhancements come from the Paschen continuum with wavelengths greater than 3 647 Å with contribution from the Balmer continuum with wavelengths in the interval 912 – 3 646 Å [3]. The Balmer continuum is caused by hydrogen recombination to the first excited state, the Paschen continuum is caused by hydrogen recombination to the second excited state. Some WLFs exhibit the Balmer jump that occurs at the wavelength of 3 646 Å. A Balmer jump is a jump in the observed intensity and it occurs at the ionization wavelength that corresponds to the first excited state of hydrogen. Type I WLFs exhibit a Balmer jump, Type II do not.

Solar flares studied in [30] and [31] suggest that there is a correlation between WL enhancements and HXR enhancements during solar flares. Both of these studies imply that HXR emission and WL emission are excited by the same source which is non-thermal electrons. In the study [32], they investigated three WLFs. Two of them were Type I, the other one was Type II. According to this study, the peaks in HXR and microwave radiations correlate well with the peaks in WL radiation for Type I. However, for Type II there is no such correlation. The maximum in the WL precedes or lags behind the peaks in HXR and microwave radiations. They suggest that these two types of WLFs have different energy sources and different energy transport mechanisms.

The height of WLF emissions has not been determined yet. It could involve the upper chromosphere, the temperature minimum region, and the photosphere [3]. The theory predicts that at least some part of the WL emission originates in the upper photosphere [33]. Electrons accelerated during the magnetic reconnection need to have the energy of the order of 100 keV to reach the lower chromosphere

and of a few MeV to reach the photosphere [3]. For the strongest solar flares, electrons reach the energy of several hundreds of keV [34]. So several mechanisms for the generation of WLF emissions were suggested:

1. **chromospheric free-bound emission**: During a flare, hydrogen over-ionization in the chromosphere occurs, which can be caused by accelerated electrons. Free-bound emission is a result of hydrogen recombination [3]. It produces enhancements in Balmer and Paschen continuum [34]. A recent study of the X9.3 flare on 2017 September 06 showed that this mechanism may play an important role in generating WLFs [35].

2. **enhanced photospheric H^- continuum emission**: Accelerated electrons cannot directly heat the photosphere and they are stopped at higher heights where they heat the medium. The photosphere is then heated by radiation from the chromosphere, for example by Balmer radiation. It can penetrate to the upper photosphere and provide sufficient heating for producing a WLF. This process is called radiative backwarming [2]. We would observe an enhanced blackbody spectrum [3].

3. **proton energy**: Protons with the energy of a few MeV could reach the sufficient depth and provide the needed heating [2].

4. Models considering accelerated electron could be wrong and both HXR and WLF emissions have their origin elsewhere [2].

The mainly considered mechanisms are the first two. It is also possible that both of them can be responsible for WLF emissions. The strength of each component would then vary from flare to flare [3].

2. Data

2.1 Flare selection

Solar flares suitable for WLF detection were selected by using GOES archive. They had to meet the following criteria:

- They had to occur after 2010 due to the data availability.
- They were of class M5.0 or stronger. We assumed that WLF detection would be easier for stronger flares.
- They occurred near the center of the solar disk. Such a position criterion limits the impact of foreshortening, which means that observed objects are shortened in a certain direction. On the solar disk, object sizes are shortened in the radial direction due to the fact that we only observe a 2D projection of the Sun. So no chosen flare occurred further from the center than 50 ° in any direction.

All selected flares were checked in Solar Monitor[1]. In some cases there was a difference no greater than 0.1×10^{-5} W/m^2 between the GOES intensity and the intensity in Solar Monitor. We used the GOES intensity for them.

These criteria were met by 53 solar flares that occurred between 2011 February 13 and 2015 August 24. We detected 23 WLFs and they were used for further analysis. We added another strong WLF of class X9.3 that occurred on 2017 September 06. In total, we analyzed 24 WLFs.

2.2 Data for WLF detection

Solar Dynamics Observatory (SDO) is NASA's mission that monitors the Sun and its activity [36]. It observes the solar atmosphere, the Sun's magnetic field, irradiance and the hot plasma in the corona. There are three instruments on board. For detecting WLFs, we use data from the instrument Helioseismic and Magnetic Imager (HMI) [37][38]. HMI studies oscillations and the magnetic field at the solar surface. It observes the full solar disk in the Fe I line (6173 Å) at six different narrow filters and in different polarization states [39]. From these measurements, HMI provides four main types of data:

- **dopplergrams** – maps of solar surface line-of-sight velocity
- **continuum filtergrams** – broad-wavelength images of the solar photosphere
- **vector magnetograms** – maps of the photospheric magnetic field
- **line-of-sight magnetograms** – maps of the photospheric magnetic field that is projected in the direction to an observer.

[1] `https://solarmonitor.org/`

Continuum filtergrams were used for detecting WLFs. They were downloaded from Joint Science Operations Center[2] (JSOC) which provides an image of 768×768 pixels every 45 s of the requested area of the Sun. One pixel corresponds to 0.5" on the solar disk. JSOC also tries to compensate the effects of the solar rotation. Images are tracked with the speed of Carrington rotation, which is the mean synodic rotation. These images are linked together to create a data cube that starts one hour before the flare starts and ends after three hours, so it contains 240 frames.

2.3 Data for analysis

2.3.1 Observations of WLFs in the white-light and at different wavelengths

For analyzing WLFs in the Hα line, we use observations from Global Oscillation Network Group (GONG) [40]. The main purpose of this network is to study the solar internal structure and dynamics using helioseismology. Since 2010 GONG has also been obtaining Hα images of the solar disk. They are collected once per minute at six stations on the Earth [41]. In Hα we can observe Hα ribbons and Hα loops as it is mentioned in Section 1.2.2.

For analyzing WLFs in UV and EUV, we use data from Atmospheric Imaging Assembly (AIA) that is another SDO instrument [42][43]. AIA provides observations of the solar corona that obtain images in multiple EUV and UV passbands. We use a channel in UV at 1 700 Å and a channel in EUV at 304 Å. AIA produces an image at 1 700 Å every 24 s and at 304 Å every 12 s.

The AIA 1 700 Å band

The AIA 1 700 Å band is designed to carry out broadband observations of the UV continuum. It often shows a web-like pattern of bright areas that highlight places where magnetic field lines are concentrated. However, near sunspots, small areas with a lot of field lines appear black. In this channel, we should observe the temperature minimum region and the photosphere [44]. However, it is possible that we also observe different parts of the solar atmosphere in this band [45].

There are studies that imply that emissions in the AIA 1 700 Å band may come from the chromosphere. In the work [45], they studied emissions from a flare and from a plage in the AIA 1 700 Å and 1 600 Å filters. They estimated that 87 % of the plage emission at 1 700 Å comes from the photospheric continuum. Nonetheless, during a flare, the main contributor is the C I 1 656 Å line (38 %), followed by the He II 1 640 Å line (17 %) and other chromospheric lines. The contribution from the continuum is minimal.

So in the 1 700 Å band, we observe the part of the solar atmosphere that is either above or at approximately the same height as the WL emission.

[2] http://jsoc.stanford.edu/

The AIA 304 Å band

The light observed in the AIA 304 Å band comes from the He II 304 Å line [46]. This channel is good for observing filaments and prominences where cooler dense plasma is located. Bright areas show places with high-density plasma. The AIA 304 Å shows the upper chromosphere and the lower transition region [44].

The He II 304 Å line is the most intense line in the solar spectrum below 1 000 Å. It has an important role in the energy balance through radiative cooling during solar flares [47]. The AIA 304 Å band may, however, contain emissions from coronal sources. The main chromospheric component in the AIA 304 Å band comes from flare ribbons that are at footpoints of coronal magnetic loops. Despite the coronal contamination, the He II 304 Å emission from flare ribbons is distinctive and we can clearly observe the progression of flare ribbons [46].

Constructing data cubes

Images in 304 Å and 1 700 Å were also obtained from JSOC, so they are co-aligned with images from HMI and have the same scale and size. However, there were some problems with the alignment for Hα images. We tried to create them with the same scale as HMI images and align them properly. Unfortunately, it was not entirely possible and there are some intensity oscillations and small differences in image rotations from frame to frame. The main reason for these data defects is that Hα images are obtained from different stations which produce slightly different images. Also, the full-disk Hα images were normalized to the median of the quiet Sun. After that, we cut out the images of the demanded region from the full-disk observations.

For all channels, we divided every image by its exposure time. For comparing lightcurves, images were only joined together creating a data cube. We created a special timeline for each data cube because, sometimes, there are some frames missing and we need to know what time corresponds to each frame. For comparing the position of emissions, data cubes for the Hα line, the 304 Å band and the 1 700 Å band were created by interpolation so they have the same time cadence as filtergrams from HMI.

2.3.2 HMI filters

As it was mentioned in Section 2.2, HMI scans the Fe I line at six narrow bands. These measurements are then used to reconstruct continuum filtergrams that we use for WLF detection. In the reconstruction process, the line is assumed to have the Gaussian profile and the continuum intensity I_c is obtained by

$$I_c \approx \frac{1}{6}\sum_{j=0}^{5}\left[I_j + I_d \exp\left(-\frac{(\lambda_j - \lambda_0)^2}{\sigma^2}\right)\right], \tag{2.1}$$

where I_j is the intensity of filters, λ_j is the wavelength of filters, I_d is the line depth, λ_0 is the Doppler-shifted wavelength of the center of the line and σ is a measure of the line width [39]. The quantity σ is associated with FWHM (full width at half maximum) by the following relation

$$\mathrm{FWHM} = 2\sigma\sqrt{\log 2}. \tag{2.2}$$

It works quite well for the quiet Sun, but during flares, the line can be distorted. For example, there can be some asymmetries or emissions in the center of the line while the wings stay the same. In magnetized regions, the reconstructed continuum can be strongly biased because all the filters are located in the magnetically broadened line core. The line sampling is inadequate in these cases and HMI continuum filtergrams can only be used as an indicator for WLF observations. Enhancements in HMI continuum can be caused by both the real continuum enhancement and by the distortions in the measured line [48].

Measurements in filters are not easily available, so we obtained them for only one flare, specifically the X9.3 flare on 2017 September 06. The filters are labeled by their wavelengths with respect to the center line wavelength, so the filters are -17.2 pm, -10.3 pm, -3.4 pm, $+3.4$ pm, $+10.3$ pm, and $+17.2$ pm. Measurements in each filter are taken in multiple polarization states. For our purposes, we only used unpolarized light. We created data cubes for every filter with the same resolution and time cadence as the HMI filtergrams.

3. Methods

3.1 Detecting WLFs

WLFs appear as brightenings in the solar photosphere often near sunspots. Their area is usually very small compared to our image size and they typically last longer than 45 s. In data cubes, we see WLFs as brighter spots that appear in multiple frames and move from frame to frame. So a program was developed for detecting WLFs. The program marks confined brightened areas that also appear in other frames as points where a WLF occurred. To show how WLFs look in our data, we created Figure 3.1. In Figure 3.1a, there is an image of the continuum filtergram for the X5.4 flare on 2012 March 07. A WLF occurred in Figure 3.1a but it is hardly visible there. In order to show where WLF ribbons are located, there is a difference image shown in Figure 3.1b, where we subtracted the previous image from the following. However, the program detects WLFs in continuum filtergrams, such as in Figure 3.1a.

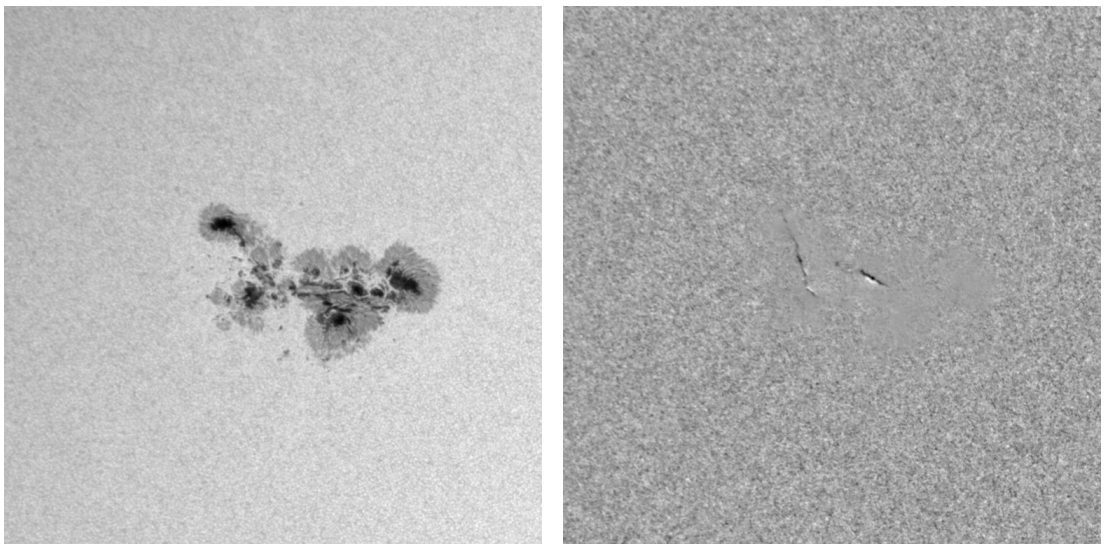

(a) HMI continuum filtergram (b) Difference image

Figure 3.1: HMI continuum filtergram and a difference image for the X5.4 flare on 2012 March 07.

The input of the program is a data cube in FITS[1] format where the first two coordinates are spatial and the third is time. The size in both of the spatial coordinates must be the same.

The program reads the input and stores it in a 3D array. For each spatial point, it eliminates long-term trend in intensity. It fits the time-dependent intensity at every spatial point with five-degree polynomial that is then subtracted from the original values. After that, the program counts the mean value and the standard deviation for each spatial point. The program then remembers only those points where the intensity is greater than the sum of the expected value and the standard

[1] `https://fits.gsfc.nasa.gov/fits_documentation.html`

deviation multiplied by the parameter σ_M. This part of the program is executed in parallel.

Now we look for groups of points where a WLF might have occurred. It is done for each cut in time separately, so the program searches only in 2D arrays. We use the breadth-first search algorithm [49] (BFS) that for each point with intensity large enough looks at its eight neighbors to see if their intensity is above the desired level. If a found group of points with higher intensity is large enough (57 points were chosen by looking at brightenings in data cubes by the naked eye and by considering the expected size of WLF areas), the program stores it and begins searching for another group until it processes all points. There is also an upper boundary (3 000 points) for the number of points in one group. It was introduced there because there were missing frames in some data cubes due to the less-than-optimal duty cycle of the instrument. Otherwise, the program detected a sudden large-scale elevation of intensity in the frames after the missing ones. It was too large to be a WLF so it had to be eliminated.

For each found group, the program finds its center by counting the mean of both of the spatial coordinates. Again using the BFS algorithm, the program finds if near the center of one group is the center of another group from the following time moment. If the time interval between the first and last center in the found set of groups is long enough (the limit is set to four frames which correspond to three minutes), the set is stored. For the same reason as in the first BFS, there is an upper limit (1 000 points) for the number of points in a set. After processing all of the groups, the program writes all the points from all the remembered sets into the output file. These points are considered as points where a WLF occurred.

The output file is a text file with three columns containing the coordinates of the detected WLF. The first two are spatial a the third is time.

The results of the code are sensitive to the value of σ_M, which is a free parameter of the program. Lower values increase the number of detected points but they will contain a lot of false positives (points where intensity exceeded the threshold randomly). Larger values decrease the code susceptibility to random oscillations. However, it also decreases the number of detected WLF points. The program would not detect points where the brightening is not that marginal. To find the optimal value of σ_M, we studied two variables and their dependence on the value σ_M.

1. **The total number of detected WLF points**: The areas of WLFs should be much smaller than the total area of the field-of-view. If the selected value of σ_M was larger than the optimal, the total number of points WLF points should decrease slowly because the points with weaker brightenings would gradually fall below the detection threshold. For smaller values of σ_M, there would be a steep increase in the total number of detected WLF points. We would then also detect random fluctuations.

2. **The spatial dispersion of WLF points**: WLFs points should occur in confined areas, whereas random fluctuation can appear anywhere in the image. We counted the standard deviation of positions of WLF points separately in both coordinates. For larger values of the parameter σ_M, we would expect the dispersion to be approximately constant. For smaller

values, we would expect a sudden increase as we start detecting random fluctuations.

After testing a large range of values, the optimal value of σ_M was set to 1.88. This method for WLF detection was published in [6].

The program was written in C# and requires .NET Framework 3.5. For reading FITS files, we use CSharpFITS[2] library. We have it only as a compiled library for the Windows platform so the program runs only on the Windows platform. For the polynomial interpolation, we use a library that is distributed by source codes and can be freely downloaded.[3]

3.2 Comparison of lightcurves

For comparing the WLF emission with emissions at other wavelengths, we constructed lightcurves for each wavelength. For the WLF lightcurve, we consider intensity only from those points where the WLF is detected. In each time moment, we sum the intensity of all the WLF points to get the total time-dependent intensity of the WLF.

In other wavelength channels, brightenings are much stronger than the background. In order to show how these brightenings look, in Figures 3.2, 3.3 and 3.4, there are images of the Sun before and during the X9.3 flare on 2017 September 06 at 1 700 Å, 304 Å and in the Hα line. In Figure 3.2b, we can see that there is a problem with pixel saturation for the 1 700 Å band. The intensity in some pixels during flares is too high, it overflows and appears in neighboring pixels. However, it is not a problem for lightcurves as we are only interested in the total intensity and not intensities of particular points.

To create lightcurves in other wavelength channels, we sum the intensity of the whole time frame to get the time evolution of the total frame intensity. In order to eliminate the background intensity for these wavelengths, we counted the mean of the first few values of the total intensity. Then this mean was subtracted from the total intensity. The flare started later in the data so it does not influence the background elimination.

For the WL, 1 700 Å and 304 Å, the intensity is normalized to its maximum. The situation is different for Hα. As these data come from six stations, the images significantly differ. Images from different stations are often shifted and their intensity is not sufficiently calibrated so there are jumps in intensity due to this fact. There are also large peaks in intensity that are clearly not caused by some activity on the solar disk. So the Hα intensity is normalized to its local maximum near the maximum of the WL intensity. We use normalization to maxima because it would be very difficult to derive the real physical units. Besides, it would be hard to compare the lightcurves as the intensities in real physical units may not even have the same order of magnitude.

[2] `https://www.nuget.org/packages/CSharpFITS/` Last access: 2019 April 09

[3] `http://www.vilipetek.com/2014/12/13/polynomial-fitting-in-c/` Last access: 2019 April 09

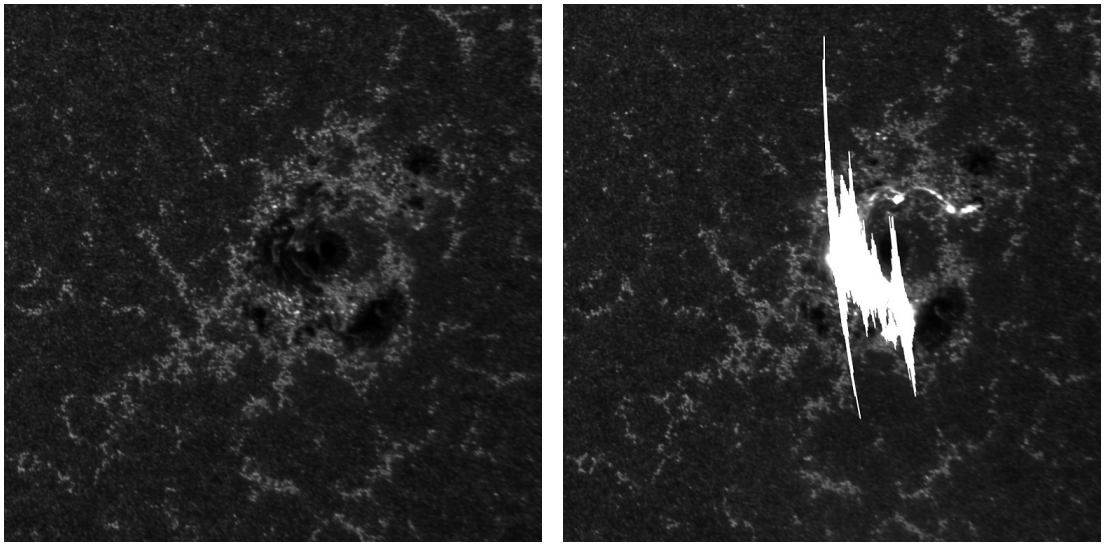

(a) Before the solar flare (b) During the solar flare

Figure 3.2: Images at 1 700 Å before and during the X9.3 flare on 2017 September 06.

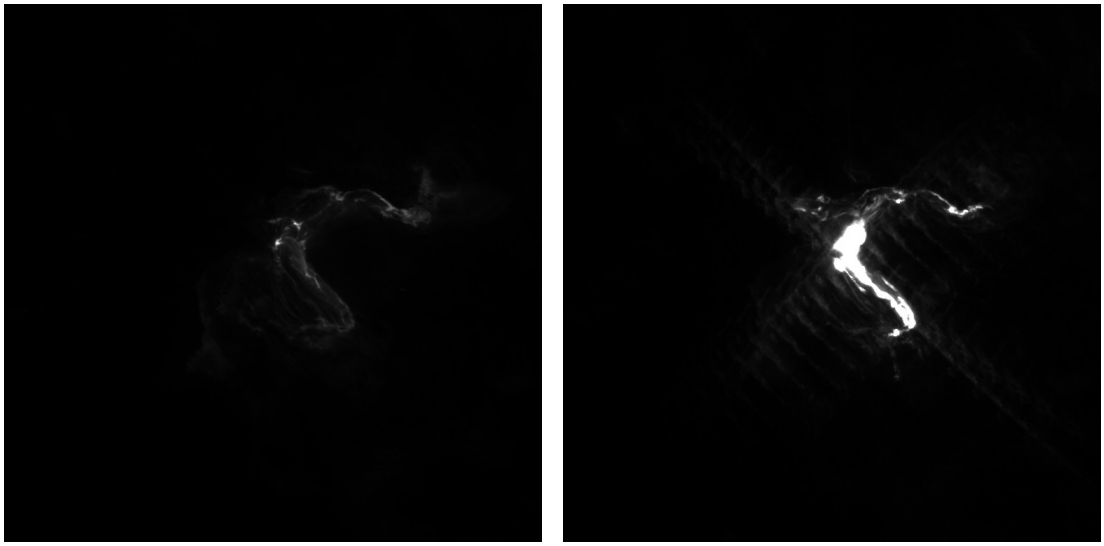

(a) Before the solar flare (b) During the solar flare

Figure 3.3: Images at 304 Å before and during the X9.3 flare on 2017 September 06.

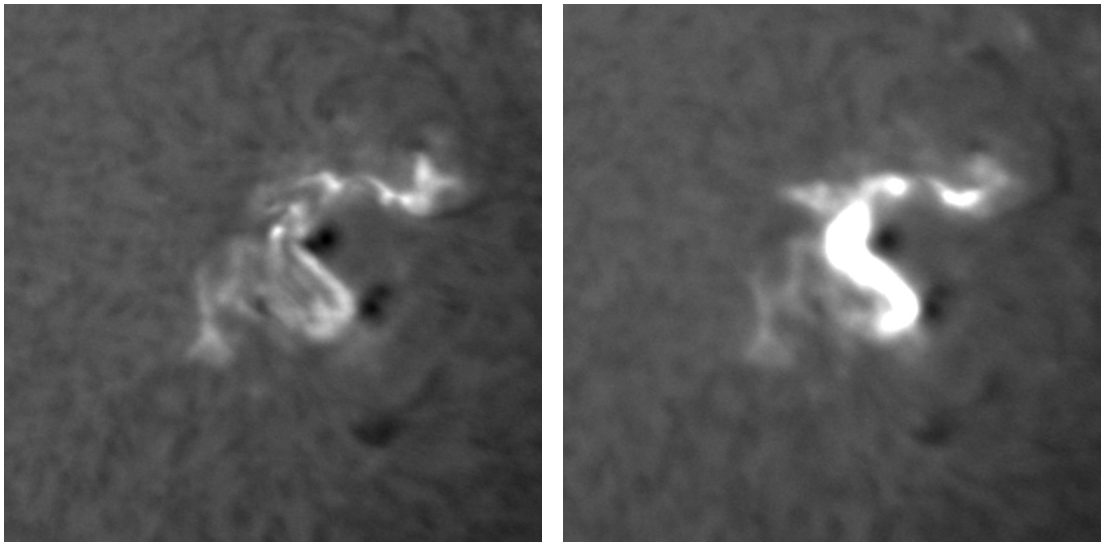

(a) Before the solar flare (b) During the solar flare

Figure 3.4: Images in the Hα line before and during the X9.3 flare on 2017 September 06.

3.3 Comparison of enhancements positions

In order to compare the positions of enhancements, we create videos where we can see all channels at the same time. In these videos, the data cubes have the same cadence. Videos are created from images where detected WLF points are plotted. In every image, points with red color are those where a WLF was detected at any time during the whole data cube. Points plotted with blue color are those where a WLF was detected at the time that corresponds to the image. As an example, we show images for X5.4 flare on 2012 March 07 in Figure 3.5.

3.4 Lightcurves of WLF points

We want to find the typical decay time for WLFs. For every WLF, we construct lightcurves for every point of a WLF. Even though intensity brightenings can occur multiple times in one point, in this case, it counts only as one WLF point and has only one corresponding lightcurve. Then we select only those points whose lightcurves have a certain shape that is expected from WLFs. There should be a sudden increase in intensity and then a slow decay. We exclude points that do not have their maximum close to the maximum of the overall lightcurve, which is counted when comparing lightcurves of different channels. Further, we exclude points where the brightening at its peak is less than 10 % compared to the intensity before the flare. All lightcurves are normalized to the value approximately 15 minutes before the maximum of each of the lightcurves.

Firstly, we find the decay time by studying the mean lightcurve. All lightcurves of WLF points are shifted to one another so their maxima occur at the same time. Then we count the mean value at each time. Thus we get the mean lightcurve. The errors were calculated as standard deviations but separately for values smaller than the mean and for values larger than the mean. The decay

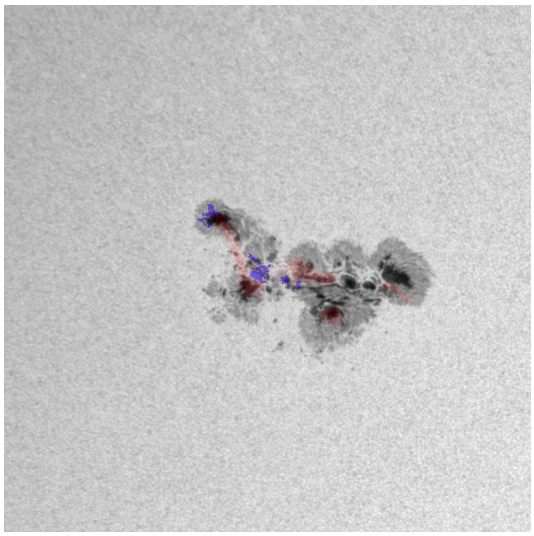

(a) The white light

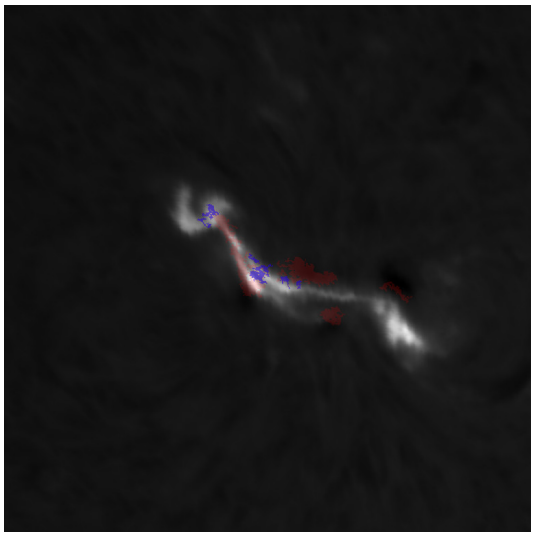

(b) The Hα line

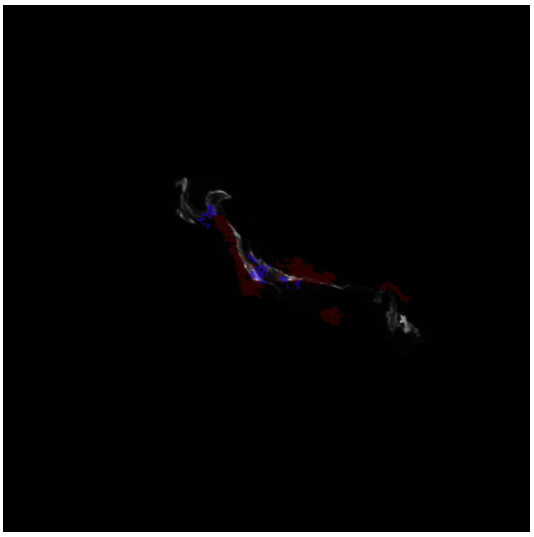

(c) 304 Å

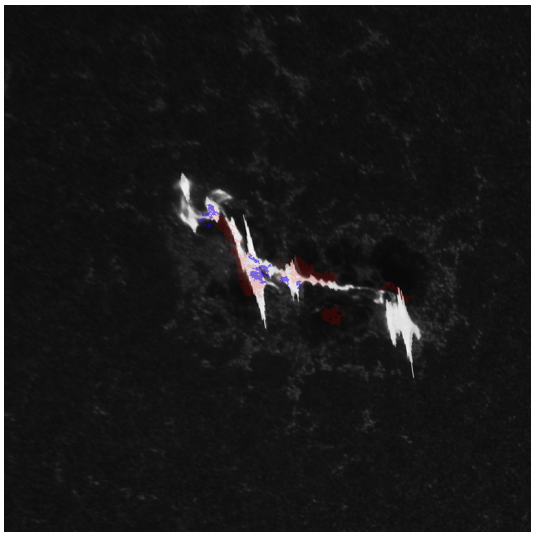

(d) 1 700 Å

Figure 3.5: Images of the Sun in different wavelength channels for the X5.4 flare on 2012 March 07 at 00:09:00 UT. Red points are points where a WLF was detected at any time during the whole data cube. Blue points represent points where a WLF was detected at the time that corresponds to this image.

time is estimated by fitting a part of the lightcurve (starting at the maximum and ending 20 points after). The fitted function is an exponential function of the form

$$f(t) = A \exp(-Bt) + C \tag{3.1}$$

where t is time and A, B and C are the fitted constants. The decay time τ_{decay} is then taken as the inverse value of the constant B. The decay time error σ_τ is estimated from

$$\sigma_\tau = \frac{\sigma_B}{B^2} \tag{3.2}$$

where σ_B is the error of the fitted value B.

In order to estimate the decay time, we use also another approach. Instead of fitting the mean lightcurve we fit lightcurves of individual WLF points. Thus we get a set of decay times for each WLF. From this set, we create a histogram of fitted decay times.

3.5 Emission detection in HMI filters and its analysis

For the detection of intensity in filter data cubes, we use the same code as for detecting WLFs in continuum filtergrams. However, it is necessary to find the optimal value σ_M for each filter separately. The methods used for finding σ_M for filters are the same as for continuum filtergrams. In Figure 4.3, there are filter images where we detected intensity enhancements. Blue points represent enhancements in filters at the time corresponding to images and red points represent points of the detected WLF at this time.

It seems that the position of enhancements in filters are more or less the same as in the reconstructed continuum. So we create masks for filters and the continuum. It means that points where an enhancement appears are labeled as one and all the other points are labeled zero. Then we subtract the masks of filters from the continuum mask and take an absolute value of the difference. Now the zero points are those where either enhancements appear in the filter and in the continuum or in neither of them. Points with value one are those where an enhancement appears only in the filter or the in the continuum. For every filter, we sum over all the points in each time to see how this quantity evolves in time. The bigger the value is at a given time, the larger the difference between the continuum and the filter is. This quantity is at first normalized to the number of points detected in the continuum in each time. Therefore, we only consider those time moments when there is an enhancement in the continuum data cube. Then the quantity is normalized to its maximum. This normalization is done in order to compare the filters to one another.

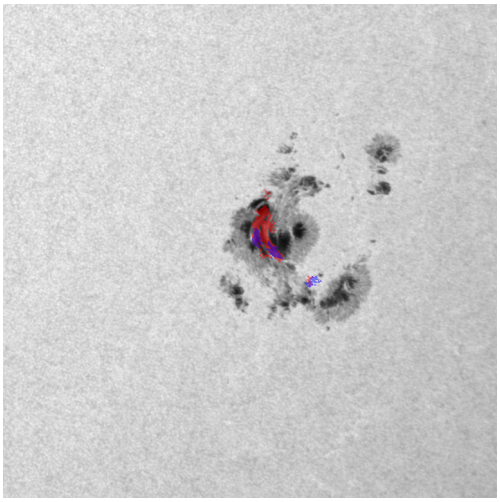

(a) −17.2 pm

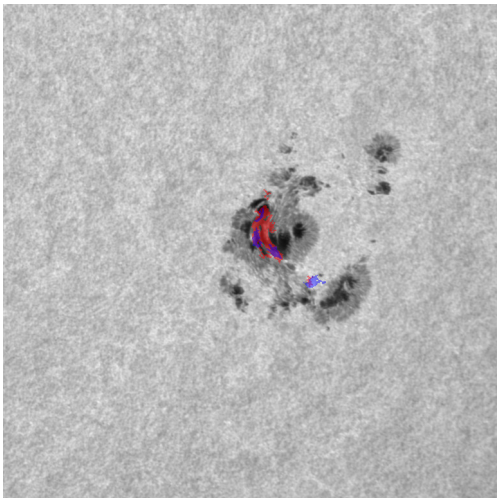

(b) −10.3 pm

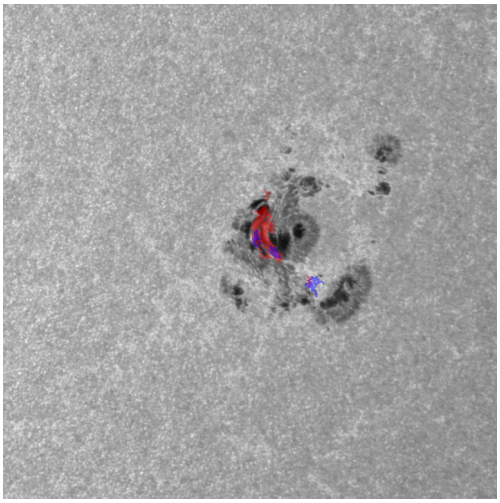

(c) −3.4 pm

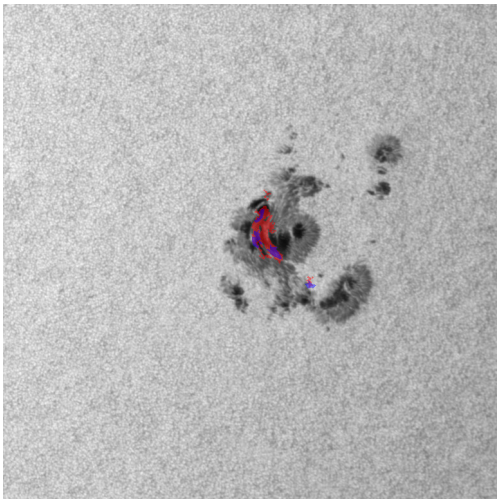

(d) +3.4 pm

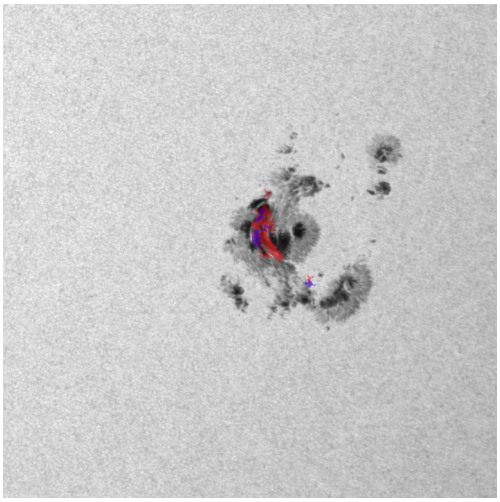

(e) +10.3 pm

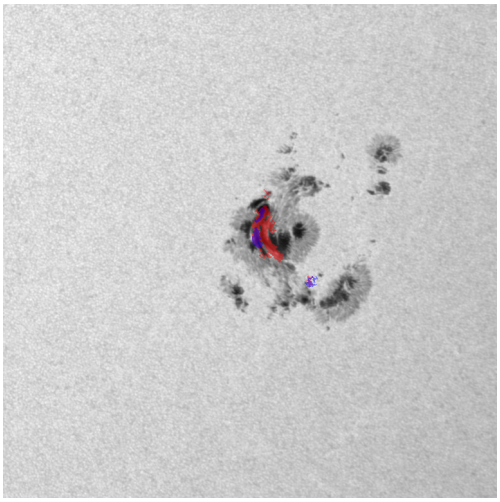

(f) +17.2 pm

Figure 3.6: Images of the Sun in different HMI filters for the X9.3 flare on 2017 September 06 at 12:00:00 UT. Red points are points where brightenings in the HMI filtergram was detected at the time that correspond to this image. Analogously, blue points are detected enhancements in filters.

4. Results

The list of detected WLFs is shown in Table 4.1. Dates and times correspond to the time of the maximum of a solar flare according to GOES archive, as well as solar-flare classes. Then there are numbers of points detected by the program for WLF detection and numbers of detected unique points. The number of unique points is determined from the total number of detected points. In the total number of detected points, spatial points can be counted multiple times according to the number of frames where intensity enhancements were detected. The number of detected unique points counts every point once, regardless of how many times we detect a brightening there.

Date	Time [UT]	Class	Number of detected points	Number of detected unique points
2017 September 06	12:02	X9.3	33007	5432
2012 March 07	00:24	X5.4	23214	5737
2013 November 05	22:12	X3.3	1603	633
2014 October 24	21:41	X3.1	433	176
2011 February 15	01:56	X2.2	4542	1254
2011 September 06	22:20	X2.1	3995	1196
2014 October 26	10:56	X2.0	5191	1023
2014 December 20	00:28	X1.8	3882	1352
2011 September 07	22:38	X1.8	5209	1486
2014 October 22	14:28	X1.6	622	314
2012 March 07	01:14	X1.3	4713	4394
2011 July 30	02:09	M9.3	2731	985
2011 August 04	03:57	M9.3	1104	483
2014 October 22	01:59	M8.7	488	163
2015 June 25	08:16	M7.9	3265	1273
2014 January 07	10:13	M7.2	1393	668
2014 October 27	00:34	M7.1	652	170
2012 March 09	03:53	M6.3	962	243
2013 November 01	19:53	M6.3	1217	345
2012 July 05	11:44	M6.2	3370	1304
2015 August 24	07:33	M5.6	1645	575
2011 September 06	01:50	M5.3	734	248
2014 February 04	04:00	M5.2	2429	696
2014 September 28	02:58	M5.1	420	124

Table 4.1: Date and time of the maximum of a solar flare, class of a solar flare, a number of detected WLF points and a number of detected unique WLF points for detected WLFs.

4.1 Comparison of lightcurves at different wavelengths

We constructed lightcurves for every WLF in order to compare emissions at different wavelengths. All of them are shown in Attachment A.1. An example is plotted in Figure 4.1, where it is possible to see lightcurves for the X5.4 solar flare on 2012 March 07 with the solar flare maximum at 00:24 UT. It is then followed by the X1.3 flare on 2012 March 07 with the solar flare maximum at 01:14 UT. In Figure 4.1a, there are lightcurves for the whole duration, so there is the intensity evolution over three hours. In Figure 4.1b, the lightcurves are zoomed in in the interval ± 15 min around the WL maximum. The quantity on the vertical axis represents the difference between the intensity I and the average pre-flare intensity $I_{\mathrm{p-f}}$.

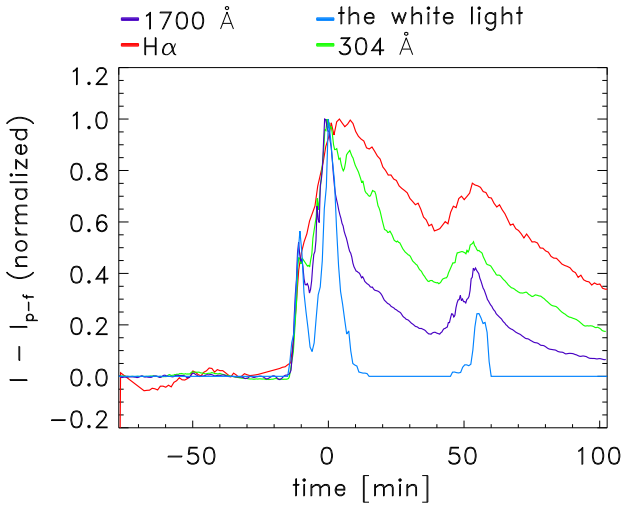

(a) Lightcurves for the white light, Hα, 1 700 Å and 304 Å.

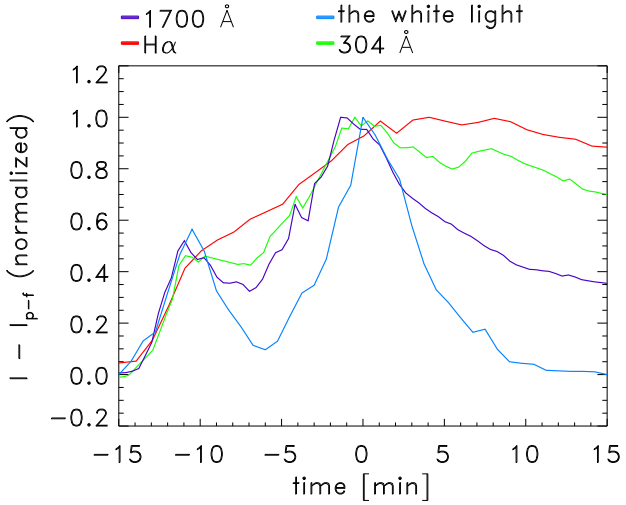

(b) Lightcurves for the white light, Hα, 1 700 Å and 304 Å zoomed in at the maximum of the WL emission.

Figure 4.1: Lightcurves for the X5.4 solar flare on 2012 March 07 with its maximum at 00:24 UT.

As it can be seen in Figure 4.1 and figures in Attachment A.1, the lightcurve for 1 700Å resembles the most the one in the WL. For that reason, we study whether the emission at 1 700Å precedes or lags behind the emission in the WL by comparing the time of their lightcurve maxima. Results of this analysis can be seen in Table 4.2. Then we compare the positions of enhancements in the WL and at 1 700Å using the videos where we can observe all the studied channels at the same time. These videos are in the electronic attachment. Selected images from the videos are shown in Attachment A.2.

Date	Time [UT]	Class	First emission
2017 September 06	12:02	X9.3	1 700
2012 March 07	00:24	X5.4	1 700
2013 November 05	22:12	X3.3	1 700
2014 October 24	21:41	X3.1	1 700
2011 February 15	01:56	X2.2	1 700
2011 September 06	22:20	X2.1	1 700
2014 October 26	10:56	X2.0	WL
2014 December 20	00:28	X1.8	1 700
2011 September 07	22:38	X1.8	1 700
2014 October 22	14:28	X1.6	1 700
2012 March 07	01:14	X1.3	1 700
2011 July 30	02:09	M9.3	1 700
2011 August 04	03:57	M9.3	WL
2014 October 22	01:59	M8.7	1 700
2015 June 25	08:16	M7.9	1 700
2014 January 07	10:13	M7.2	1 700
2014 October 27	00:34	M7.1	WL
2012 March 09	03:53	M6.3	1 700
2013 November 01	19:53	M6.3	WL
2012 July 05	11:44	M6.2	1 700
2015 August 24	07:33	M5.6	AIA data missing
2011 September 06	01:50	M5.3	1 700
2014 February 04	04:00	M5.2	1 700
2014 September 28	02:58	M5.1	no 1 700

Table 4.2: Date and time of the maximum of a solar flare, class of a solar flare and the channel where the maximum of intensity appears first

In Table 4.2, we can see that in most cases the emission at 1 700 Å precedes the WL emission. The average time delay is about two minutes. Only for four WLFs, the WL emission precedes the emission at 1 700 Å. For the X2.0 flare on 2014 October 26, even though in Figure A.7, the maximum in the WL appears first, there is a large emission at 1 700 Å during the WL emission and slightly before. In case of the M9.3 flare on 2011 August 04, a smaller peak in the WL precedes the maximum of 1 700 Å as shown in Figure A.13. However, the

main maximum of the WL emission comes after. For the M6.3 flare on 2013 November 01, it is complicated to decide. In Figure A.19, we can see that the WL maximum precedes the 1 700 Å maximum by about half a minute and they appear more or less at the same time. Some emission at 1 700 Å appears before the WL maximum. For the M5.3 flare on 2011 September 06, the WL emission starts before the emission at 1 700 Å, as it can be seen in Figure A.22. But the maximum of 1 700 Å precedes the main WL maximum.

It is not possible to decide for two WLFs. In case of the M5.6 flare on 2015 August 24, data for 1 700 Å and 304 Å are missing before and during the solar flare, which explains their unexpected behavior shown in Figure A.21. After the gap, the data start after the peak of the WL emission making it impossible to decide which emission appears first. Another problematic flare is the M5.1 flare on 2014 September 28. For this flare, we do not see emissions at other wavelength bands near the WL emission in Figure A.24, so it is hard to compare the behavior of the WL with other studied wavelengths. We cannot properly explain their behavior and why we do not see emissions during the WLF.

After analyzing the videos, it seems that enhancements in the WL occur in similar places as enhancements at 1 700 Å. Enhancements at 1 700 Å also often appear at other places. Positions of enhancements at 1 700 Å are connected with places where enhancements in the WL and often at 1 700 Å occur by ribbons that can be observed at 304 Å or in the Hα line. An example is shown in Figure 4.2, where there are images for the M9.3 flare on 2011 July 30 at 02:08:15 UT. We can see that brightenings in the 1 700 Å band occur also in another location and are connected by the Hα ribbon with the location for the WLF.

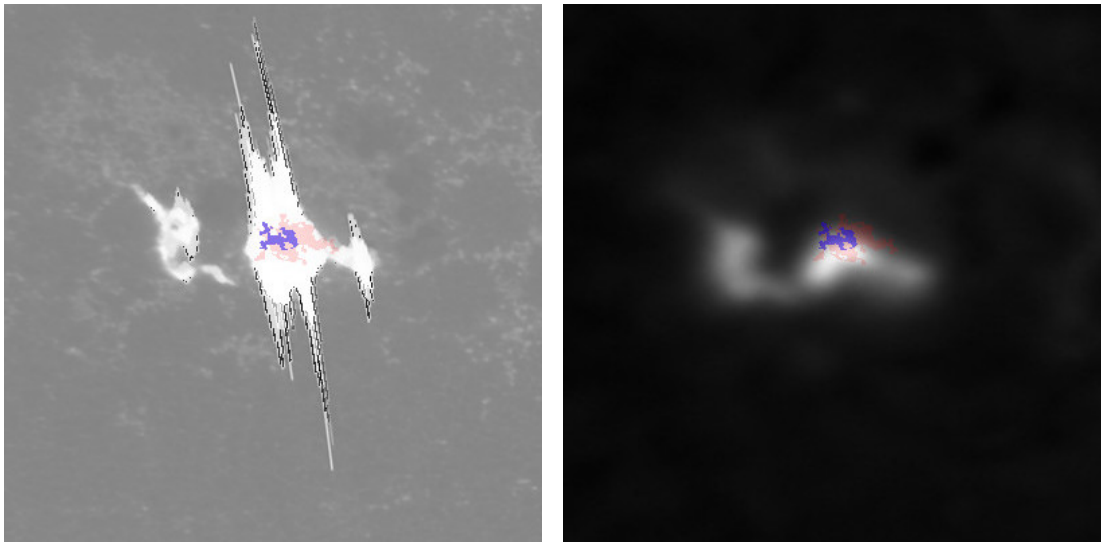

(a) 1 700 Å (b) The Hα line

Figure 4.2: Images for the M9.3 flare on 2011 July 30 at 02:08:15 UT where blue points are WL enhancements detected at this time and red points are all detected WLF points. Images are zoomed in around the flaring region.

The M6.3 flare on 2013 November 01 is an exception and in Figure 4.3, we show images in the 1 700 Å band and in the Hα line at 19:51:00 UT. A very large part of the 1 700 Å emission occurs at similar positions as the WL emission and they

occur on the same 304 Å or the Hα ribbon. However, a small part of the 1 700 Å emission occurs at approximately the same time but in a different place that is marked by the green circle in Figure 4.3a. It does not seem to be on the same ribbon or otherwise connected to the main location. It could also be another flare occurring at the same time.

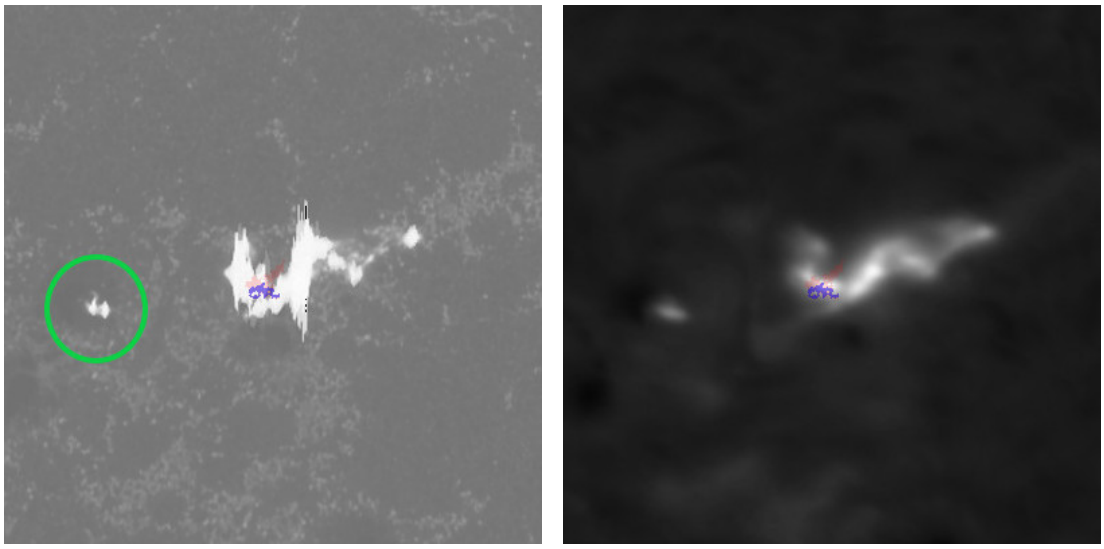

(a) 1 700 Å (b) The Hα line

Figure 4.3: Images for the M6.3 flare on 2013 November 01 at 19:51:00 UT where blue points are WL enhancements detected at this time, red points are all detected WLF points and in the green circle, there is the location of the enhancement at 1 700 Å that is not connected to the WLF by Hα ribbons. Images are zoomed in around the flaring region.

By investigating flares where the emission in the WL precede the 1 700 Å emission we can see that two peaks in the WL emission shown in Figure A.13 for the M9.3 flare on 2011 August 04 correspond to two locations of the WL emission. The second peak clearly corresponds to the location where there is a large emission in the 1 700 Å band. However, there are very small emissions at 1 700 Å around the place with enhancements corresponding to the first WL peak. For the X2.0 flare on 2014 October 26 and the M7.1 flare on 2014 October 27 the situation is quite similar. Enhancements in the 1 700 Å band appear at various locations and some of them are more or less the same as the locations of the WL emission. Nonetheless, the strongest enhancements occur in places where there is no WL emission detected. For the M6.3 flare on 2013 November 01, they appear at similar places.

4.2 Decay time of WLFs

The mean lightcurves and histograms of decay times are shown in Attachment A.3. As an example, there is the mean lightcurve and histogram for the X9.3 flare on 2017 September 06 shown in Figure 4.4. The intensity on the vertical axis is normalized to the first point. It can be seen in Figure 4.4a and in the figures in Attachment A.3 that error bars are huge and it suggests

that there is a big variation in the lightcurves of WLF points. Fitted decay times for mean lightcurves of every WLF are listed in Table 4.3 with their errors. The average value of decay time is about seven minutes if we do not count the value for the M7.1 flare on 2014 October 27 as this value is clearly very different from others. However, the errors are huge for most of the flares so the real decay times can vary from the fitted ones. It could be caused by a significant variation in lightcurves of WLF points. Also, the errors strongly depend on the conditions that were used to select appropriate WLF points and on the fitted time. If we slightly changed, for instance, the required time distance between the maximum of lightcurves of WLF points and the total lightcurve, for certain flares the errors could change by the whole order.

To evaluate the fit goodness, we also plotted residuum differences, where on the vertical axis there is the difference between the observed and the fitted intensity divided by the deviation of the fitted point. These plots are shown in Attachment A.3. There are flares, such as the X3.1 flare on 2014 October 24 in Figure A.52b, where the points appear to be randomly scattered and the difference between the fit and the observation is not very significant. However, there are flares where the residuum differences show apparent trends. A good example of this behavior is in Figure A.63b for the M7.9 flare on 2015 June 25. We can clearly see the points in Figure A.63b are not scattered randomly but increase and decrease in time, which indicates that the intensity does not depend exponentially on time.

Therefore, we used another approach to determine the typical decay of WLFs and we studied histograms of decay times of WLF points. According to these histograms, the typical decay time for WLF points is about 2 – 3 min. But there are also a lot of points where the decay time is much longer and reaches the orders of tens of minutes.

There are also histograms where there is a very small number of spatial points to provide credible information about the decay time. The numbers of spatial points for each WLF are listed in Table 4.1. However, the number of spatial points used to create histograms is lower due to the conditions that they have to fulfill and are mentioned in Section 3.4. As a result, histograms for certain flares contain a very low number of points to get a real estimation of the typical decay time. A good example is the histogram in Figure A.89 for the M7.1 flare on 2014 October 27 containing only ten points.

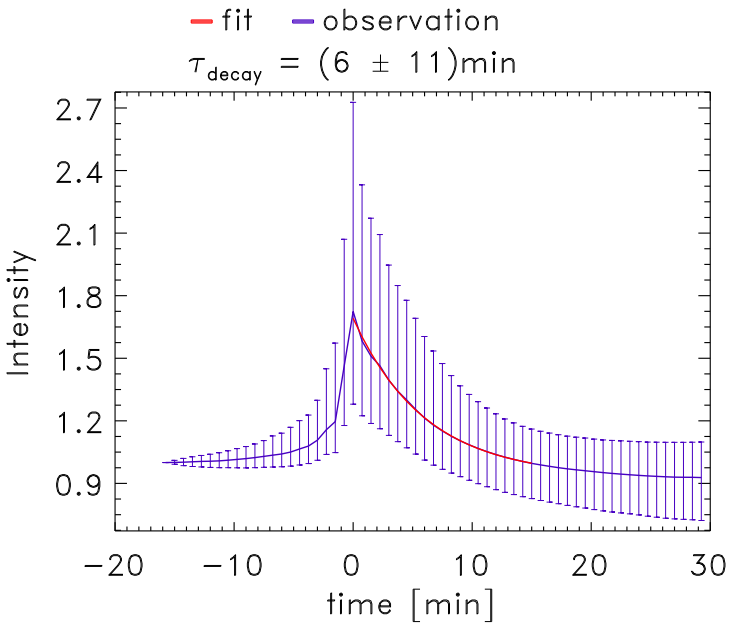

(a) Mean lightcurve of WLF points.

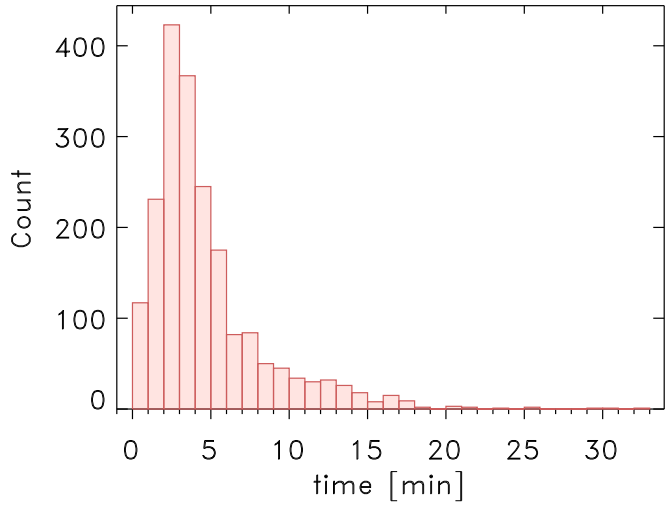

(b) Histogram of decay times of WLF points.

Figure 4.4: Mean lightcurve and histogram of decay times of WLF points for the X9.3 solar flare on 2017 September 06 with the solar flare maximum at 12:02 UT.

Date	Time [UT]	Class	Decay time [min]
2017 September 06	12:02	X9.3	6 ± 11
2012 March 07	00:24	X5.4	5 ± 8
2013 November 05	22:12	X3.3	2 ± 2
2014 October 24	21:41	X3.1	7 ± 14
2011 February 15	01:56	X2.2	13 ± 41
2011 September 06	22:20	X2.1	4 ± 6
2014 October 26	10:56	X2.0	7 ± 13
2014 December 20	00:28	X1.8	7 ± 10
2011 September 07	22:38	X1.8	4 ± 5
2014 October 22	14:28	X1.6	2.1 ± 0.8
2012 March 07	01:14	X1.3	8.3 ± 0.2
2011 July 30	02:09	M9.3	3 ± 3
2011 August 04	03:57	M9.3	6 ± 10
2014 October 22	01:59	M8.7	18 ± 65
2015 June 25	08:16	M7.9	6 ± 6
2014 January 07	10:13	M7.2	5 ± 7
2014 October 27	00:34	M7.1	81 ± 126
2012 March 09	03:53	M6.3	12 ± 22
2013 November 01	19:53	M6.3	15 ± 37
2012 July 05	11:44	M6.2	3 ± 3
2015 August 24	07:33	M5.6	3 ± 3
2011 September 06	01:50	M5.3	11 ± 15
2014 February 04	04:00	M5.2	7.87 ± 0.03
2014 September 28	02:58	M5.1	4 ± 4

Table 4.3: Date and time of the maximum of a solar flare, class of a solar flare, fitted decay time and its error for mean lightcurves.

4.3 HMI measurement filters

We analyzed emissions in HMI filters for the X9.3 solar flare on 2017 September 06 only. The mask difference time evolution is shown in Figure 4.5. It can be seen that the biggest difference between the emission in filters and the emission in the reconstructed continuum occurs in the filters -17.2 pm and $+17.2$ pm that are the most distant from the center of the Fe I line (6173 Å) line. The difference appears to be smaller for filters closer to the center of the line. It could mean that emissions observed in the reconstructed continuum are influenced by the Fe I line and are not entirely the real visible continuum. If we observed strictly the real continuum in HMI filtergrams, then the emission in the filters further from the center of the line should resemble more the emission in the reconstructed continuum.

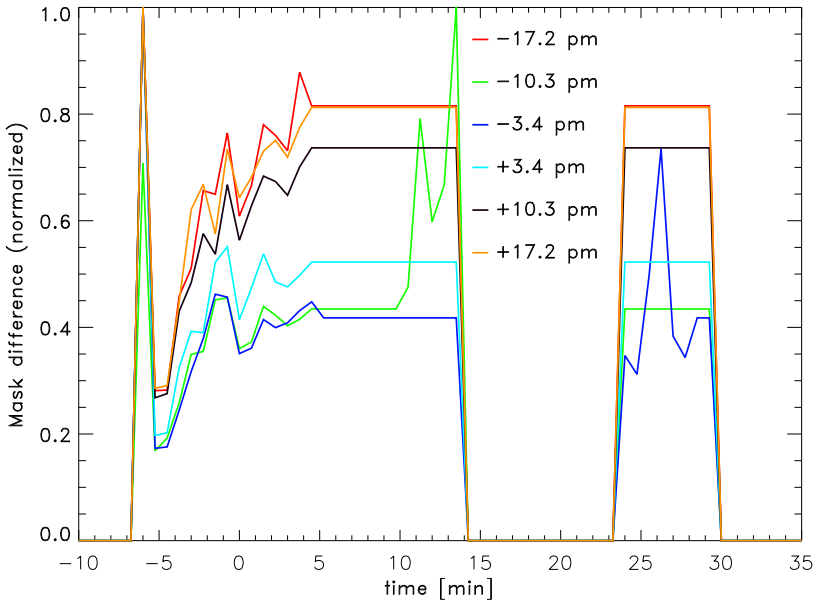

Figure 4.5: The time evolution of filter mask differences for the X9.3 solar flare on 2017 September 06.

5. Discussion

5.1 Correspondence of the WL emission and brightenings in other wavelength channels

By studying lightcurves of different wavelength bands, we see that the lightcurve for 1 700 Å is very similar to the WL continuum lightcurve. However, the maximum of the emission at 1 700 Å often appears before the WL maximum. The AIA 1 700 Å band should observe the temperature minimum region and the upper photosphere. But during flares, we could also observe a strong contribution from the chromospheric lines as it was stated in Section 2.3.1. If the WL continuum has its origin in the photosphere, we would expect to see the emission at 1 700 Å before the WL as solar flares start in the corona and their impact spread downwards through the solar atmosphere. Nonetheless, it is still not certain where in the solar atmosphere WLFs originate and what height we observe at 1 700 Å, hence it is hard to tell which emission should occur first. According to figures in Attachment A.1, it appears that places where emissions at 1 700 Å occur are reached sooner and could, therefore, be generated higher in the atmosphere, or the conditions required for emissions at 1 700 Å are created sooner. It means that potentially the WL and 1 700 Å emissions could occur at the same height but conditions to generate emissions at 1 700 Å are met faster.

When we study the positions of enhancements at 1 700 Å and in the detected WL continuum we can see that they often appear at similar places. However, enhancements in the 1 700 Å band often occur also at other locations. There are many reasons as to why we do not observe the WL emission there. The simplest one is that it just did not occur there. It could be possible that high-energy electrons accelerated in the reconnection point did not reach deeper places of the solar atmosphere where conditions were right for the emission in the WL to occur. In that case, we would have to assume that WLFs are truly generated by electron beams. In addition, this effect would be more marginal, if the emission at 1 700 Å really has a large contribution from chromospheric lines that was mentioned in Section 2.3.1. There might be also another reason and it could be associated with the method of detecting WLFs. WLFs appear in HMI filtergrams as small brightenings and are best observed in sunspots that are much darker than the quiet Sun. Enhancements at 1 700 Å are also observable in areas of the quiet Sun or almost the quiet Sun. So it is possible that WLFs are not detectable in HMI filtergrams in these places as the relative intensity increase is very subtle.

Nevertheless, in the videos of different channels, we can see that the positions of 1 700 Å enhancements are connected with the positions of WLFs by ribbons observed in the 304 Å and in the Hα line. This fact supports the theory that emissions at 1 700 Å and in the WL are associated with each other. It suggests that both of them have the same original source and we usually just observe the emission at 1 700 Å first because the information from the reconnection point came to the places with 1 700 Å emissions sooner. It could mean that we see higher places of the atmosphere in the 1 700 Å band than in the detected WL. However, we would need to have the model of the solar atmosphere during the solar flare to be able to confirm this theory. The model would have to be more

complex than a 1D model of the solar atmosphere as it cannot explain such delays. The electron velocity is too large and in 1D models, they would travel the distance in less than a second. Hence, we would not observe the delay between the emission at 1 700 Å and in the WL. We would also have to study each point of the 1 700 Å emission individually, determine its distance from the detected WLF and the delay between its emission and the WL emission.

5.2 Decay time

In the figures in Attachment 4.2, we can see that errors for the mean lightcurves are extremely large. It is probably caused by a large variation in lightcurves of WLF points. These errors were used when fitting the mean lightcurve by an exponential function and thus contribute to large errors of the fitted decay time that are listed in Table 4.3. In addition, these errors also heavily depend on the conditions that were used to select appropriate WLF points. Therefore, the estimation of the typical decay time by studying the mean lightcurves is not very accurate.

By analyzing the histograms of WLF points, we can see that most of the points have the typical decay time in the range of 2 – 3 min. There are also points where the typical decay time reaches the order of tens of minutes. Decay times of the order of minutes are expected and are obtained in other studies. For instance, in the work [50] they studied the X2.1 solar flare on 2011 September 06 and obtained similar results. Their decay times for WL kernels range in the order of minutes.

One must be also careful when interpreting the low decay times. Data contain cut-offs at smaller timescales due to the HMI cadence of 45 s and due to the requirement of WLFs lasting at least three minutes. The latter requirement is introduced in the method for WLF detection and is mentioned in Section 3.1. It is clear that due to the cadence of 45 s we cannot observe anything with shorter timescales. But it is not sure how exactly the requirement of WLFs lasting at least three minutes affects these results. As the typical decay time is more or less the same as the required lasting time of WLFs it is possible that found decay times are somehow biased by this condition. It would require further analysis to conclude these effects. However, the condition cannot be softened significantly as it would cause the program detecting random fluctuations as WLFs.

5.3 HMI filters

As it was mentioned in Section 4.3, the smallest difference between filter emissions and the reconstructed continuum is in the filters that are close to the center line. It suggests that we may not observe emissions in the real visible continuum in HMI filtergrams, but rather artifacts of the method used to reconstruct the continuum from measurements of the Fe I line. There can be emissions or asymmetries in the line that are responsible for the emission detected in HMI filtergrams. Even though the biggest difference is for the filters −17.2 pm and +17.2 pm, there are a lot of detected points in these filters during the detected WLF. Furthermore, emissions are detected in all of the filters. So it appears that at least some part

of the emission detected in the reconstructed continuum could really belong to a real WLF. As it was mentioned in Section 2.3.2, in the work [48] they concluded that enhancements in HMI filtergrams can be caused by both the real continuum and the behavior in the Fe I line and we cannot distinguish these two situations without knowing the real profile of the Fe I line.

Conclusions

We analyzed 24 WLFs detected by our program. These WLFs correspond to solar flares that occurred after 2010. The strongest solar flare is of class X9.3 and the weakest is of class M5.1. For detection of WLFs, we used SDO/HMI continuum filtergrams. For analysis of WLFs, we used SDO/AIA 1 700 Å and 304 Å bands and Hα images from GONG.

First, we analyzed lightcurves of WLFs and discovered that during the detected WLFs, there is always an emission in the other bands with only one exception of the M5.1 flare on 2014 September 28. The lightcurve of the 1 700 Å band resembles the WL lightcurve the most but the emission usually starts a few minutes before the WL. It suggests that either the emission in the 1 700 Å band occur higher in the solar atmosphere than the WL continuum, or conditions required to generate emissions at 1 700 Å are created faster. Hence, the emission at 1 700 Å and in the WL possibly occur at the same height in the solar atmosphere, or the WL emission occurs a little deeper.

Then we compare the positions of 1 700 Å enhancements with the positions of the WL enhancements. They appear at similar places but enhancements at 1 700 Å could appear also elsewhere. However, these positions are connected by ribbons seen in the 304 Å band and in the Hα line. So it seems that emissions in the WL and at 1 700 Å have their origin in the same source and it just usually gets sooner to places where the 1 700 Å band is generated.

We also found the typical decay time for WLFs. At first, we used the mean lightcurves but the errors of decay times were too large. Therefore, we fitted directly lightcurves of WLF points and thus obtained a set of decay times for each WLF. Then by studying histograms of decay times of WLF points, we estimated that the typical decay time for WLF points is in the interval 2 – 3 min. It was expected to be of the order of minutes as other works have similar results [3][50].

Finally, we looked at filters of the Fe I line (6173 Å) line that HMI measures and which are used to reconstruct the visible continuum. It was done for only the strongest solar flare of class X9.3 that occurred on 2017 September 06. By comparing the emission in filters with the reconstructed continuum, it seems that emissions in filters closer to the center of the line resemble better the emission in the reconstructed continuum. It suggests that the continuum may be contaminated by the behavior of the line. However, we see brightenings in all filters during the emission in the continuum. So at least some part of the emission in the reconstructed continuum could actually belong to the real visible continuum. To sum up, it seems that even though the reconstructed continuum may be influenced by the line, we should also see there some part of the real visible continuum.

Bibliography

[1] K. Shibata and T. Magara. Solar Flares: Magnetohydrodynamic Processes. *Living Reviews in Solar Physics*, 8:6, Dec 2011.

[2] H. Potts, H. Hudson, L. Fletcher, and D. A. Diver. The optical depth of white-light flare continuum. *The Astrophysical Journal*, 722, 04 2010.

[3] G. S. Kerr and L. Fletcher. Physical Properties of White-light Sources in the 2011 February 15 Solar Flare. *The Astrophysical Journal*, 783:98, March 2014.

[4] H. S. Hudson, C. J. Wolfson, and T. R. Metcalf. White-light flares: A trace/rhessi overview. *Solar Physics*, 234(1):79–93, March 2006.

[5] L. Kleint, P. Heinzel, P. Judge, and S. Krucker. Continuum Enhancements in the Ultraviolet, the Visible and the Infrared during the X1 Flare on 2014 March 29. *The Astrophysical Journal*, 816(2):88, January 2016.

[6] L. Mravcová and M. Švanda. Automatic detection of white-light flare kernels in SDO/HMI intensitygrams. *New Astronomy*, 57:14–21, November 2017.

[7] D. H. Hathaway. Why We Study The Sun, 2014. `https://solarscience.msfc.nasa.gov/whysolar.shtml` [Last access: 2019 April 02].

[8] D. H. Hathaway. The Solar Interior, 2015. `https://solarscience.msfc.nasa.gov/interior.shtml` [Last access: 2019 April 03].

[9] M. Brož, M. Šolc. *Fyzika sluneční soustavy.* Matfyzpress, Praha, 2013.

[10] Our Star the Sun. `https://soho.nascom.nasa.gov/explore/` [Last access: 2019 April 03.

[11] The Sun. `https://lco.global/spacebook/sun/` [Last access: 2019 May 02].

[12] D. H. Hathaway. The Photosphere, 2014. `https://solarscience.msfc.nasa.gov/surface.shtml` [Last access: 2019 April 03].

[13] D. H. Hathaway. The Chromosphere, 2014. `https://solarscience.msfc.nasa.gov/chromos.shtml` [Last access: 2019 April 03].

[14] D. H. Hathaway. The Transition Region, 2014. `https://solarscience.msfc.nasa.gov/t_region.shtml` [Last access: 2019 April 03].

[15] D. H. Hathaway. The Corona, 2014. `https://solarscience.msfc.nasa.gov/corona.shtml` [Last access: 2019 April 03].

[16] Solar Activity. `https://helios.gsfc.nasa.gov/solaract.html` [Last access: 2019 April 03].

[17] D. H. Hathaway. Photospheric Features, 2014. `https://solarscience.msfc.nasa.gov/feature1.shtml` [Last access: 2019 April 03].

[18] D. H. Hathaway. Chromospheric Features, 2014. https://solarscience.msfc.nasa.gov/feature2.shtml [Last access: 2019 April 04].

[19] D. H. Hathaway. Coronal Features, 2014. https://solarscience.msfc.nasa.gov/feature3.shtml [Last access: 2019 April 04].

[20] D. H. Hathaway. Coronal Mass Ejections, 2014. https://solarscience.msfc.nasa.gov/CMEs.shtml [Last access: 2019 April 04].

[21] Sun. https://en.wikipedia.org/wiki/Sun. [Last access: 2019 April 03].

[22] A. O. Benz. Flare observations. *Living Reviews in Solar Physics*, 14(1):2, Dec 2016.

[23] P. Heinzel. Sluneční erupce, 2013. http://pozorovanislunce.eu/odborne-clanky/slunecni-erupce.html [Last access: 2019 April 04].

[24] Reconnection on the Sun. https://www.nasa.gov/content/goddard/reconnection-on-the-sun [Last access: 2019 April 04].

[25] K. R. Lang. Solar Flares in Varying Perspectives, 2010. http://ase.tufts.edu/cosmos/view_picture.asp?id=178 [Last access: 2019 April 04].

[26] What are solar flares? https://www.spaceweatherlive.com/en/help/what-are-solar-flares. [Last access: 2019 April 04].

[27] The Classification of X-ray Solar Flares. http://spaceweather.com/glossary/flareclasses.html [Last access: 2019 May 05].

[28] D. B. Jess, M. Mathioudakis, P. J. Crockett, and F. P. Keenan. Do All Flares Have White-Light Emission? *The Astrophysical Journal Letters*, 688:L119, December 2008.

[29] M. Kretzschmar. The Sun as a star: observations of white-light flares. *Astronomy & Astrophysics*, 530:A84, June 2011.

[30] L. Fletcher, I. G. Hannah, H. S. Hudson, and T. R. Metcalf. A TRACE White Light and RHESSI Hard X-Ray Study of Flare Energetics. *The Astrophysical Journal*, 656:1187–1196, February 2007.

[31] K. Watanabe, S. Krucker, H. Hudson, T. Shimizu, S. Masuda, and K. Ichimoto. G-band and Hard X-ray Emissions of the 2006 December 14 Flare Observed by Hinode/SOT and Rhessi. *The Astrophysical Journal*, 715:651–655, May 2010.

[32] C. Fang and M. D. Ding. On the spectral characteristics and atmospheric models of two types of white-light flares. *Astronomy and Astrophysics Supplement Series*, 110:99, April 1995.

[33] Lucia Kleint, Petr Heinzel, and Säm Krucker. On the Origin of the Flare Emission in IRIS' SJI 2832 Filter:Balmer Continuum or Spectral Lines? *The Astrophysical Journal*, 837:160, Mar 2017.

[34] V. Yurchyshyn, P. Kumar, V. Abramenko, Y. Xu, P. R. Goode, K. S. Cho, and E. K. Lim. High-resolution Observations of a White-light Flare with NST. *The Astrophysical Journal*, 838:32, March 2017.

[35] J. Jurčák, J. Kašparová, M. Švand a, and L. Kleint. Heating of the solar photosphere during a white-light flare. *Astronomy & Astrophysics*, 620:A183, December 2018.

[36] N. Hurlburt, M. Cheung, C. Schrijver, L. Chang, S. Freeland, S. Green, C. Heck, A. Jaffey, A. Kobashi, D. Schiff, J. Serafin, R. Seguin, G. Slater, A. Somani, and R. Timmons. Heliophysics Event Knowledgebase for the Solar Dynamics Observatory (SDO) and Beyond. *Solar Physics*, 275:67–78, 2012.

[37] P. H. Scherrer, J. Schou, R. I. Bush, A. G. Kosovichev, R. S. Bogart, J. T. Hoeksema, Y. Liu, T. L. Duvall, J. Zhao, A. M. Title, C. J. Schrijver, T. D. Tarbell, and S. Tomczyk. The helioseismic and magnetic imager (hmi) investigation for the solar dynamics observatory (sdo). *Solar Physics*, 275(1):207–227, January 2012.

[38] J. Schou, P. H. Scherrer, R. I. Bush, R. Wachter, S. Couvidat, M. C. Rabello-Soares, R. S. Bogart, J. T. Hoeksema, Y. Liu, T. L. Duvall, D. J. Akin, B. A. Allard, J. W. Miles, R. Rairden, R. A. Shine, T. D. Tarbell, A. M. Title, C. J. Wolfson, D. F. Elmore, A. A. Norton, and S. Tomczyk. Design and ground calibration of the helioseismic and magnetic imager (hmi) instrument on the solar dynamics observatory (sdo). *Solar Physics*, 275(1):229–259, January 2012.

[39] S. Couvidat, J. Schou, J. T. Hoeksema, R. S. Bogart, R. I. Bush, T. L. Duvall, Y. Liu, A. A. Norton, and P. H. Scherrer. Observables processing for the helioseismic and magnetic imager instrument on the solar dynamics observatory. *Solar Physics*, 291(7):1887–1938, August 2016.

[40] J. W. Harvey, F. Hill, R. P. Hubbard, J. R. Kennedy, J. W. Leibacher, J. A. Pintar, P. A. Gilman, R. W. Noyes, A. M. Title, J. Toomre, R. K. Ulrich, A. Bhatnagar, J. A. Kennewell, W. Marquette, J. Patrón, O. Saá, and E. Yasukawa. The global oscillation network group (gong) project. *Science*, 272(5266):1284–1286, 1996.

[41] J. W. Harvey, J. Bolding, R. Clark, D. Hauth, F. Hill, R. Kroll, G. Luis, N. Mills, T. Purdy, C. Henney, D. Holland, and J. Winter. Full-disk Solar H-alpha Images From GONG. In *AAS/Solar Physics Division Abstracts #42*, AAS/Solar Physics Division Meeting, page 17.45, May 2011.

[42] Paul Boerner, Christopher Edwards, James Lemen, Adam Rausch, Carolus Schrijver, Richard Shine, Lawrence Shing, Robert Stern, Theodore Tarbell, Alan Title, C. Jacob Wolfson, Regina Soufli, Eberhard Spiller, Eric Gullikson, David McKenzie, David Windt, Leon Golub, William Podgorski, Paola Testa, and Mark Weber. Initial calibration of the atmospheric imaging assembly (aia) on the solar dynamics observatory (sdo). *Solar Physics*, 275(1):41–66, January 2012.

[43] James R. Lemen, Alan M. Title, David J. Akin, Paul F. Boerner, Catherine Chou, Jerry F. Drake, Dexter W. Duncan, Christopher G. Edwards, Frank M. Friedlaender, Gary F. Heyman, Neal E. Hurlburt, Noah L. Katz, Gary D. Kushner, Michael Levay, Russell W. Lindgren, Dnyanesh P. Mathur, Edward L. McFeaters, Sarah Mitchell, Roger A. Rehse, Carolus J. Schrijver, Larry A. Springer, Robert A. Stern, Theodore D. Tarbell, Jean-Pierre Wuelser, C. Jacob Wolfson, Carl Yanari, Jay A. Bookbinder, Peter N. Cheimets, David Caldwell, Edward E. Deluca, Richard Gates, Leon Golub, Sang Park, William A. Podgorski, Rock I. Bush, Philip H. Scherrer, Mark A. Gummin, Peter Smith, Gary Auker, Paul Jerram, Peter Pool, Regina Soufli, David L. Windt, Sarah Beardsley, Matthew Clapp, James Lang, and Nicholas Waltham. The atmospheric imaging assembly (aia) on the solar dynamics observatory (sdo). *Solar Physics*, 275(1):17–40, January 2012.

[44] Recent Views of the Sun. `https://smithsonian-eclipse-app.simulationcurriculum.com/recent-views-of-the-sun.html` [Last access: 2019 May 05].

[45] P. J. A. Simões, H. A. S. Reid, R. O. Milligan, and L. Fletcher. The Spectral Content of SDO/AIA 1600 and 1700 Å Filters from Flare and Plage Observations. *The Astrophysical Journal*, 870:114, January 2019.

[46] C. Lindsey and A. C. Donea. What can he ii 304 Å tell us about transient seismic emission from solar flares? *Proceedings of the International Astronomical Union*, 12(S327):113–116, 2016.

[47] P. J. A. Simões, L. Fletcher, N. Labrosse, and G. S. Kerr. Observations and Modelling of Helium Lines in Solar Flares. In I. Dorotovic, C. E. Fischer, and M. Temmer, editors, *Coimbra Solar Physics Meeting: Ground-based Solar Observations in the Space Instrumentation Era*, volume 504 of *Astronomical Society of the Pacific Conference Series*, page 197, April 2016.

[48] M. Švanda, J. Jurčák, J. Kašparová, and L. Kleint. Understanding the HMI pseudocontinuum in white-light solar flares. *The Astrophysical Journal*, 860(2):144, jun 2018.

[49] Thomas H. Cormen, Clifford Stein, Ronald L. Rivest, and Charles E. Leiserson. *Introduction to Algorithms*. McGraw-Hill Higher Education, 2nd edition, 2001.

[50] T. Kawate, T. T. Ishii, Y. Nakatani, K. Ichimoto, A. Asai, S. Morita, and S. Masuda. Temporal Evolution and Spatial Distribution of White-light Flare Kernels in a Solar Flare. *The Astrophysical Journal*, 833(1):50, December 2016.

List of Figures

List of Tables

List of Abbreviations

AIA – Atmospheric Imaging Assembly
BFS – breadth-first search
CME – coronal mass ejection
EUV – extreme ultraviolet
GOES – Geostationary Operational Environmental Satellite
GONG – Global Oscillation Network Group
HMI – Helioseismic and Magnetic Imager
HXR – hard X-ray
JSOC – Joint Science Operations Center
NASA – National Aeronautics and Space Administration
SDO – Solar Dynamics Observatory
SXR – soft X-ray
UV – ultraviolet
WL – white light
WLF – white-light flare

A. Attachments

A.1 Lightcurves

In the following figures, there are lightcurves in the WL, Hα, 1 700 Å, and 304 Å for all the detected WLFs. The quantity on the vertical axis represents the difference between the intensity I and the average pre-flare intensity $I_{\mathrm{p-f}}$. Figures (a) contain the full time-dependence of three hours, whereas figures (b) are zoomed in at the maximum of the WL emission. We can see the lightcurves in the interval ± 15 min around the WL maximum.

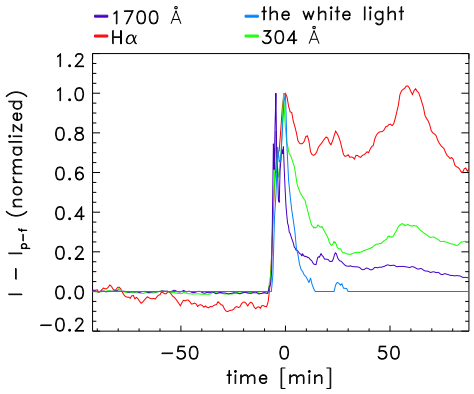

(a) Light curves for the white light, Hα, 1 700 Å and 304 Å.

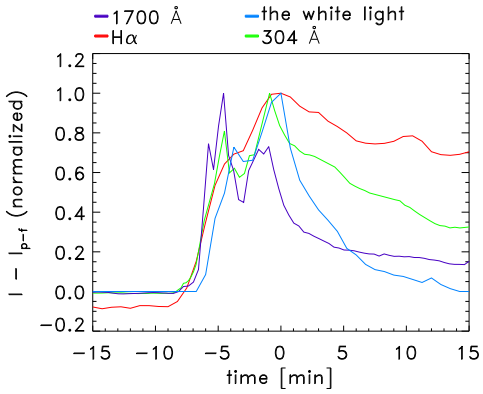

(b) Light curves for the white light, Hα, 1 700 Å and 304 Å zoomed in at the maximum of the WL emission.

Figure A.1: Light curves for the X9.3 solar flare on 2017 September 06 with the solar flare maximum at 12:02 UT.

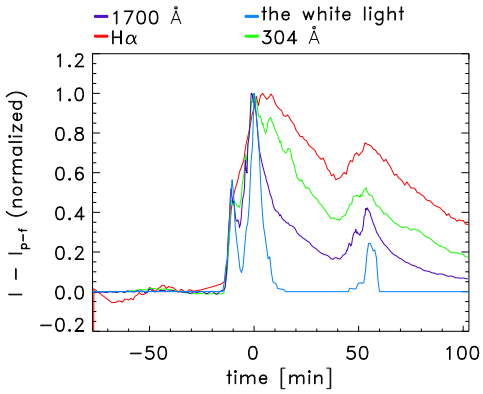

(a) Light curves for the white light, Hα, 1 700 Å and 304 Å.

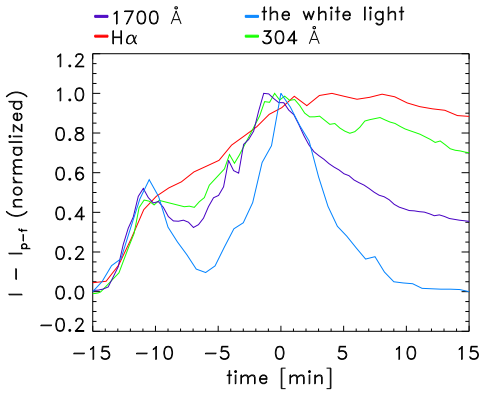

(b) Light curves for the white light, Hα, 1 700 Å and 304 Å zoomed in at the maximum of the WL emission.

Figure A.2: Light curves for the X5.4 solar flare on 2012 March 07 with the solar flare maximum at 00:24 UT.

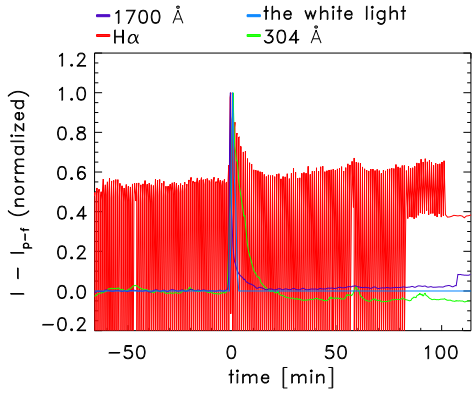

(a) Light curves for the white light, Hα, 1 700 Å and 304 Å.

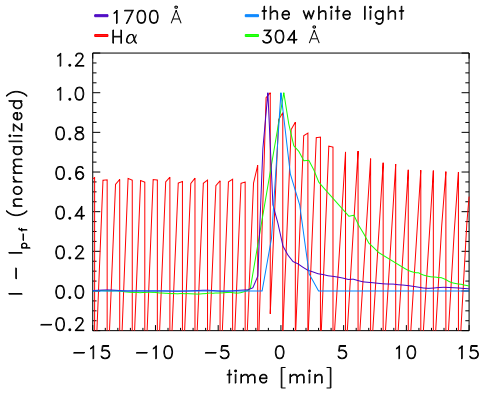

(b) Light curves for the white light, Hα, 1 700 Å and 304 Å zoomed in at the maximum of the WL emission.

Figure A.3: Light curves for the X3.3 solar flare on 2013 November 05 with the solar flare maximum at 22:12 UT.

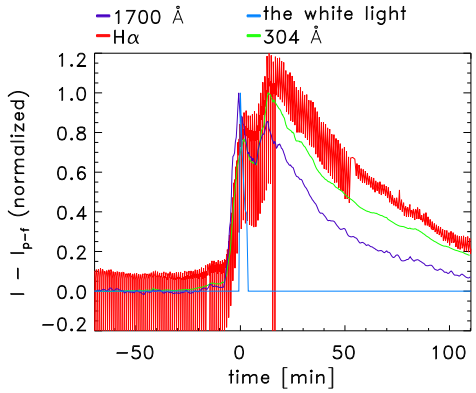

(a) Light curves for the white light, Hα, 1 700 Å and 304 Å.

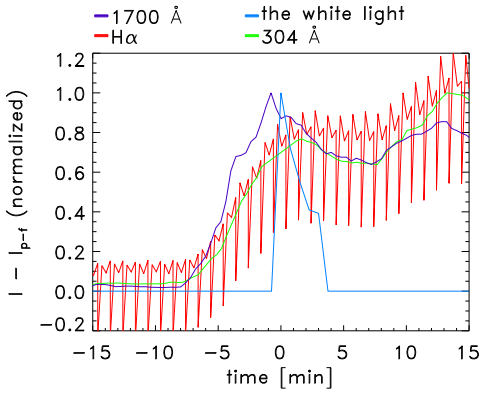

(b) Light curves for the white light, Hα, 1 700 Å and 304 Å zoomed in at the maximum of the WL emission.

Figure A.4: Light curves for the X3.1 solar flare on 2014 October 24 with the solar flare maximum at 21:41 UT.

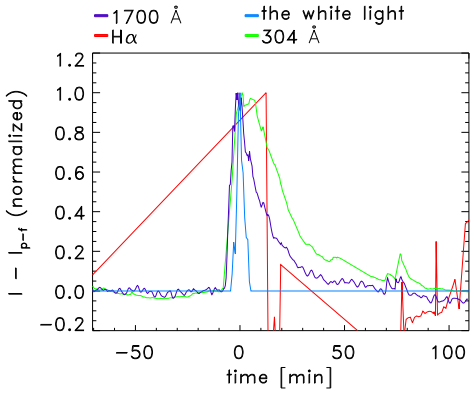

(a) Light curves for the white light, Hα, 1 700 Å and 304 Å.

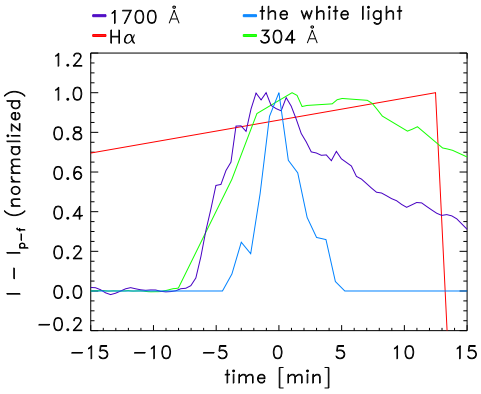

(b) Light curves for the white light, Hα, 1 700 Å and 304 Å zoomed in at the maximum of the WL emission.

Figure A.5: Light curves for the X2.2 solar flare on 2011 February 15 with the solar flare maximum at 01:56 UT.

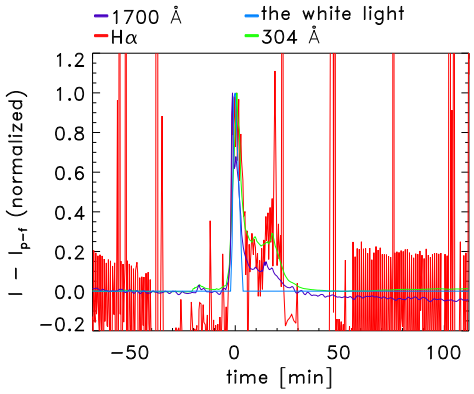

(a) Light curves for the white light, Hα, 1 700 Å and 304 Å.

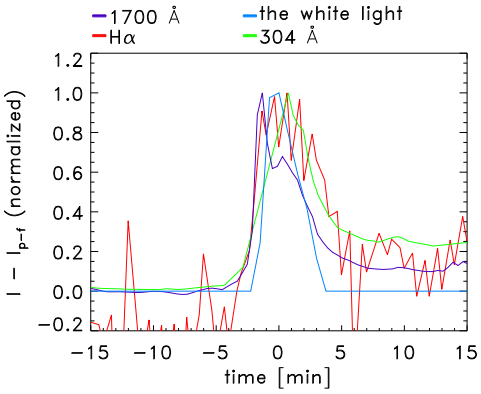

(b) Light curves for the white light, Hα, 1 700 Å and 304 Å zoomed in at the maximum of the WL emission.

Figure A.6: Light curves for the X2.1 solar flare on 2011 September 06 with the solar flare maximum at 22:20 UT.

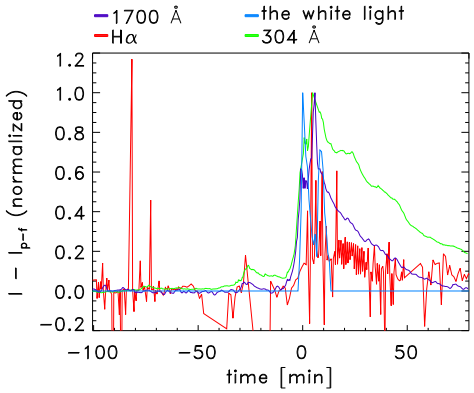

(a) Light curves for the white light, Hα, 1 700 Å and 304 Å.

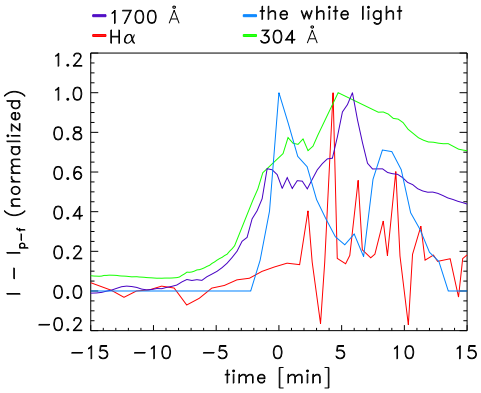

(b) Light curves for the white light, Hα, 1 700 Å and 304 Å zoomed in at the maximum of the WL emission.

Figure A.7: Light curves for the X2.0 solar flare on 2014 October 26 with the solar flare maximum at 10:56 UT.

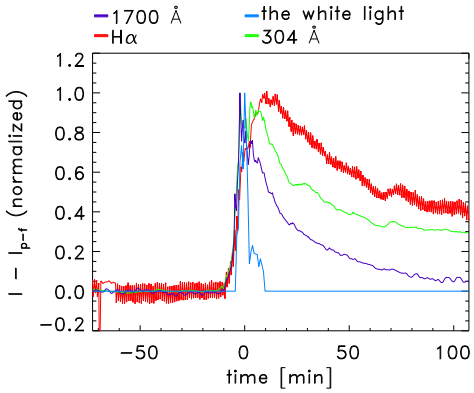

(a) Light curves for the white light, Hα, 1 700 Å and 304 Å.

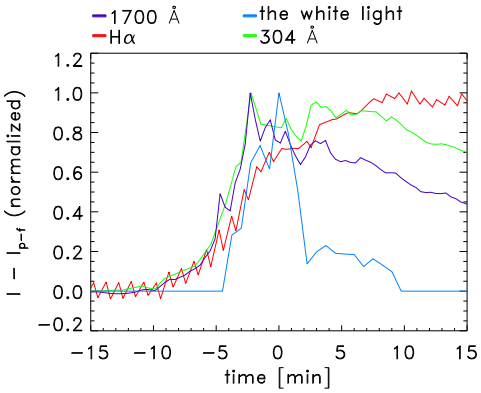

(b) Light curves for the white light, Hα, 1 700 Å and 304 Å zoomed in at the maximum of the WL emission.

Figure A.8: Light curves for the X1.8 solar flare on 2014 December 20 with the solar flare maximum at 00:28 UT.

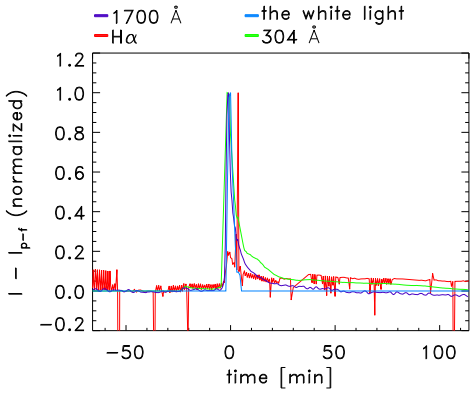

(a) Light curves for the white light, Hα, 1 700 Å and 304 Å.

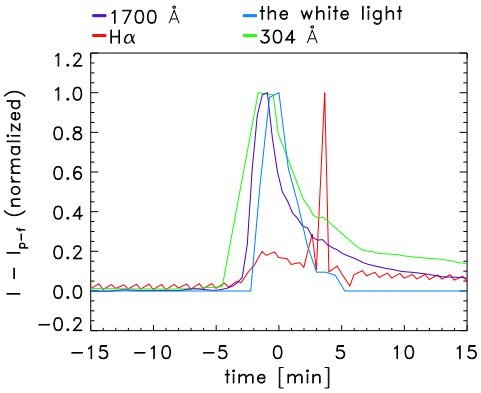

(b) Light curves for the white light, Hα, 1 700 Å and 304 Å zoomed in at the maximum of the WL emission.

Figure A.9: Light curves for the X1.8 solar flare on 2011 September 07 with the solar flare maximum at 22:38 UT.

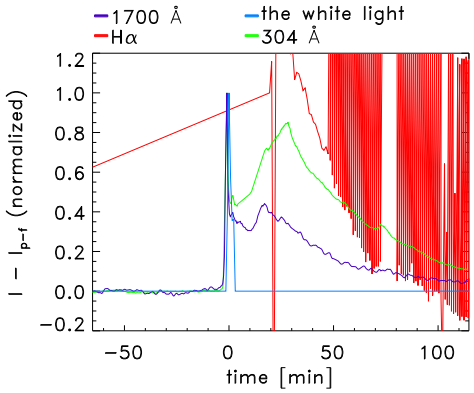

(a) Light curves for the white light, Hα, 1 700 Å and 304 Å.

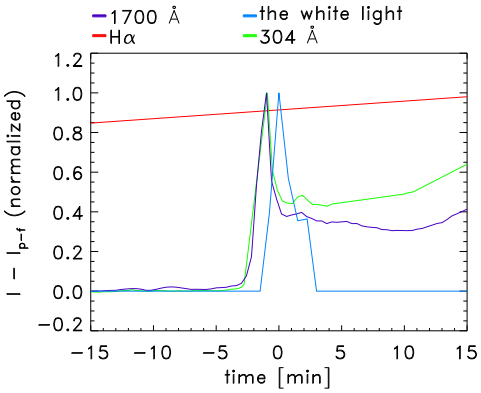

(b) Light curves for the white light, Hα, 1 700 Å and 304 Å zoomed in at the maximum of the WL emission.

Figure A.10: Light curves for the X1.6 solar flare on 2014 October 22 with the solar flare maximum at 14:28 UT.

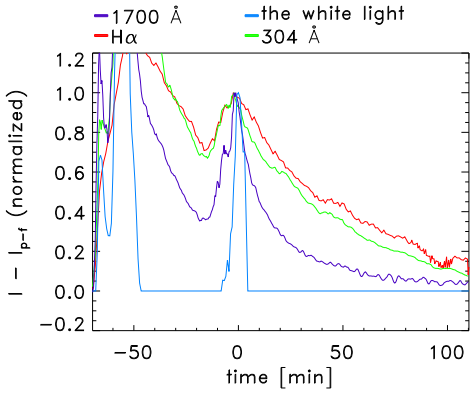

(a) Light curves for the white light, Hα, 1 700 Å and 304 Å.

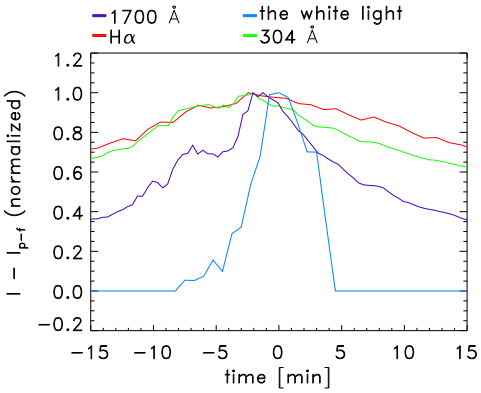

(b) Light curves for the white light, Hα, 1 700 Å and 304 Å zoomed in at the maximum of the WL emission.

Figure A.11: Light curves for the X1.3 solar flare on 2012 March 07 with the solar flare maximum at 01:14 UT.

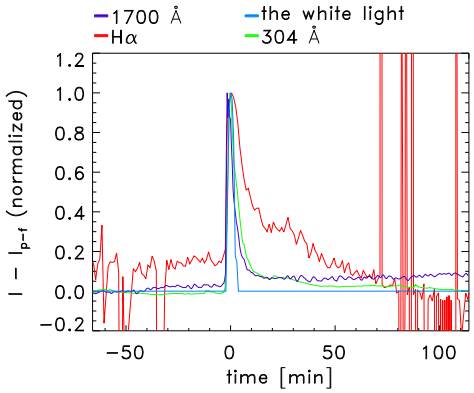

(a) Light curves for the white light, Hα, 1 700 Å and 304 Å.

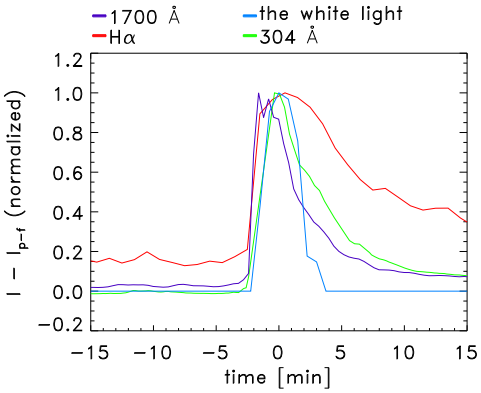

(b) Light curves for the white light, Hα, 1 700 Å and 304 Å zoomed in at the maximum of the WL emission.

Figure A.12: Light curves for the M9.3 solar flare on 2011 July 30 with the solar flare maximum at 02:09 UT.

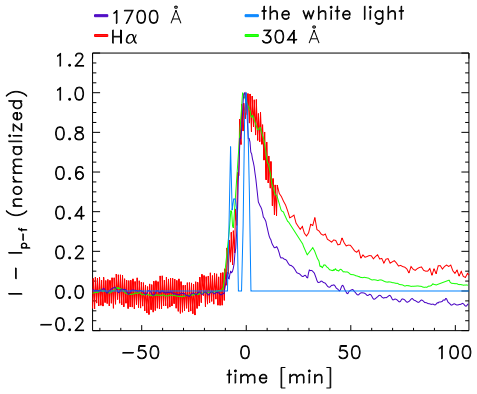

(a) Light curves for the white light, Hα, 1 700 Å and 304 Å.

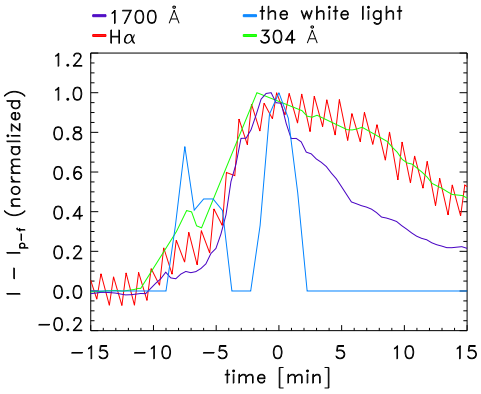

(b) Light curves for the white light, Hα, 1 700 Å and 304 Å zoomed in at the maximum of the WL emission.

Figure A.13: Light curves for the M9.3 solar flare on 2011 August 04 with the solar flare maximum at 03:57 UT.

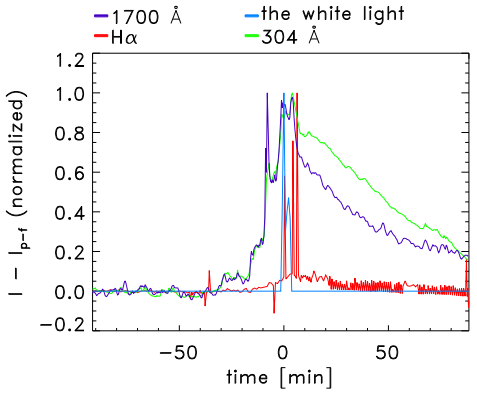

(a) Light curves for the white light, Hα, 1 700 Å and 304 Å.

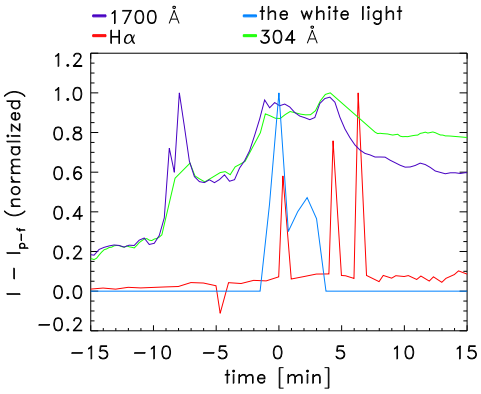

(b) Light curves for the white light, Hα, 1 700 Å and 304 Å zoomed in at the maximum of the WL emission.

Figure A.14: Light curves for the M8.7 solar flare on 2014 October 22 with the solar flare maximum at 01:59 UT.

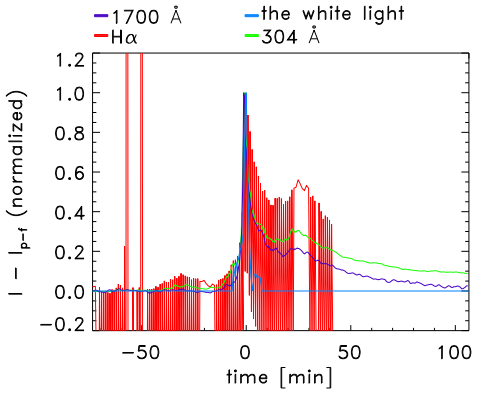

(a) Light curves for the white light, Hα, 1 700 Å and 304 Å.

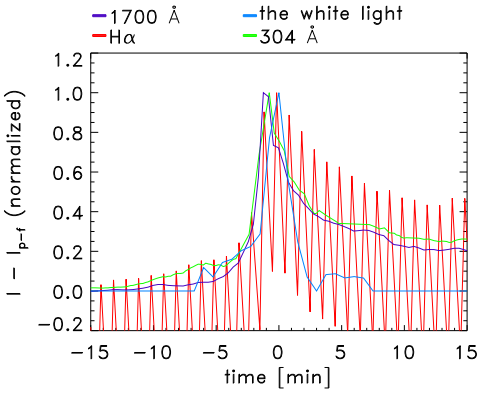

(b) Light curves for the white light, Hα, 1 700 Å and 304 Å zoomed in at the maximum of the WL emission.

Figure A.15: Light curves for the M7.9 solar flare on 2015 June 25 with the solar flare maximum at 08:16 UT.

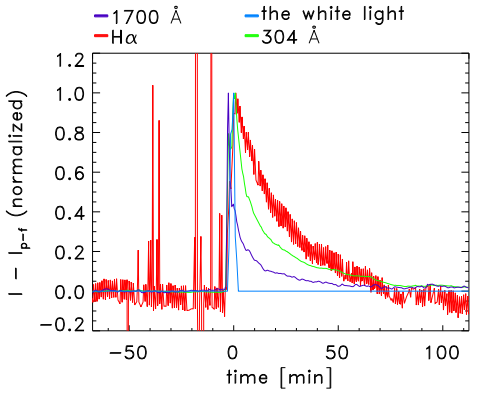

(a) Light curves for the white light, Hα, 1 700 Å and 304 Å.

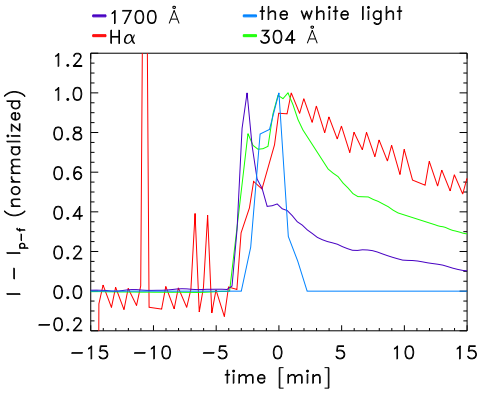

(b) Light curves for the white light, Hα, 1 700 Å and 304 Å zoomed in at the maximum of the WL emission.

Figure A.16: Light curves for the M7.2 solar flare on 2014 January 07 with the solar flare maximum at 10:13 UT.

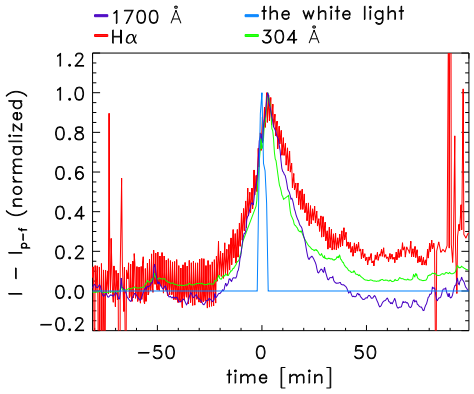

(a) Light curves for the white light, Hα, 1 700 Å and 304 Å.

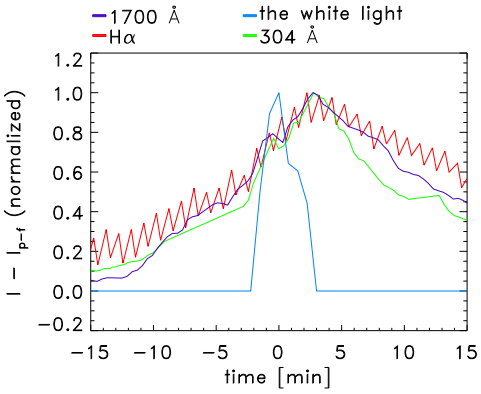

(b) Light curves for the white light, Hα, 1 700 Å and 304 Å zoomed in at the maximum of the WL emission.

Figure A.17: Light curves for the M7.1 solar flare on 2014 October 27 with the solar flare maximum at 00:34 UT.

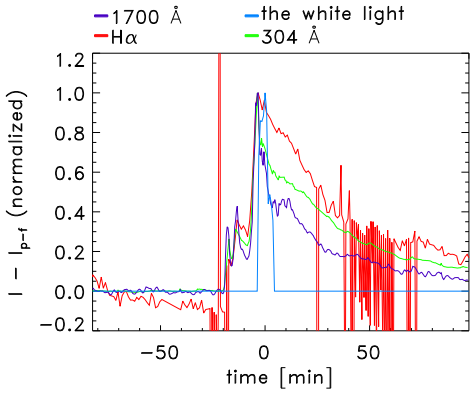

(a) Light curves for the white light, Hα, 1 700 Å and 304 Å.

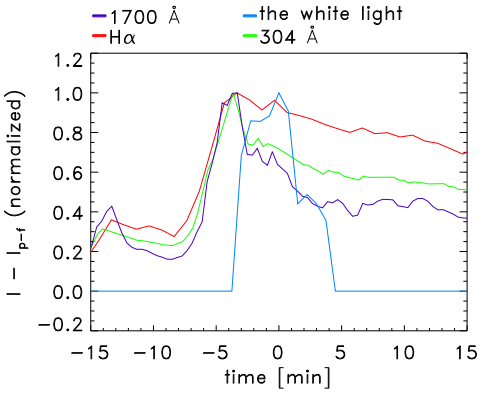

(b) Light curves for the white light, Hα, 1 700 Å and 304 Å zoomed in at the maximum of the WL emission.

Figure A.18: Light curves for the M6.3 solar flare on 2012 March 09 with the solar flare maximum at 03:53 UT.

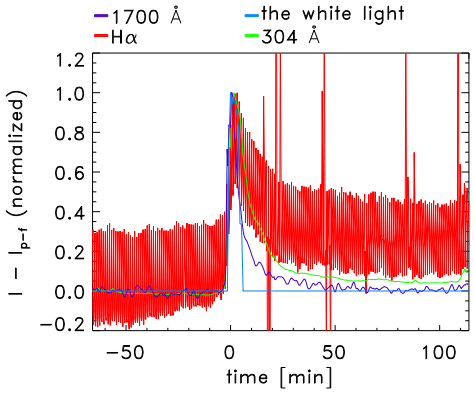

(a) Light curves for the white light, Hα, 1 700 Å and 304 Å.

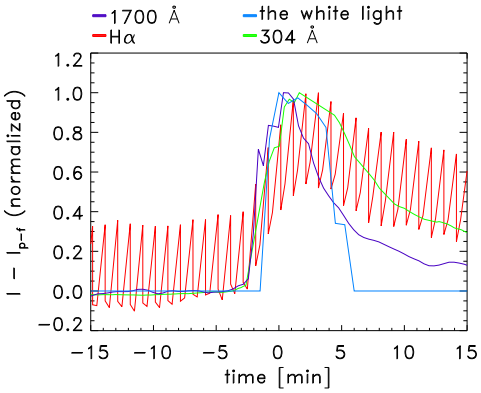

(b) Light curves for the white light, Hα, 1 700 Å and 304 Å zoomed in at the maximum of the WL emission.

Figure A.19: Light curves for the M6.3 solar flare on 2013 November 01 with the solar flare maximum at 19:53 UT.

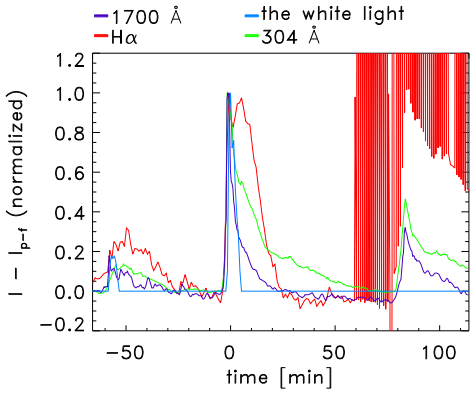

(a) Light curves for the white light, Hα, 1 700 Å and 304 Å.

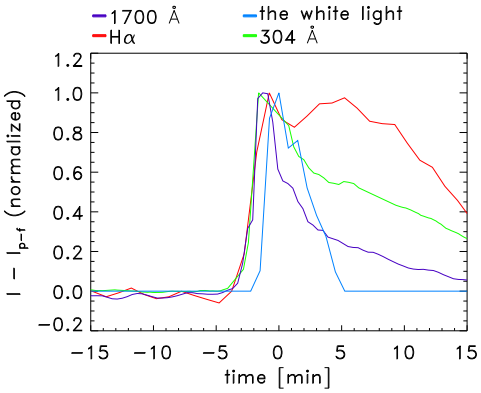

(b) Light curves for the white light, Hα, 1 700 Å and 304 Å zoomed in at the maximum of the WL emission.

Figure A.20: Light curves for the M6.2 solar flare on 2012 July 05 with the solar flare maximum at 11:44 UT.

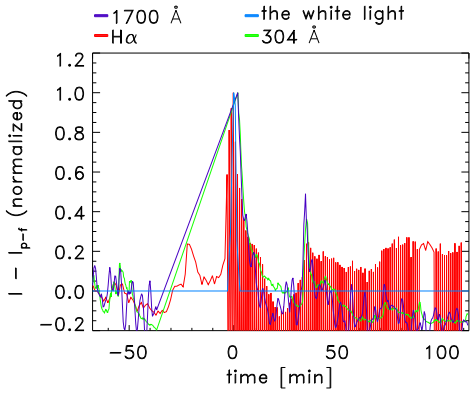

(a) Light curves for the white light, Hα, 1 700 Å and 304 Å.

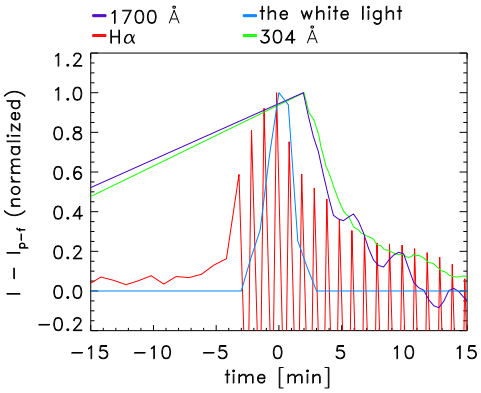

(b) Light curves for the white light, Hα, 1 700 Å and 304 Å zoomed in at the maximum of the WL emission.

Figure A.21: Light curves for the M5.6 solar flare on 2015 August 24 with the solar flare maximum at 07:33 UT.

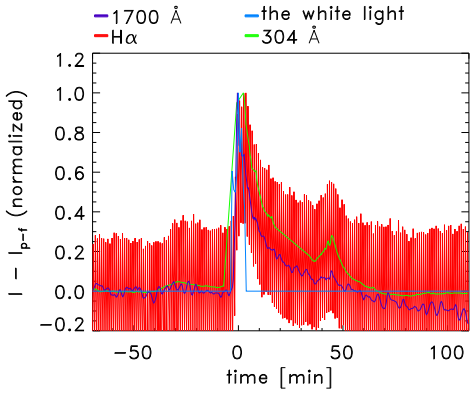

(a) Light curves for the white light, Hα, 1 700 Å and 304 Å.

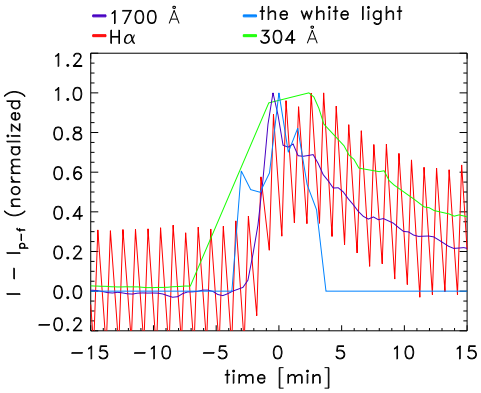

(b) Light curves for the white light, Hα, 1 700 Å and 304 Å zoomed in at the maximum of the WL emission.

Figure A.22: Light curves for the M5.3 solar flare on 2011 September 06 with the solar flare maximum at 01:50 UT.

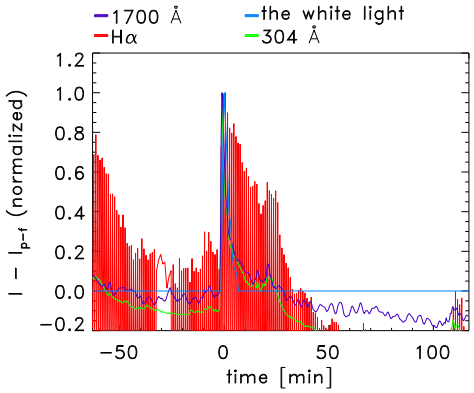

(a) Light curves for the white light, Hα, 1 700 Å and 304 Å.

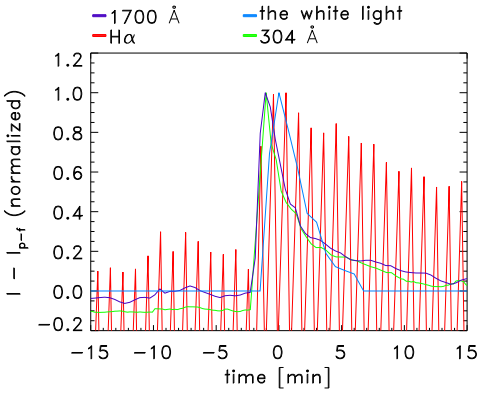

(b) Light curves for the white light, Hα, 1 700 Å and 304 Å zoomed in at the maximum of the WL emission.

Figure A.23: Light curves for the M5.2 solar flare on 2014 February 04 with the solar flare maximum at 04:00 UT.

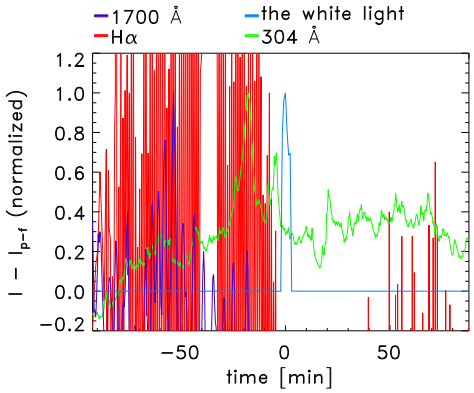

(a) Light curves for the white light, Hα, 1 700 Å and 304 Å.

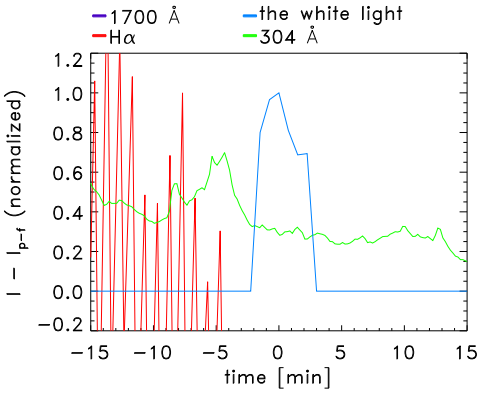

(b) Light curves for the white light, Hα, 1 700 Å and 304 Å zoomed in at the maximum of the WL emission.

Figure A.24: Light curves for the M5.1 solar flare on 2014 September 28 with the solar flare maximum at 02:58 UT.

A.2 Images at different wavelengths

In the following figures, there are images in the WL, in the Hα line, in the 304 Å, and 1 700 Å bands. Red points represent all detected WLF points. Blue points represent points where a WLF occurred at the time corresponding to the given image. For some flares, the Hα image is black because there are data missing during the detected WLF.

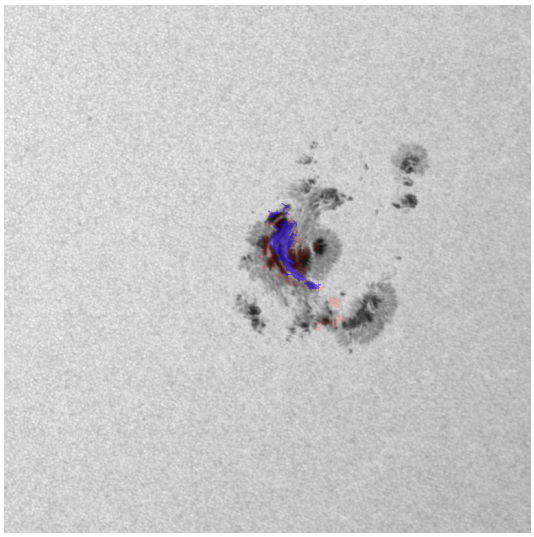

(a) The white light

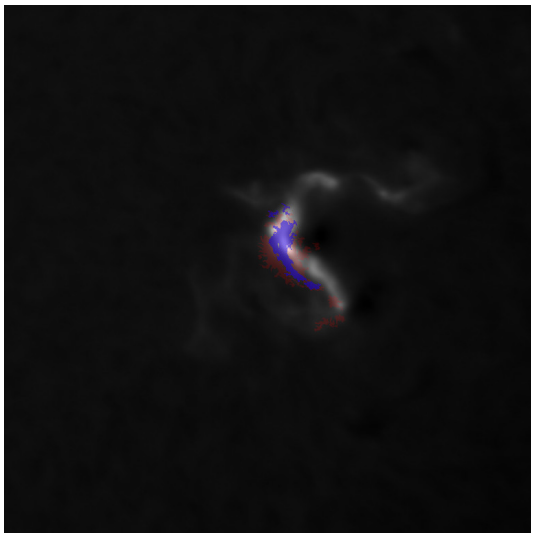

(b) The Hα line

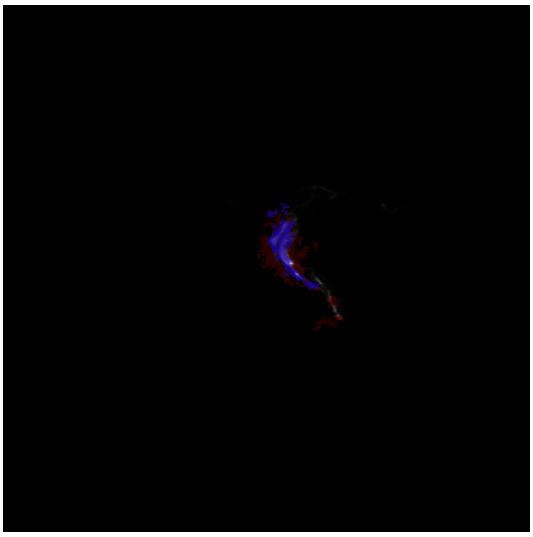

(c) 304 Å

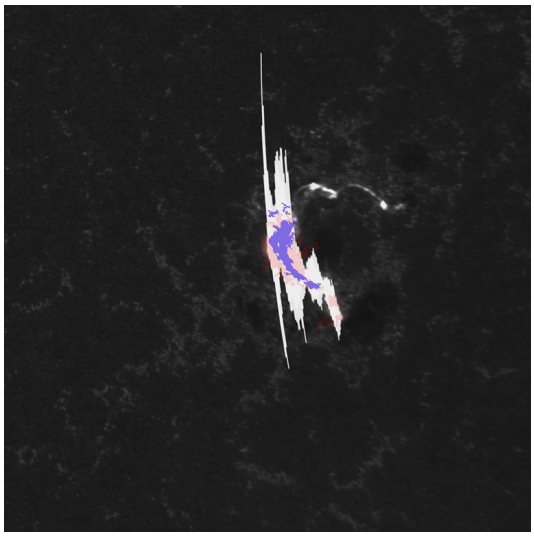

(d) 1 700 Å

Figure A.25: Images of the Sun in different wavelength channels for the X9.3 solar flare on 2017 September 06 with the solar flare maximum at 12:02 UT. Red points are points where a WLF was detected an at any time during the whole data cube. Blue points represent points where a WLF was detected at the time that correspond to this image.

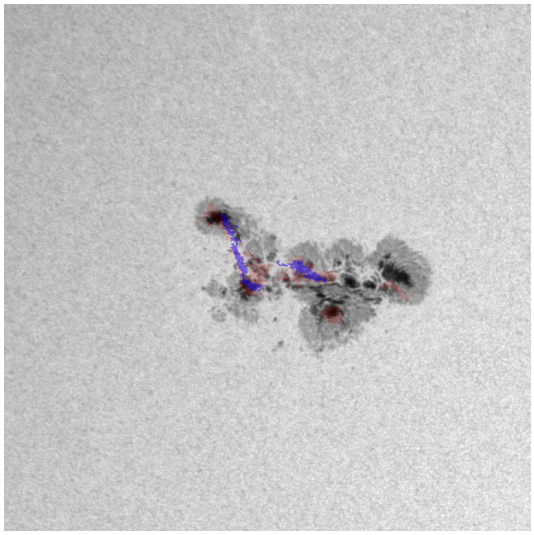

(a) The white light

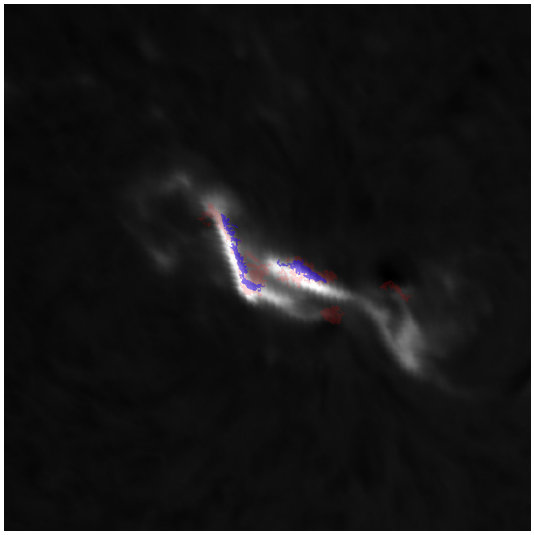

(b) The Hα line

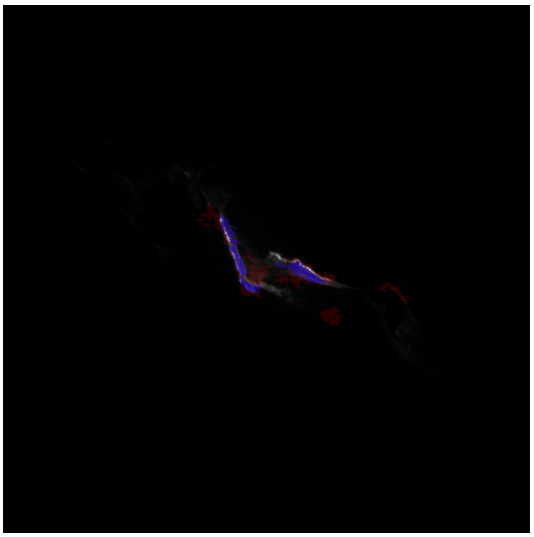

(c) 304 Å

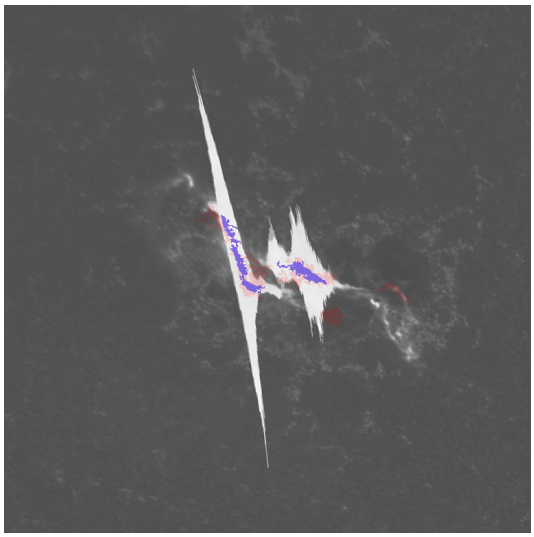

(d) 1 700 Å

Figure A.26: The same as in Figure A.25 but for the X5.4 solar flare on 2012 March 07 with the solar flare maximum at 00:24 UT.

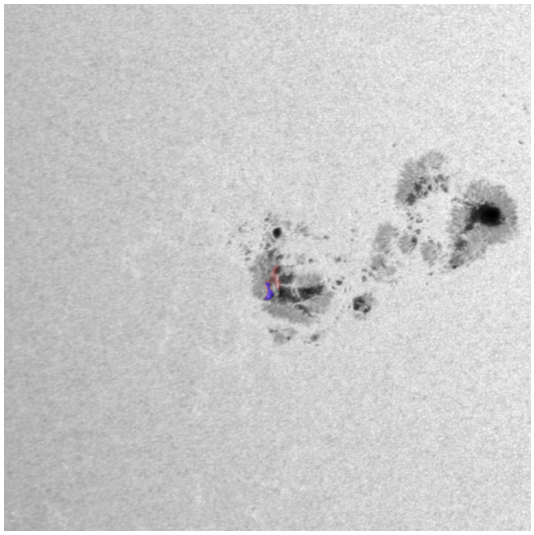

(a) The white light

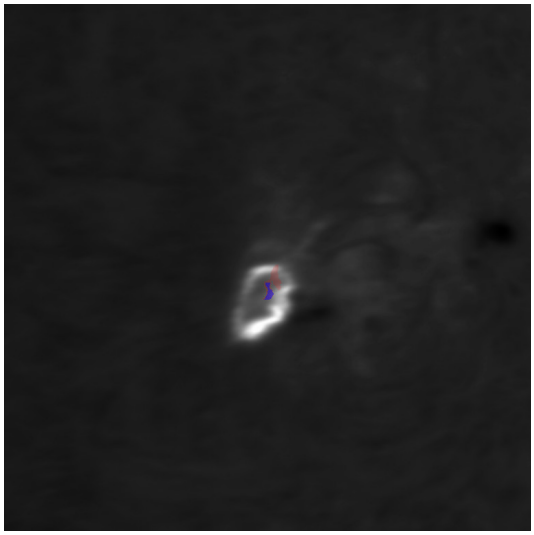

(b) The Hα line

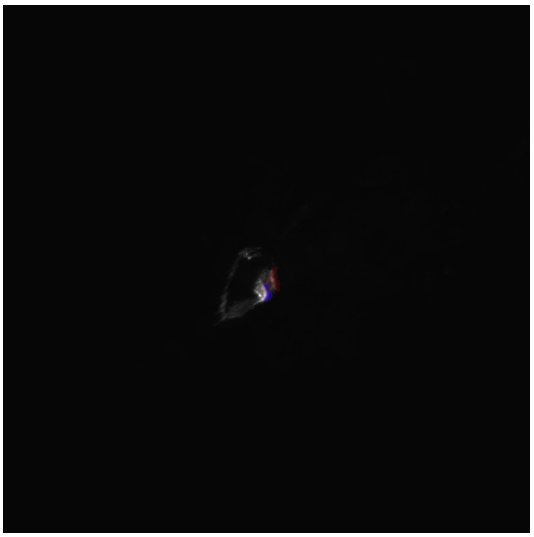

(c) 304 Å

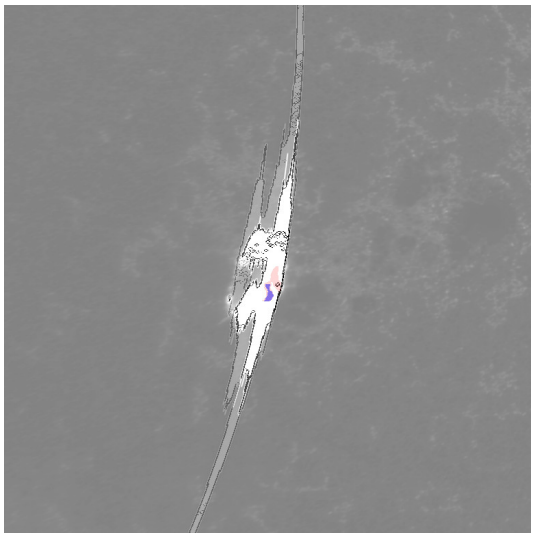

(d) 1 700 Å

Figure A.27: The same as in Figure A.25 but for the X3.3 solar flare on 2013 November 05 with the solar flare maximum at 22:12 UT.

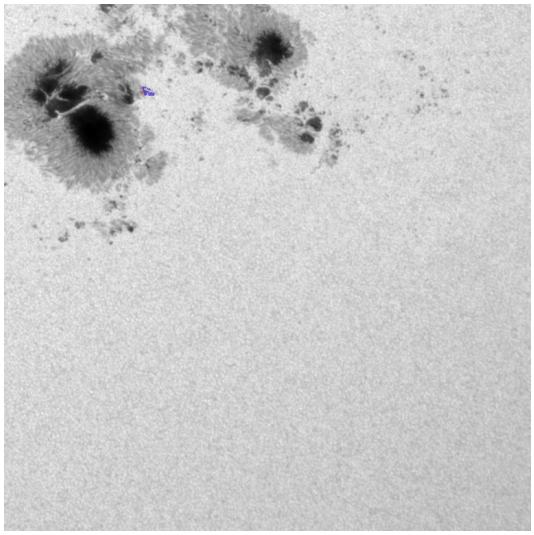

(a) The white light

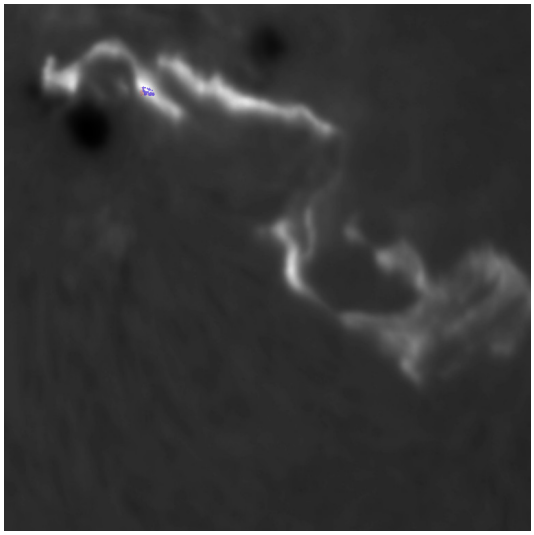

(b) The Hα line

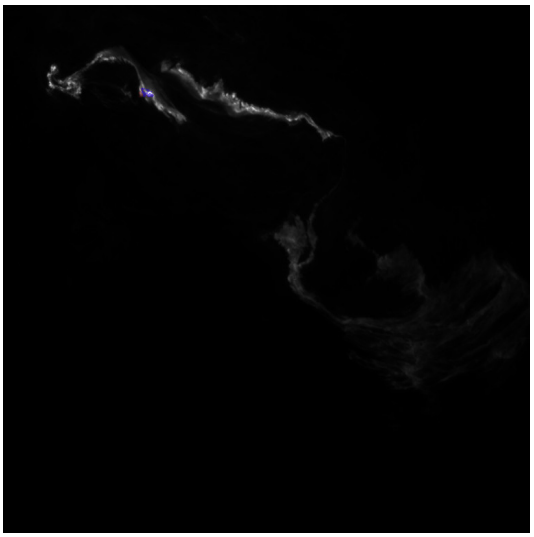

(c) 304 Å

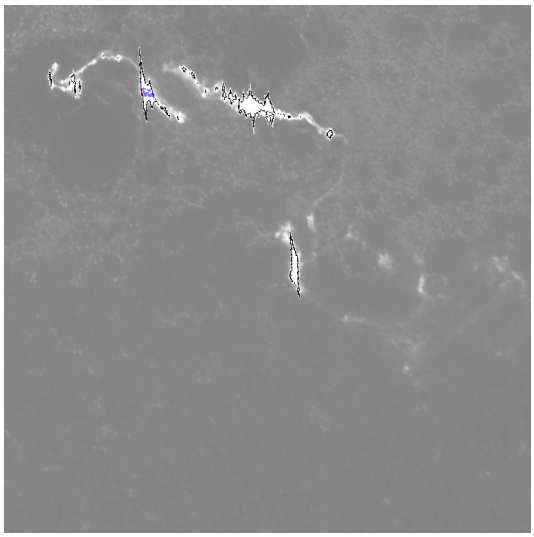

(d) 1 700 Å

Figure A.28: The same as in Figure A.25 but for the X3.1 solar flare on 2014 October 24 with the solar flare maximum at 21:41 UT.

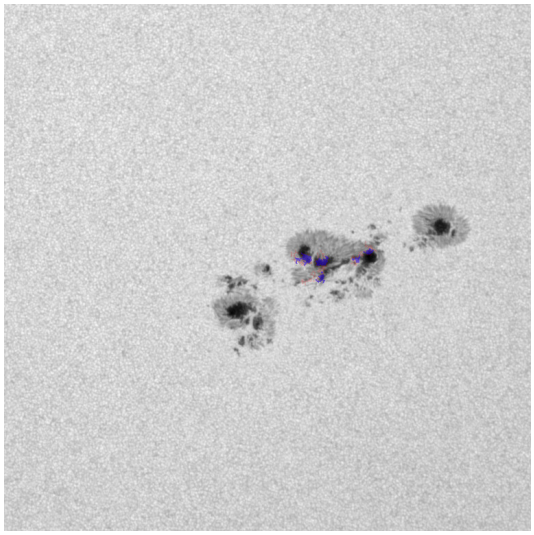

(a) The white light

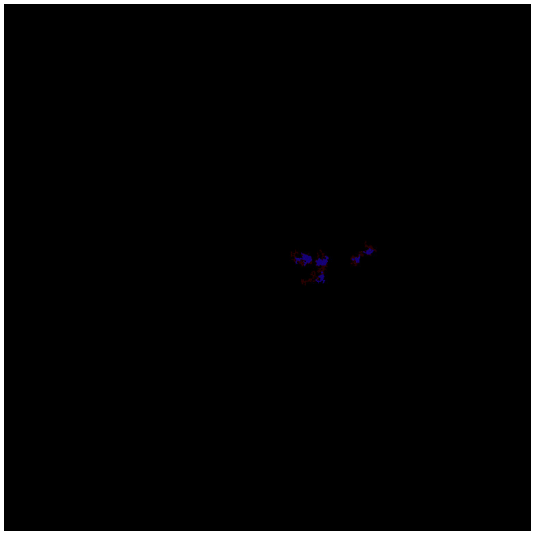

(b) The Hα line

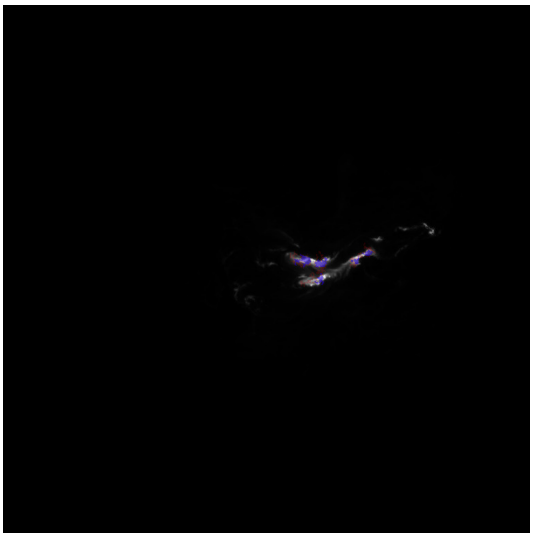

(c) 304 Å

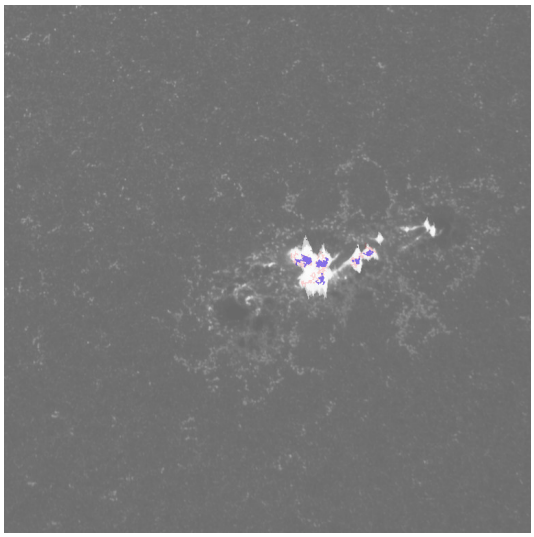

(d) 1 700 Å

Figure A.29: The same as in Figure A.25 but for the X2.2 solar flare on 2011 February 15 with the solar flare maximum at 01:56 UT.

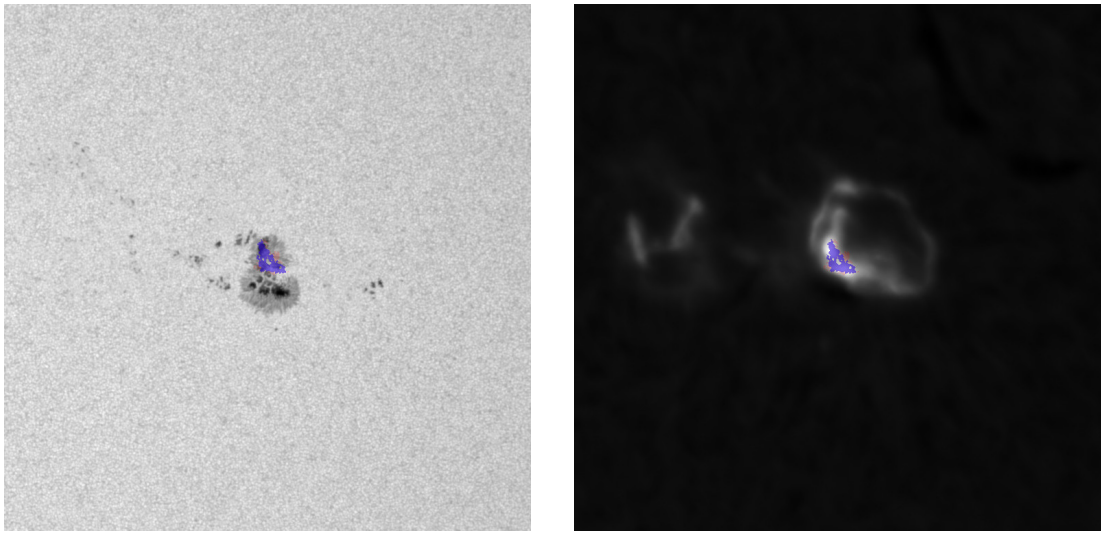

(a) The white light

(b) The Hα line

(c) 304 Å

(d) 1 700 Å

Figure A.30: The same as in Figure A.25 but for the X2.1 solar flare on 2011 September 06 with the solar flare maximum at 22:20 UT.

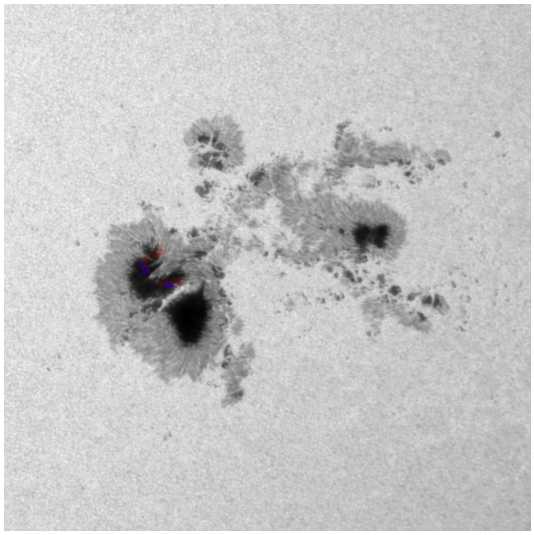

(a) The white light

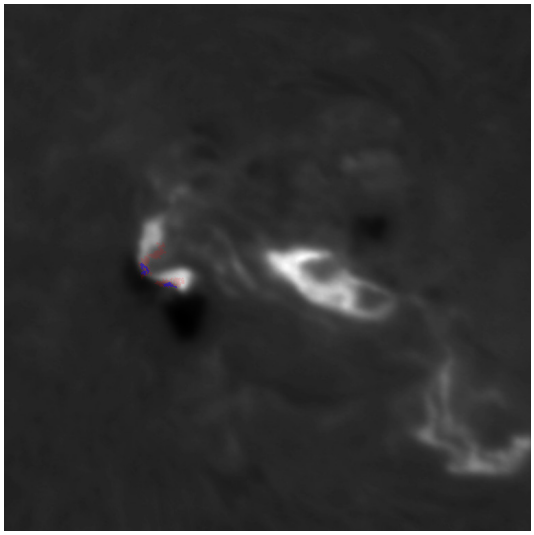

(b) The Hα line

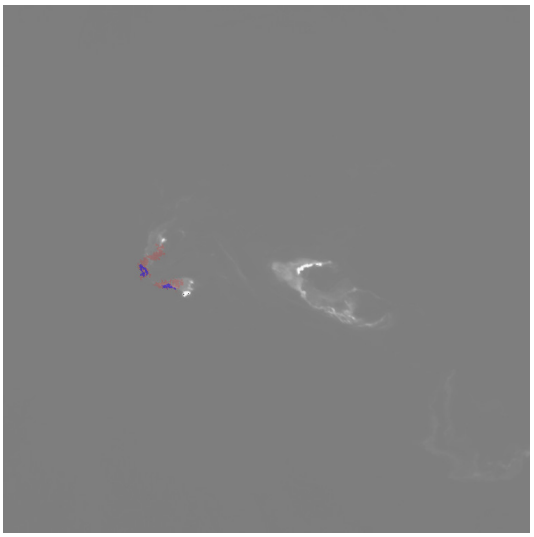

(c) 304 Å

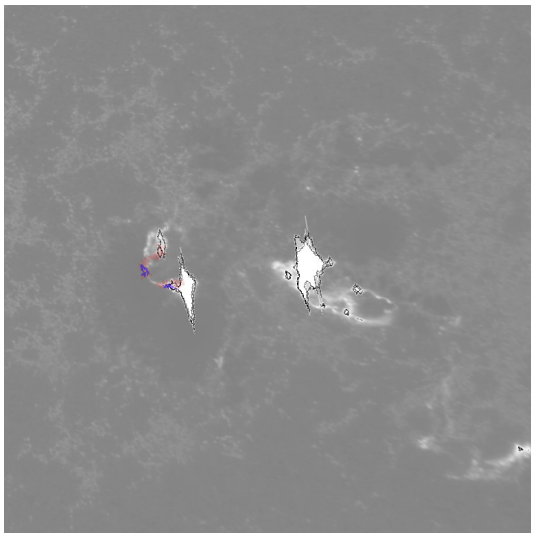

(d) 1 700 Å

Figure A.31: The same as in Figure A.25 but for the X2.0 solar flare on 2014 October 26 with the solar flare maximum at 10:56 UT.

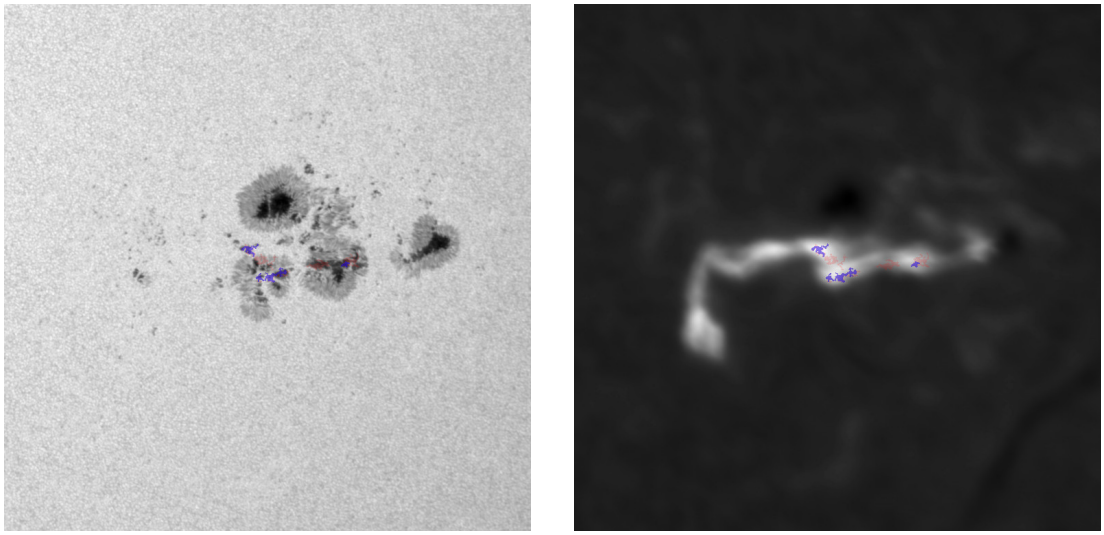

(a) The white light

(b) The Hα line

(c) 304 Å

(d) 1 700 Å

Figure A.32: The same as in Figure A.25 but for the X1.8 solar flare on 2014 December 20 with the solar flare maximum at 00:28 UT.

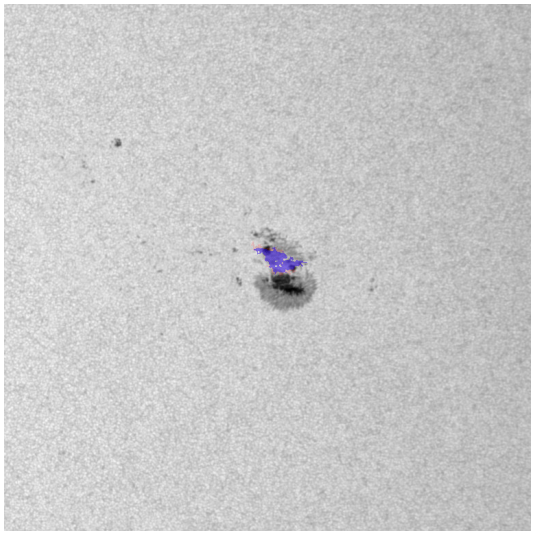

(a) The white light

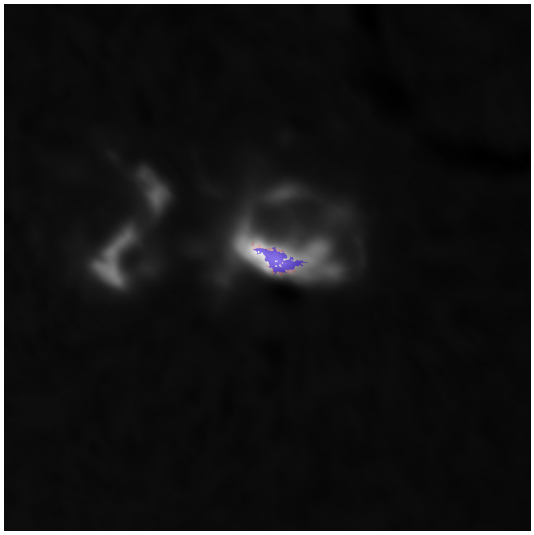

(b) The Hα line

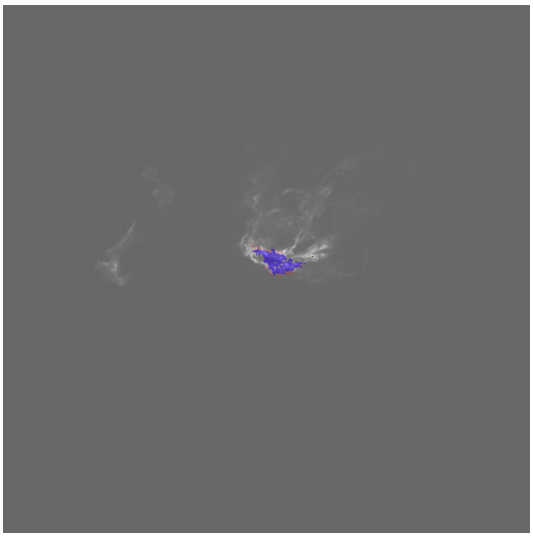

(c) 304 Å

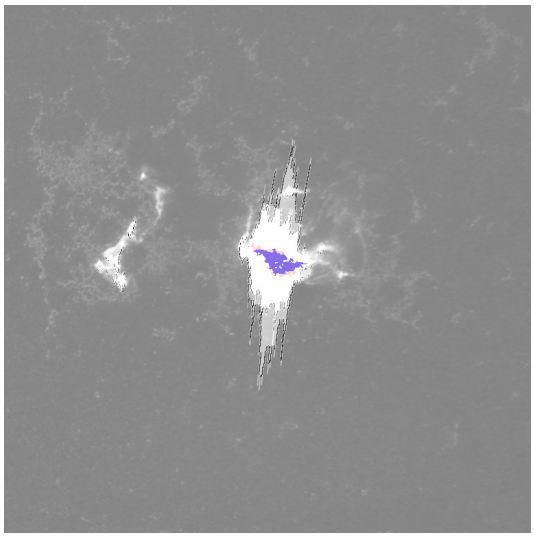

(d) 1 700 Å

Figure A.33: The same as in Figure A.25 but for the X1.8 solar flare on 2011 September 07 with the solar flare maximum at 22:38 UT.

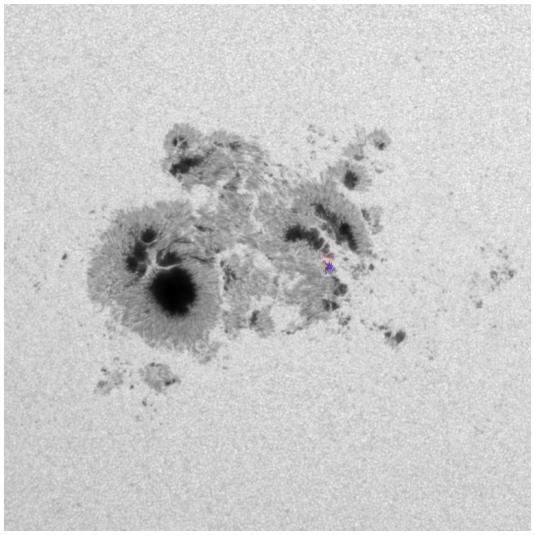

(a) The white light

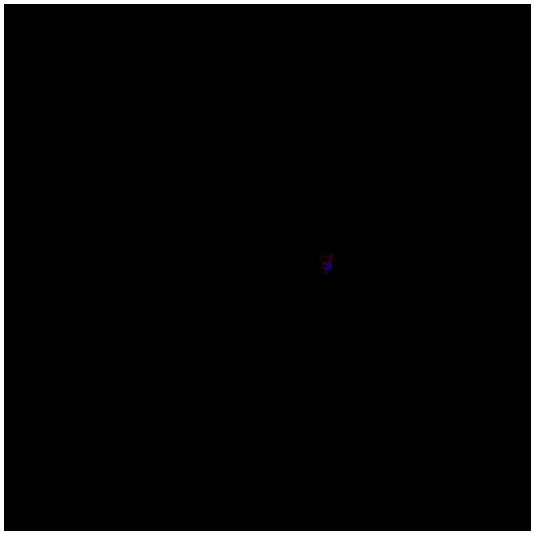

(b) The Hα line

(c) 304 Å

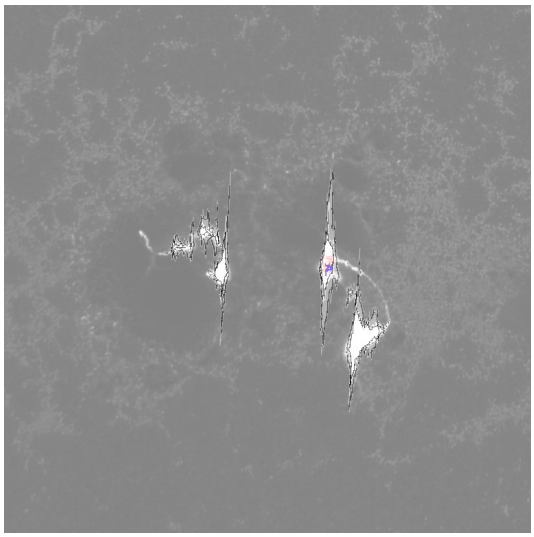

(d) 1 700 Å

Figure A.34: The same as in Figure A.25 but for the X1.6 solar flare on 2014 October 22 with the solar flare maximum at 14:28 UT.

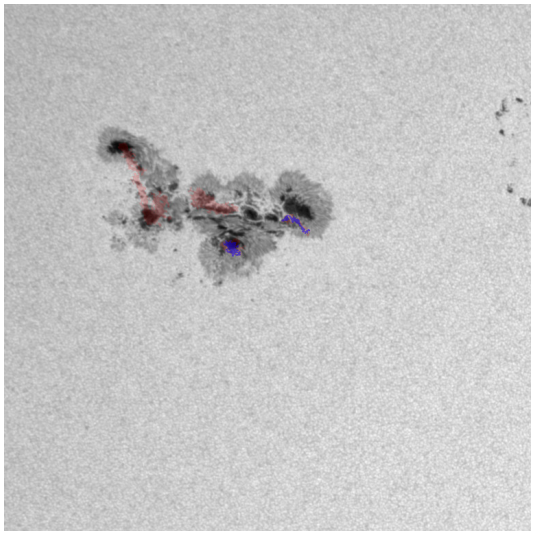

(a) The white light

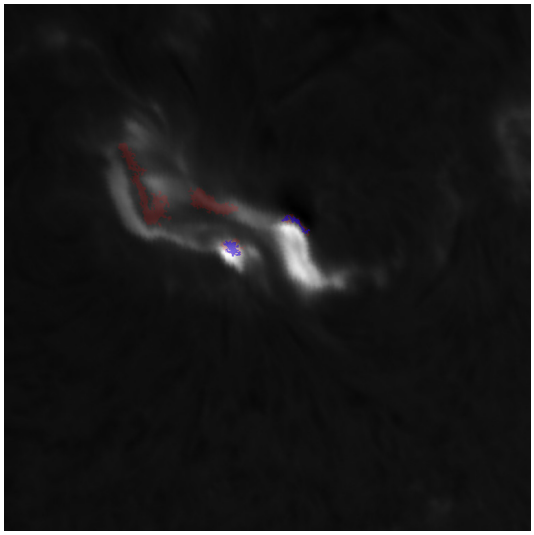

(b) The Hα line

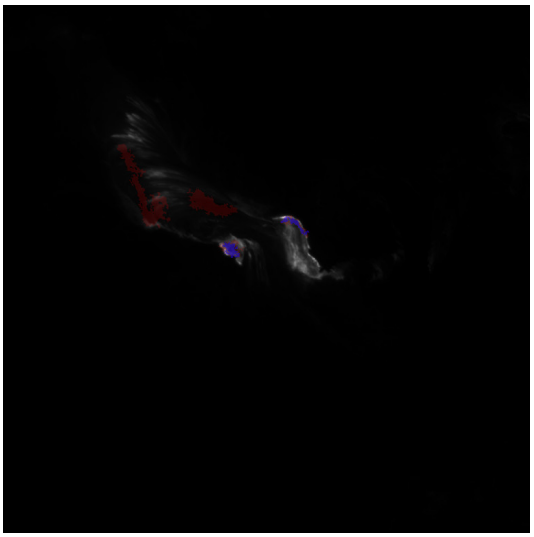

(c) 304 Å

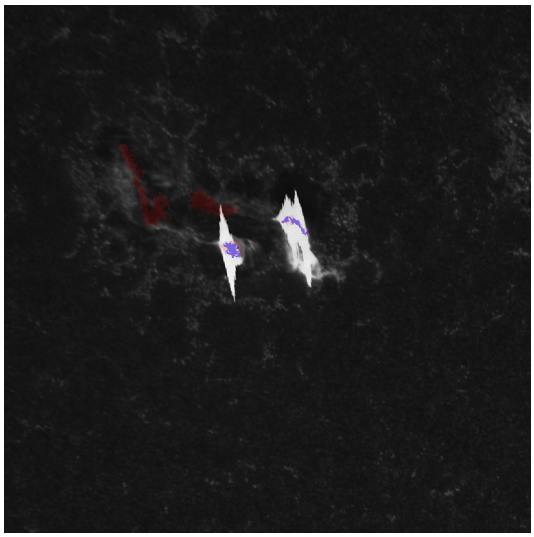

(d) 1 700 Å

Figure A.35: The same as in Figure A.25 but for the X1.3 solar flare on 2012 March 07 with the solar flare maximum at 01:14 UT.

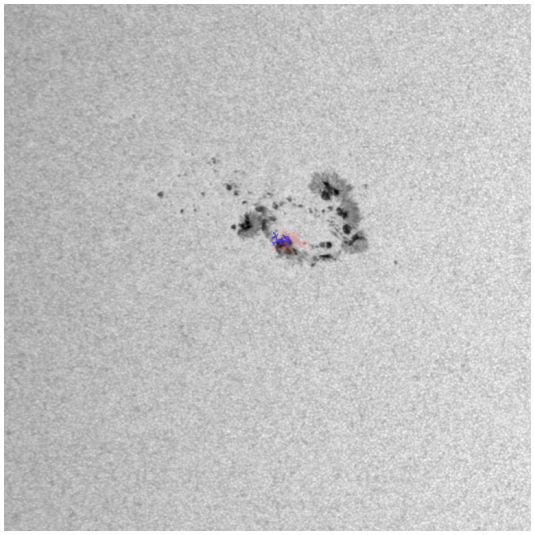

(a) The white light

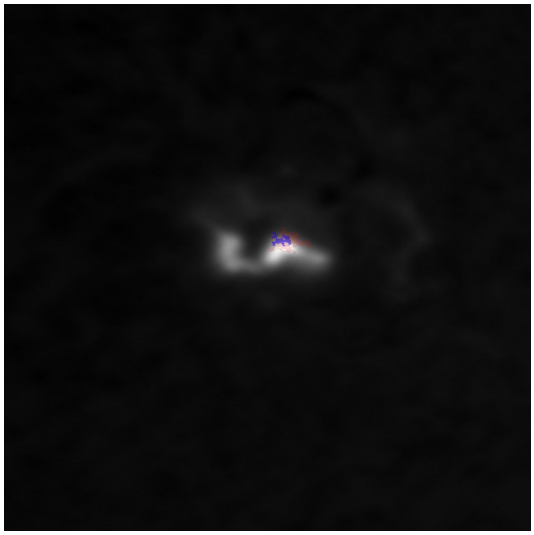

(b) The Hα line

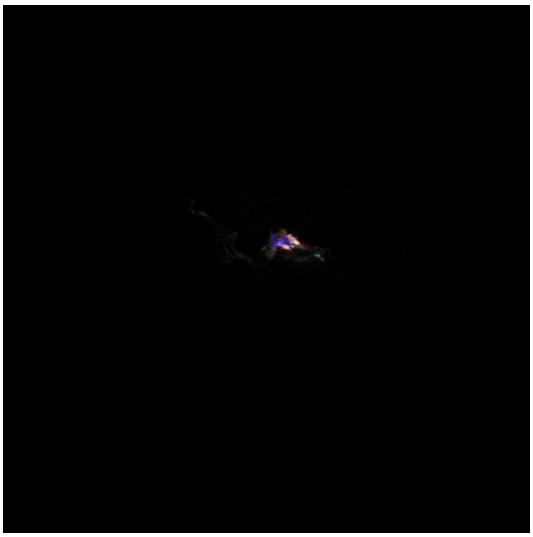

(c) 304 Å

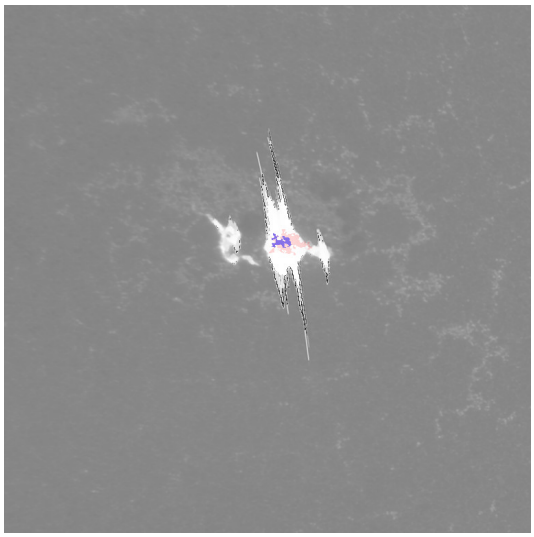

(d) 1 700 Å

Figure A.36: The same as in Figure A.25 but for the M9.3 solar flare on 2011 July 30 with the solar flare maximum at 02:09 UT.

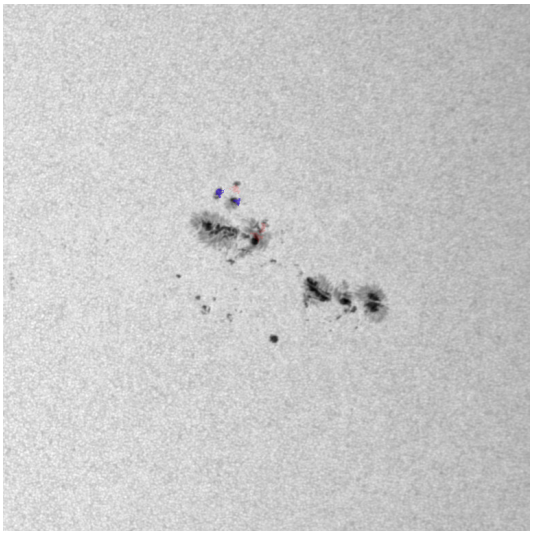

(a) The white light

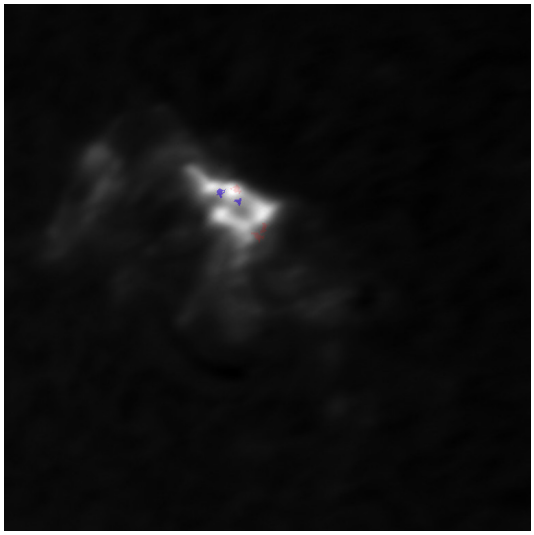

(b) The Hα line

(c) 304 Å

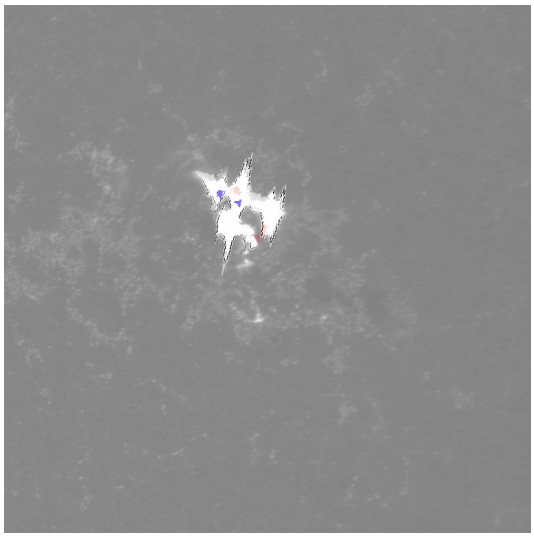

(d) 1 700 Å

Figure A.37: The same as in Figure A.25 but for the M9.3 solar flare on 2011 August 04 with the solar flare maximum at 03:57 UT.

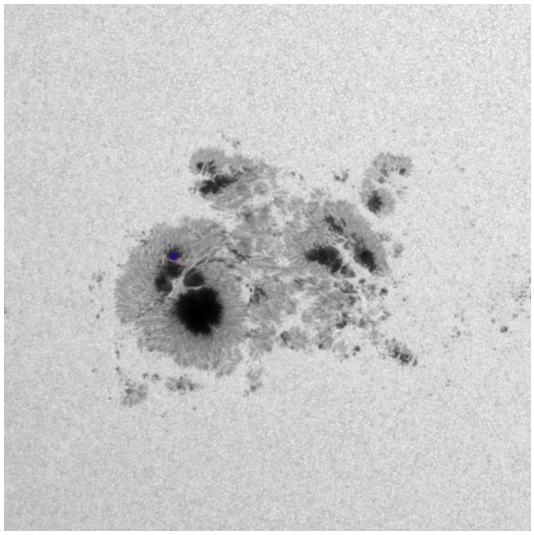

(a) The white light

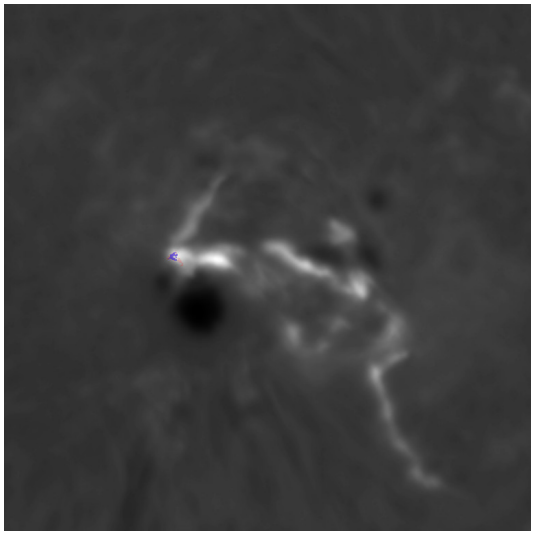

(b) The Hα line

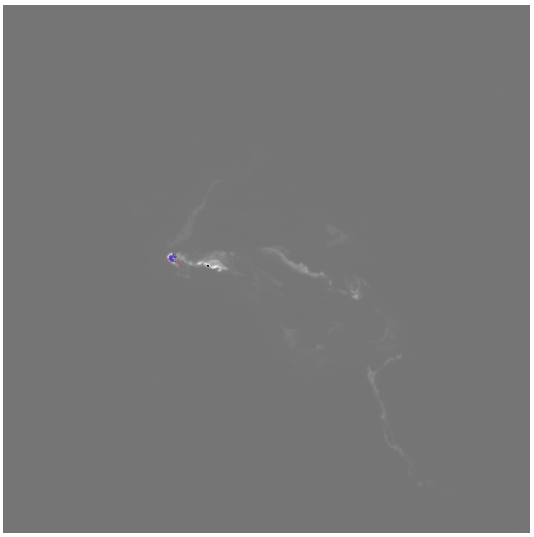

(c) 304 Å

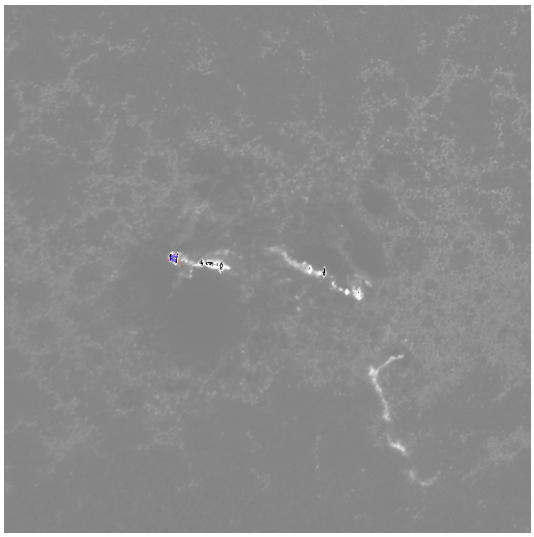

(d) 1 700 Å

Figure A.38: The same as in Figure A.25 but for the M8.7 solar flare on 2014 October 22 with the solar flare maximum at 01:59 UT.

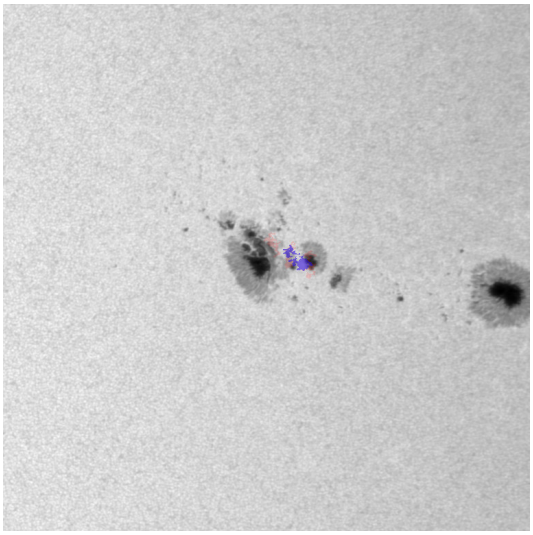

(a) The white light

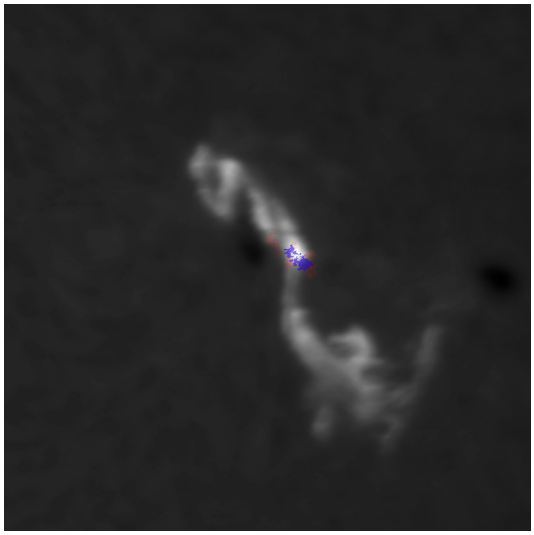

(b) The Hα line

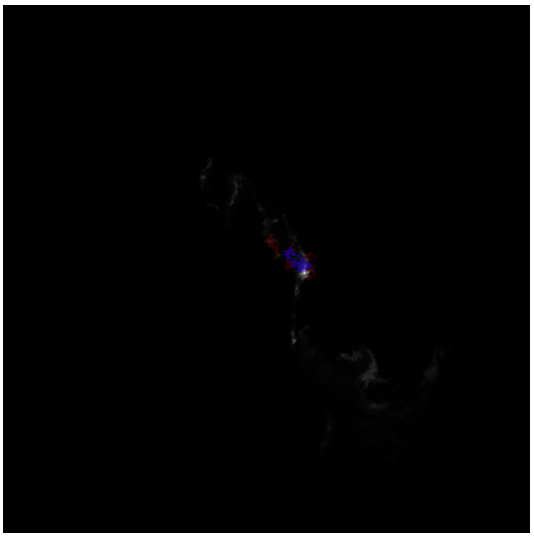

(c) 304 Å

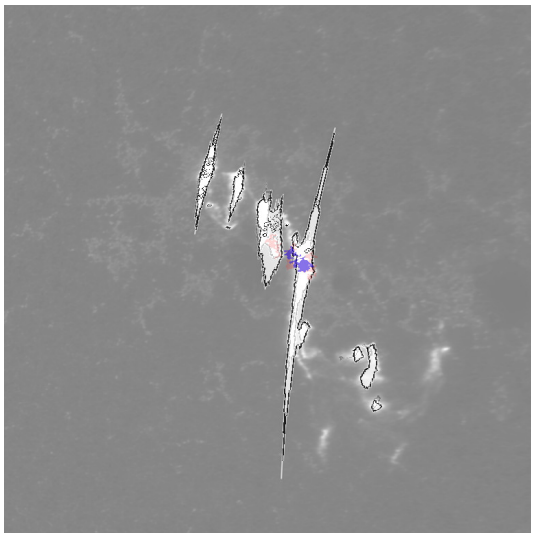

(d) 1 700 Å

Figure A.39: The same as in Figure A.25 but for the M7.9 solar flare on 2015 June 25 with the solar flare maximum at 08:16 UT.

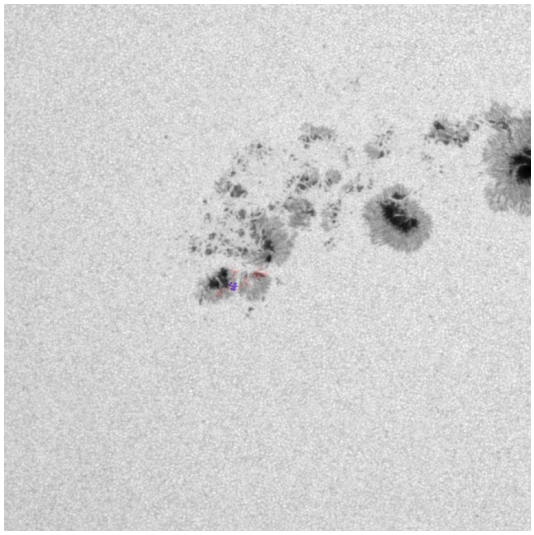

(a) The white light

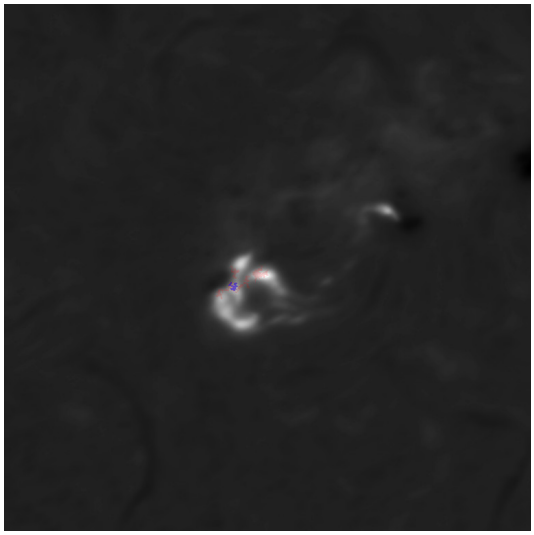

(b) The Hα line

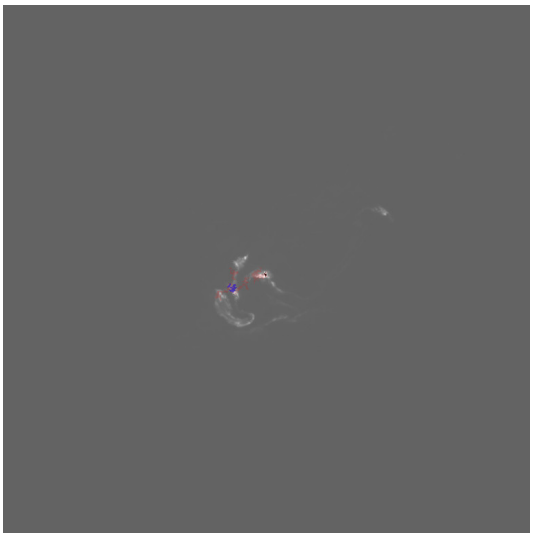

(c) 304 Å

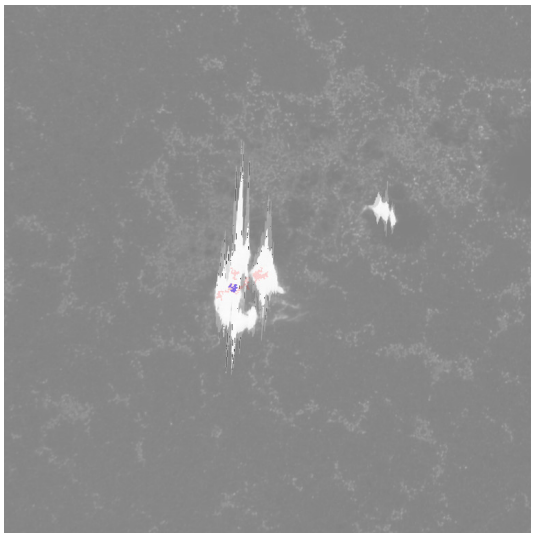

(d) 1 700 Å

Figure A.40: The same as in Figure A.25 but for the M7.2 solar flare on 2014 January 07 with the solar flare maximum at 10:13 UT.

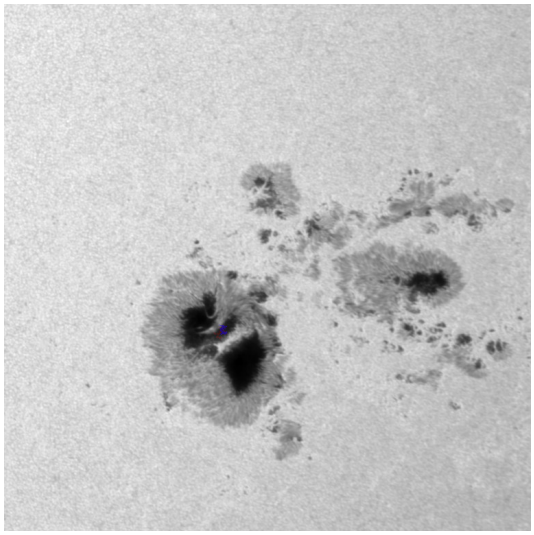

(a) The white light

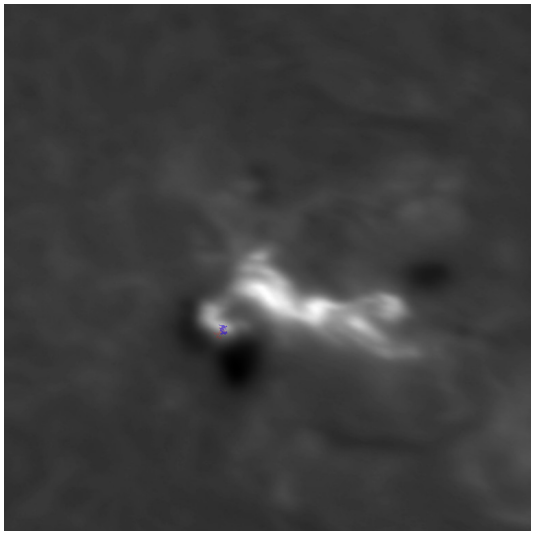

(b) The Hα line

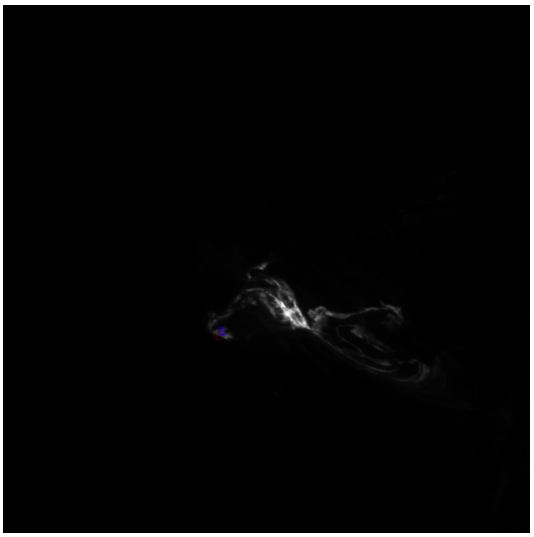

(c) 304 Å

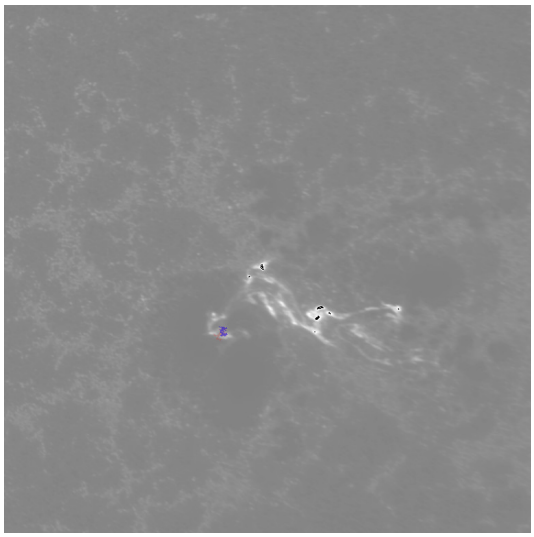

(d) 1 700 Å

Figure A.41: The same as in Figure A.25 but for the M7.1 solar flare on 2014 October 27 with the solar flare maximum at 00:34 UT.

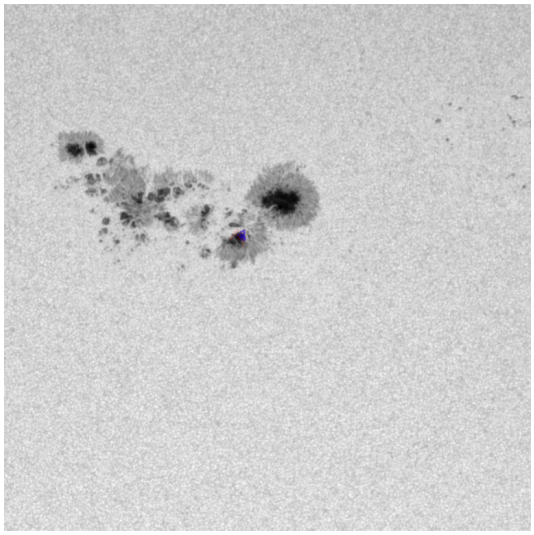

(a) The white light

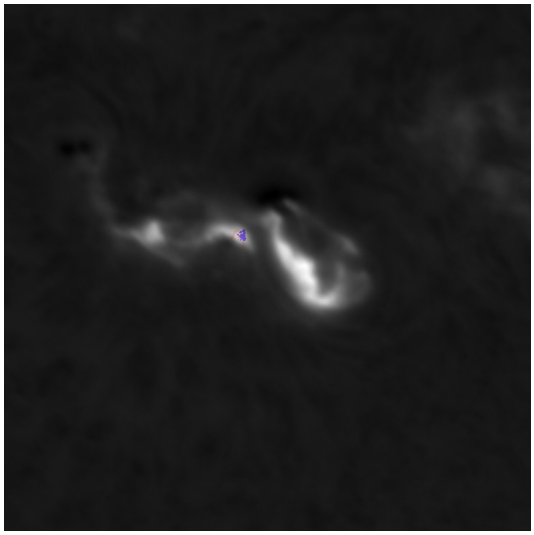

(b) The Hα line

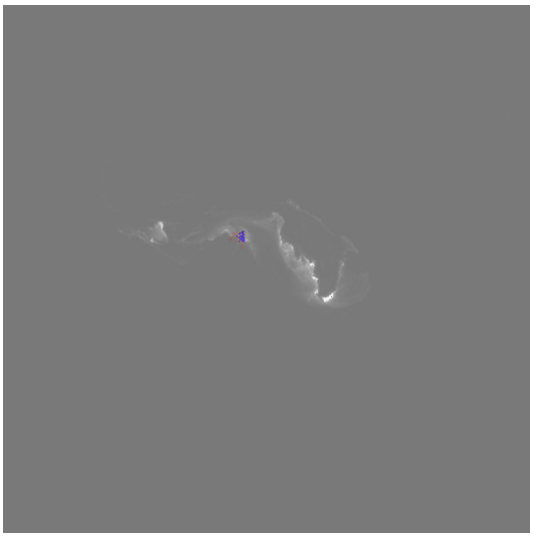

(c) 304 Å

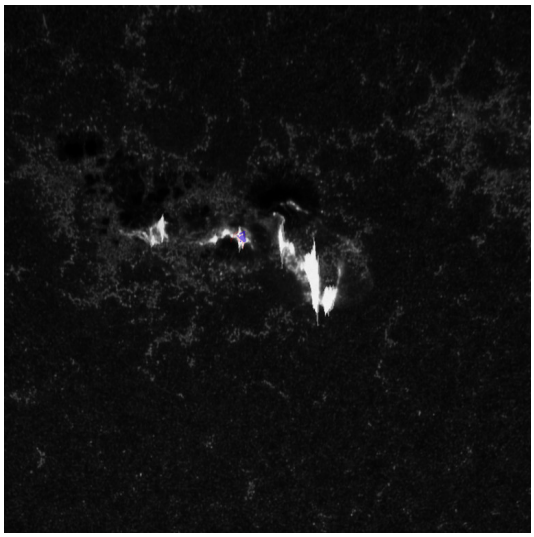

(d) 1 700 Å

Figure A.42: The same as in Figure A.25 but for the M6.3 solar flare on 2012 March 09 with the solar flare maximum at 03:53 UT.

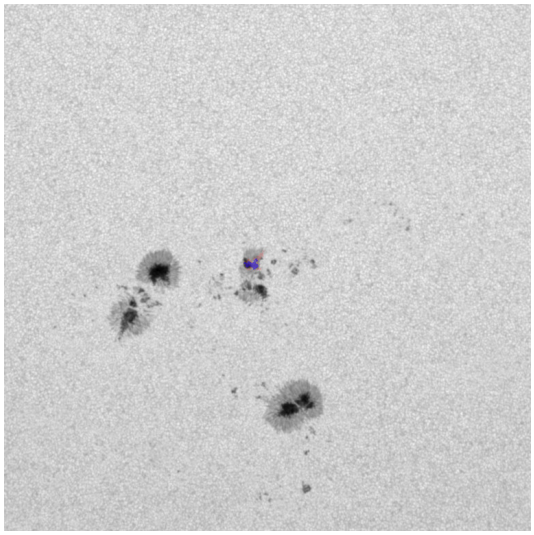

(a) The white light

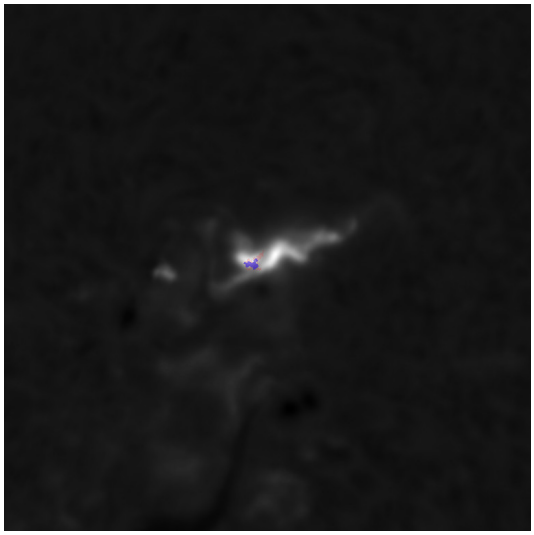

(b) The Hα line

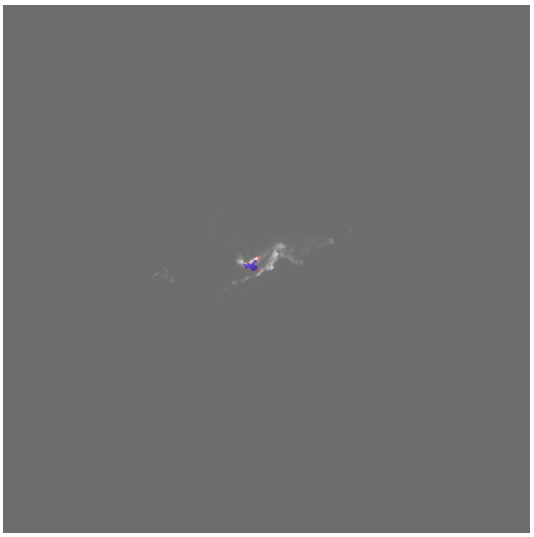

(c) 304 Å

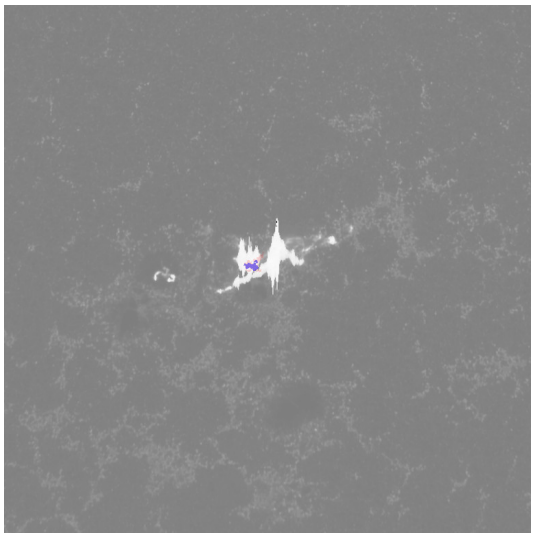

(d) 1 700 Å

Figure A.43: The same as in Figure A.25 but for the M6.3 solar flare on 2013 November 01 with the solar flare maximum at 19:53 UT.

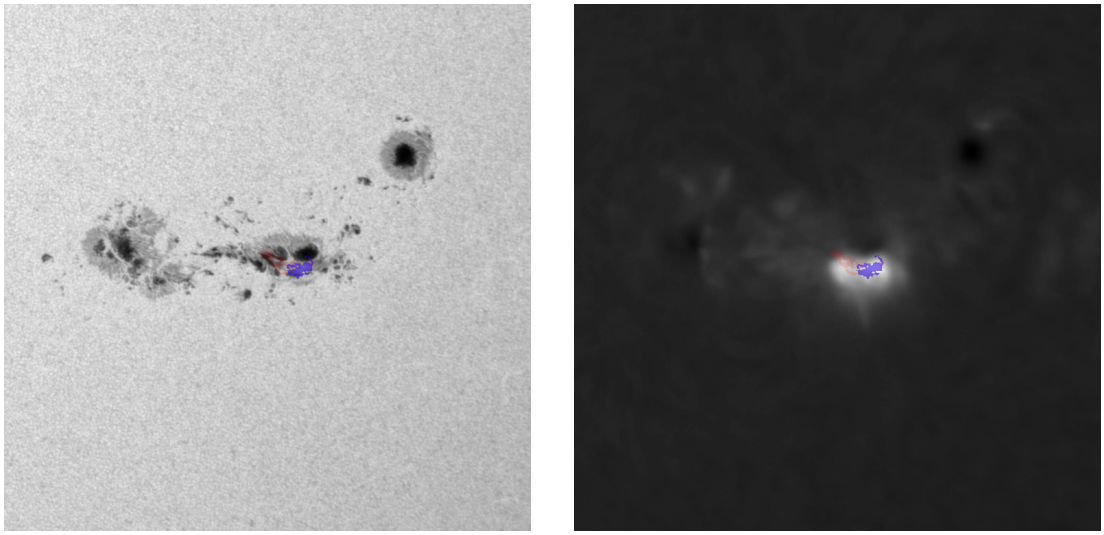

(a) The white light

(b) The Hα line

(c) 304 Å

(d) 1 700 Å

Figure A.44: The same as in Figure A.25 but for the M6.2 solar flare on 2012 July 05 with the solar flare maximum at 11:44 UT.

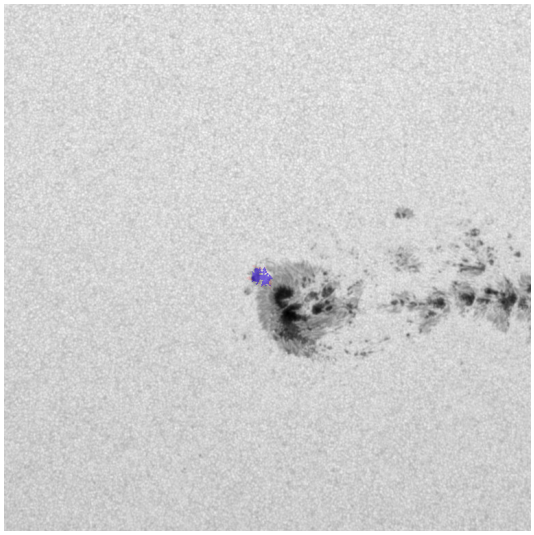

(a) The white light

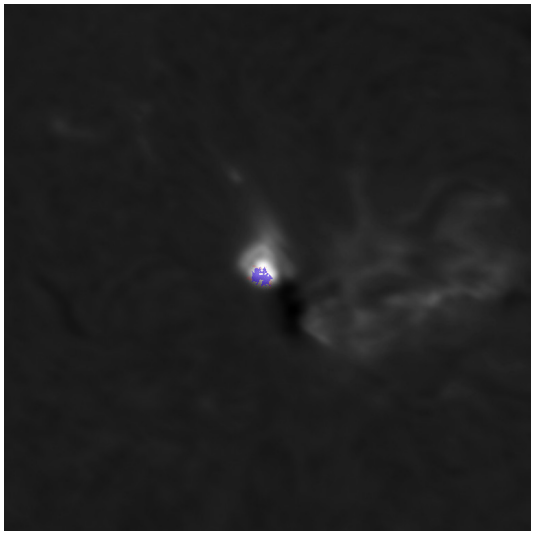

(b) The Hα line

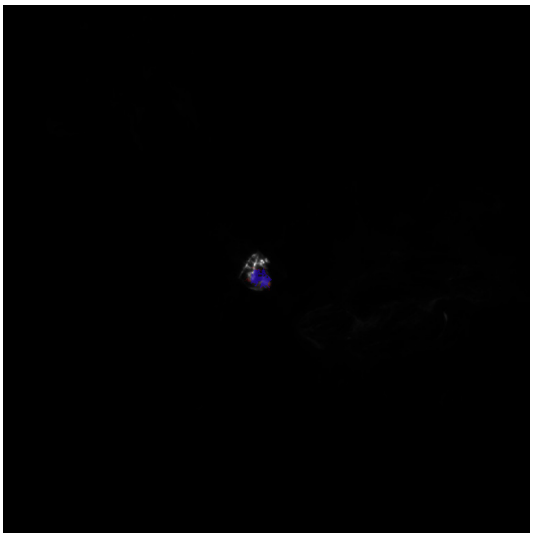

(c) 304 Å

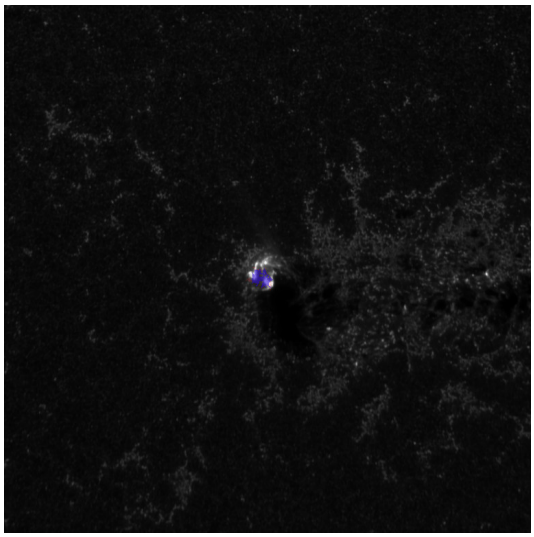

(d) 1 700 Å

Figure A.45: The same as in Figure A.25 but for the M5.6 solar flare on 2015 August 24 with the solar flare maximum at 07:33 UT.

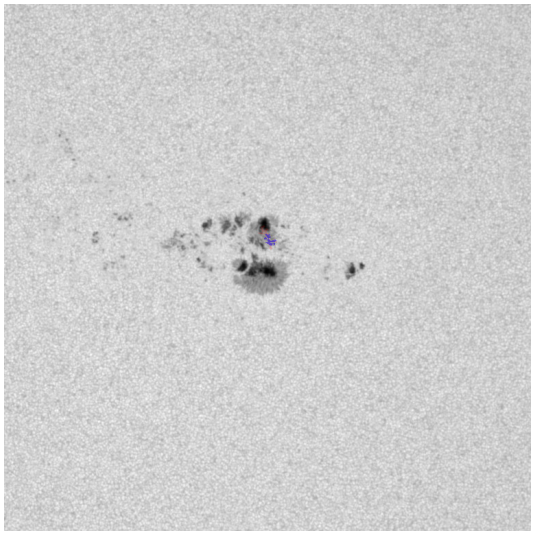

(a) The white light

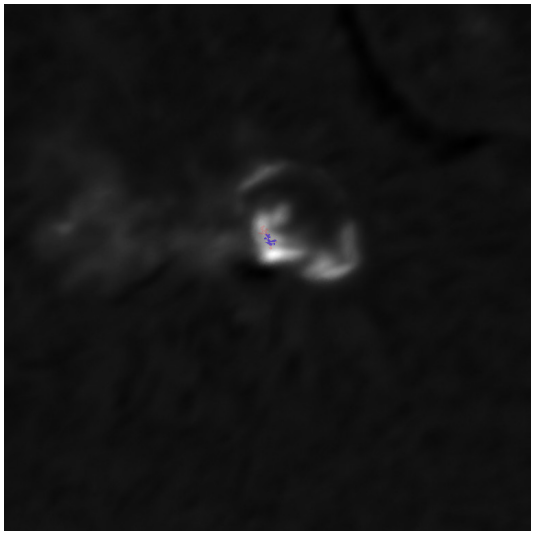

(b) The Hα line

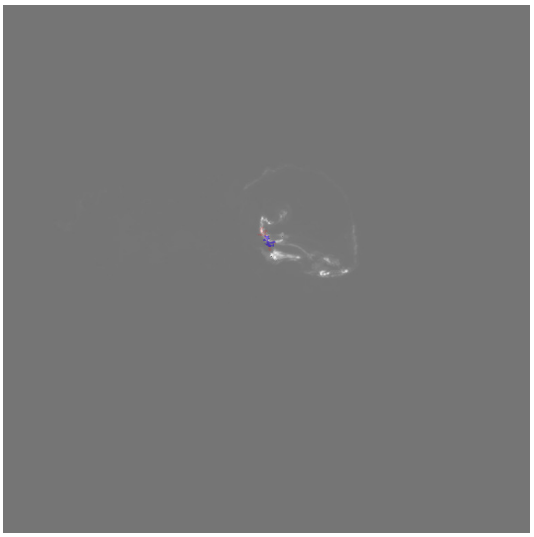

(c) 304 Å

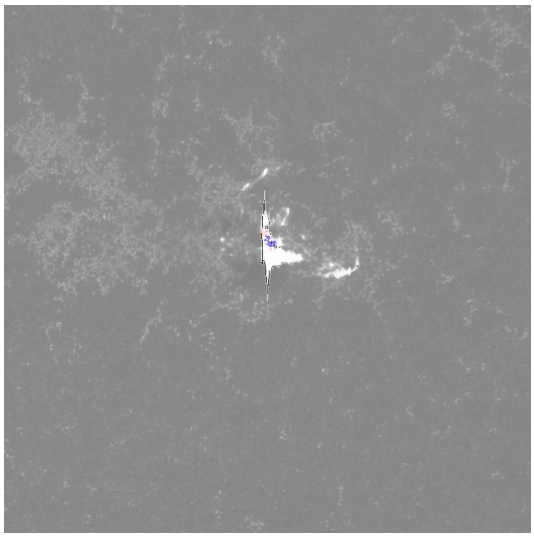

(d) 1 700 Å

Figure A.46: The same as in Figure A.25 but for the M5.3 solar flare on 2011 September 06 with the solar flare maximum at 01:50 UT.

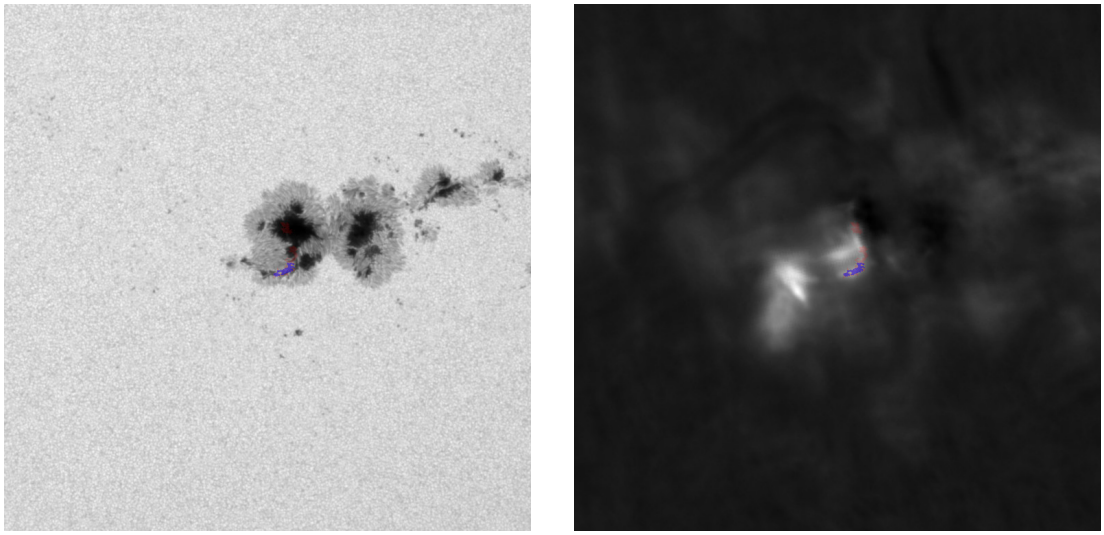

(a) The white light

(b) The Hα line

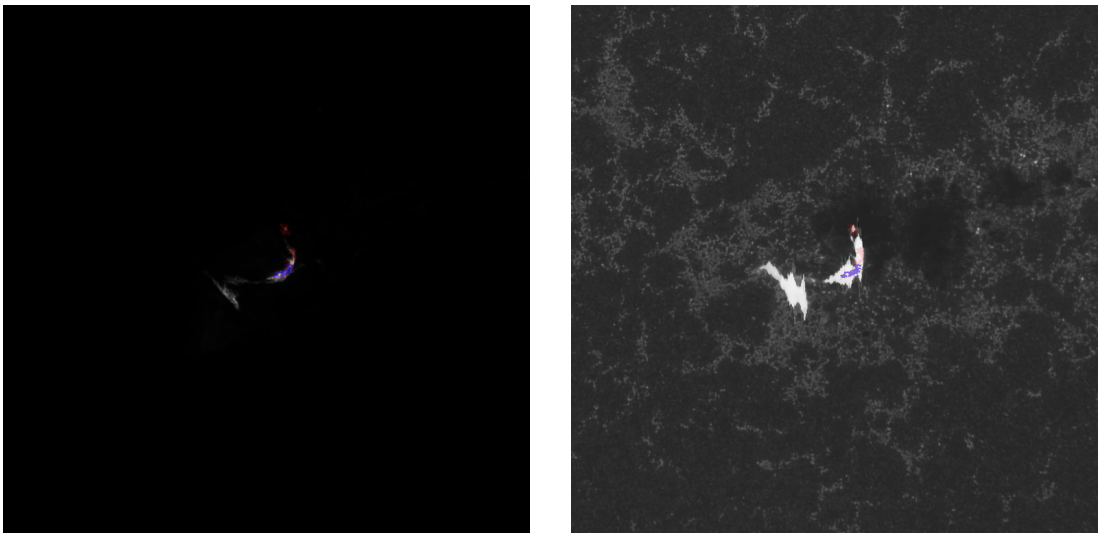

(c) 304 Å

(d) 1 700 Å

Figure A.47: The same as in Figure A.25 but for the M5.2 solar flare on 2014 February 04 with the solar flare maximum at 04:00 UT.

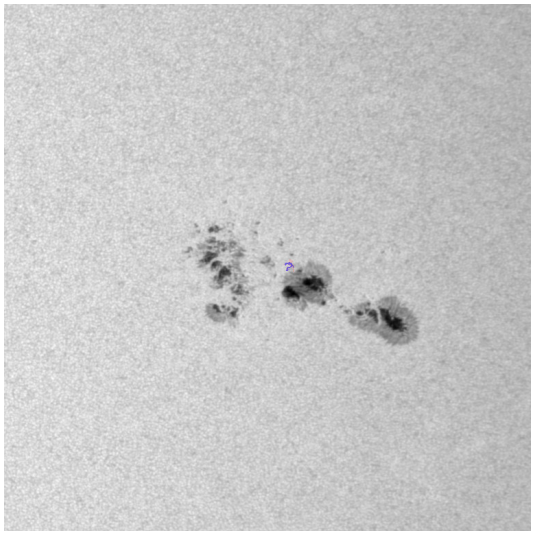

(a) The white light

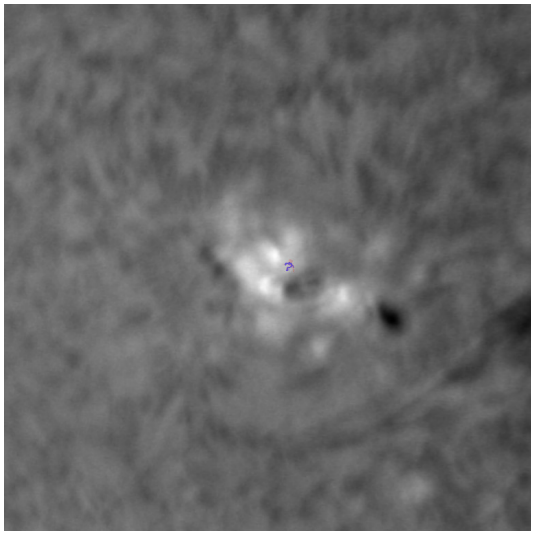

(b) The Hα line

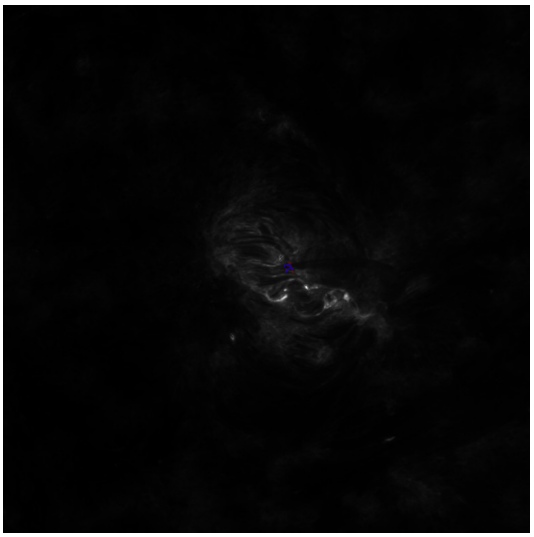

(c) 304 Å

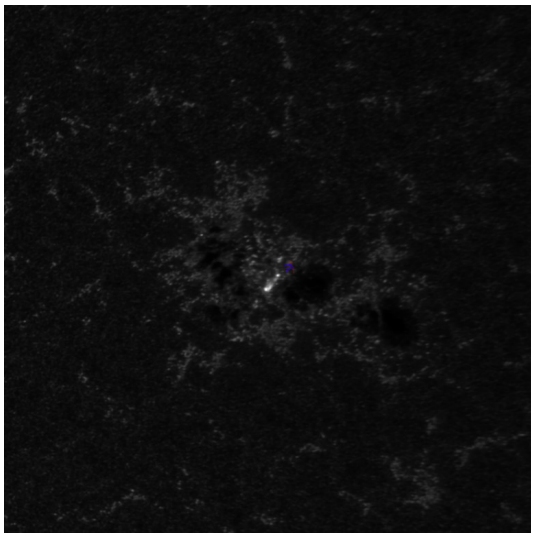

(d) 1 700 Å

Figure A.48: The same as in Figure A.25 but for the M5.1 solar flare on 2014 September 28 with the solar flare maximum at 02:58 UT.

A.3 Decay time

In the following figures, there are mean lightcurves of WLF points, residuum differences, and histograms of decay times for WLF points for all the detected WLFs. The intensity for mean light curves is normalized to the first point.

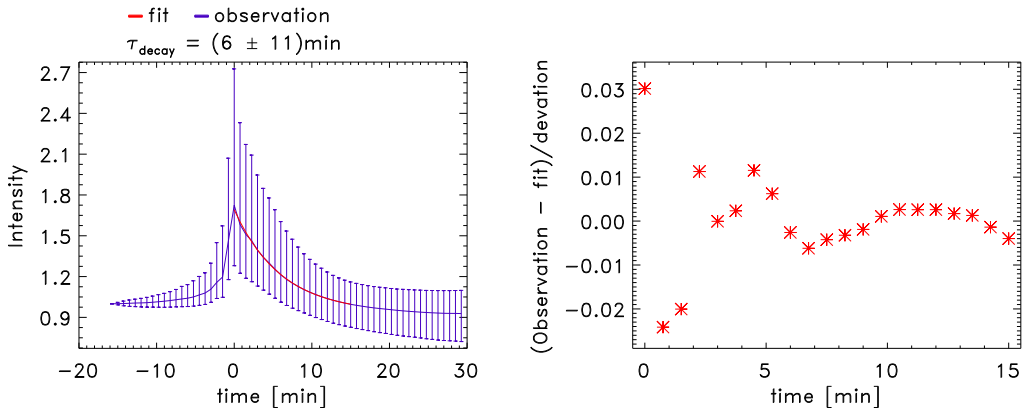

(a) Mean lightcurve of WLF points. (b) Residuum difference.

Figure A.49: Mean lightcurve and residuum difference for the X9.3 solar flare on 2017 September 06 with the solar flare maximum at 12:02 UT.

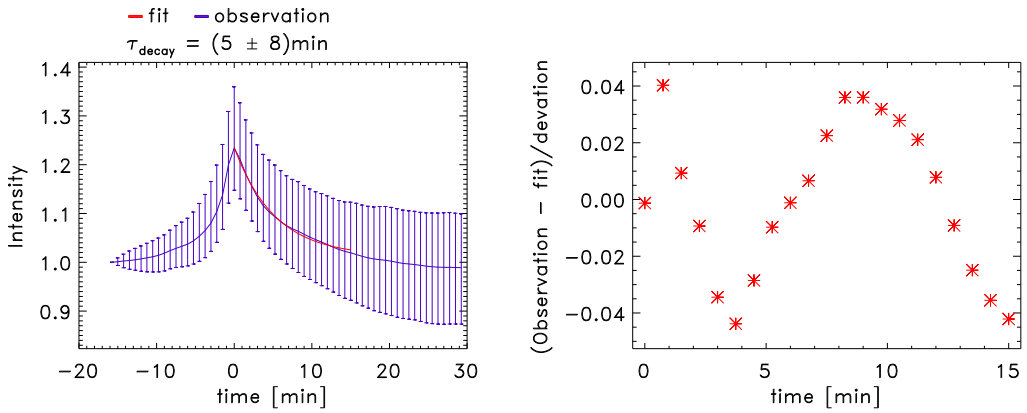

(a) Mean lightcurve of WLF points. (b) Residuum difference.

Figure A.50: Mean lightcurve and residuum difference for the X5.4 solar flare on 2012 March 07 with the solar flare maximum at 00:24 UT.

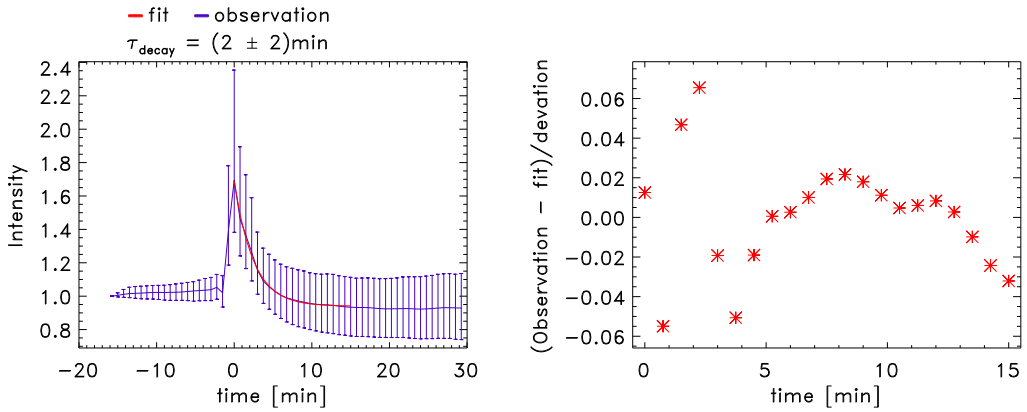

(a) Mean lightcurve of WLF points. (b) Residuum difference.

Figure A.51: Mean lightcurve and residuum difference for the X3.3 solar flare on 2013 November 05 with the solar flare maximum at 22:12 UT.

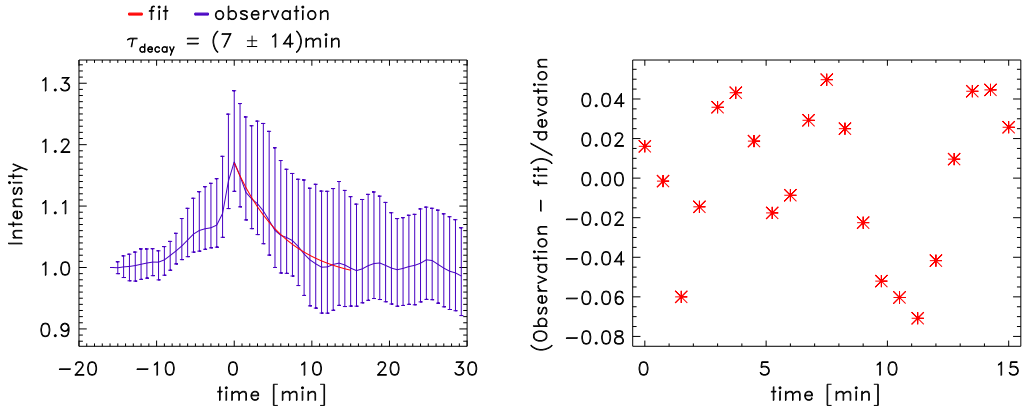

(a) Mean lightcurve of WLF points. (b) Residuum difference.

Figure A.52: Mean lightcurve and residuum difference for the X3.1 solar flare on 2014 October 24 with the solar flare maximum at 21:41 UT.

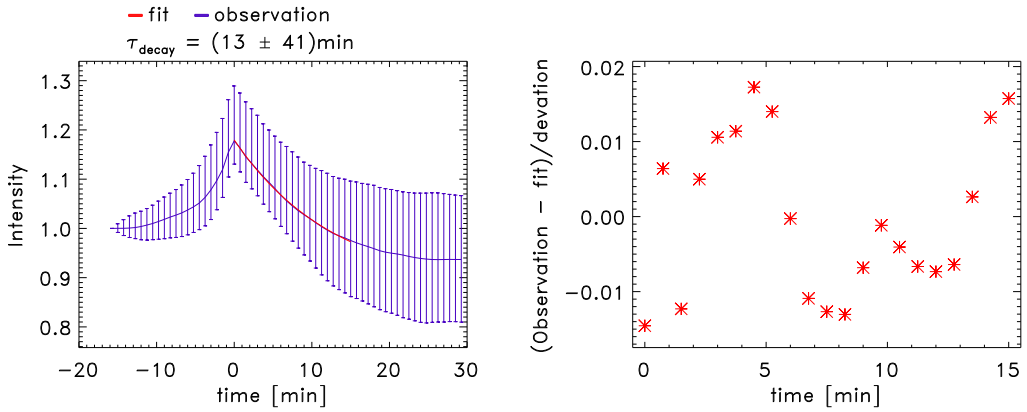

(a) Mean lightcurve of WLF points. (b) Residuum difference.

Figure A.53: Mean lightcurve and residuum difference for the X2.2 solar flare on 2011 February 15 with the solar flare maximum at 01:56 UT.

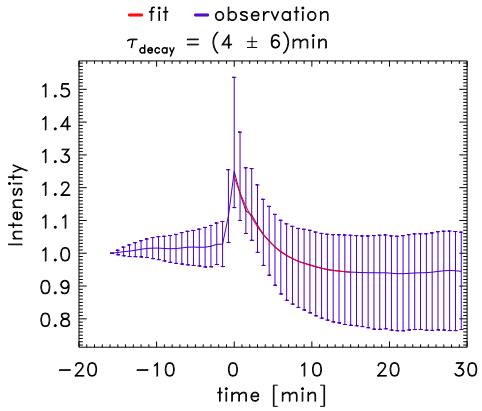

(a) Mean lightcurve of WLF points.

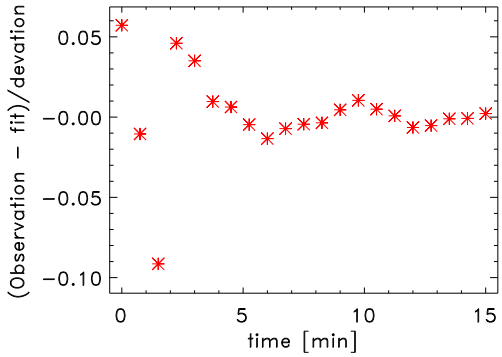

(b) Residuum difference.

Figure A.54: Mean lightcurve and residuum difference for the X2.1 solar flare on 2011 September 06 with the solar flare maximum at 22:20 UT.

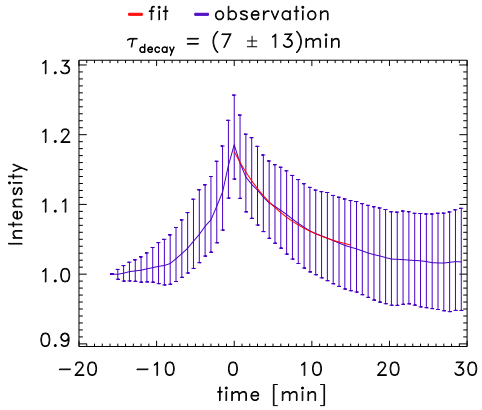

(a) Mean lightcurve of WLF points.

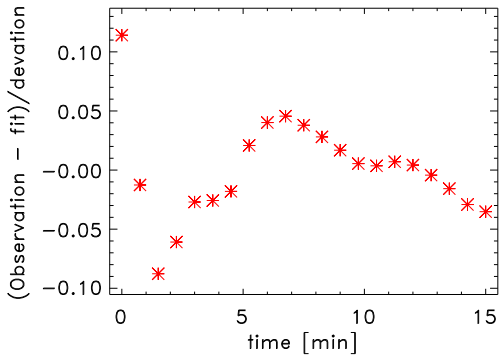

(b) Residuum difference.

Figure A.55: Mean lightcurve and residuum difference for the X2.0 solar flare on 2014 October 26 with the solar flare maximum at 10:56 UT.

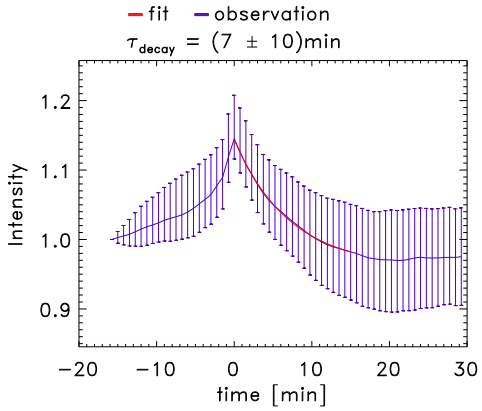

(a) Mean lightcurve of WLF points.

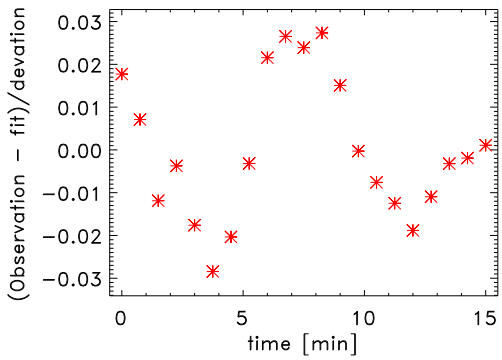

(b) Residuum difference.

Figure A.56: Mean lightcurve and residuum difference for the X1.8 solar flare on 2014 December 20 with the solar flare maximum at 00:28 UT.

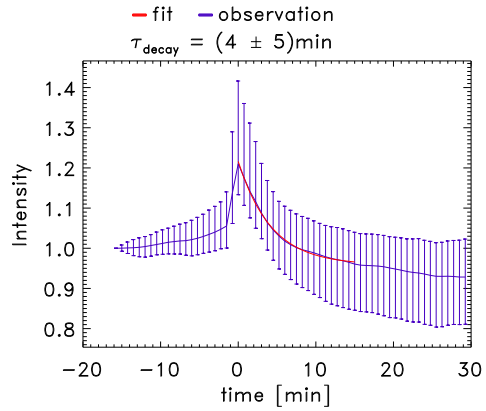

(a) Mean lightcurve of WLF points.

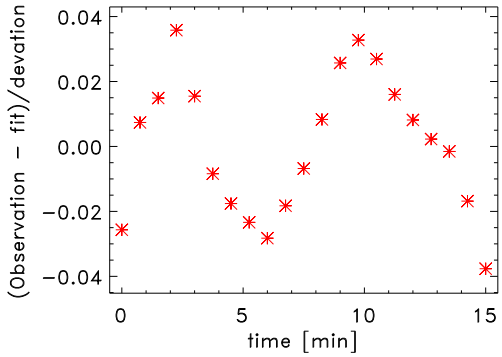

(b) Residuum difference.

Figure A.57: Mean lightcurve and residuum difference for the X1.8 solar flare on 2011 September 07 with the solar flare maximum at 22:38 UT.

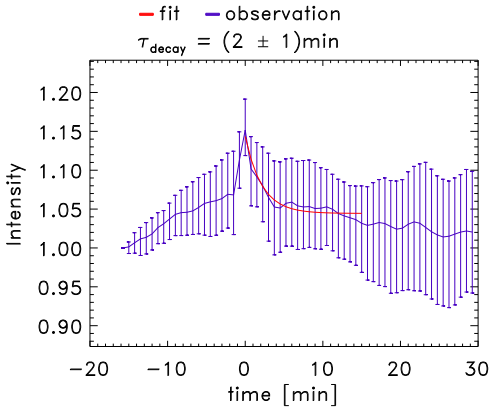

(a) Mean lightcurve of WLF points.

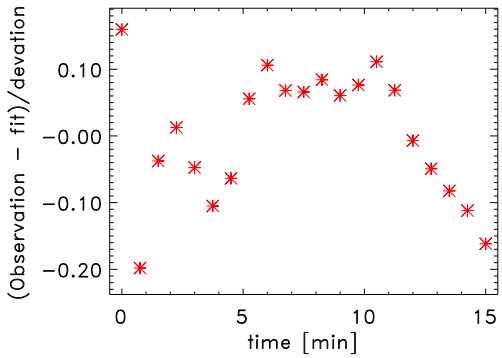

(b) Residuum difference.

Figure A.58: Mean lightcurve and residuum difference for the X1.6 solar flare on 2014 October 22 with the solar flare maximum at 14:28 UT.

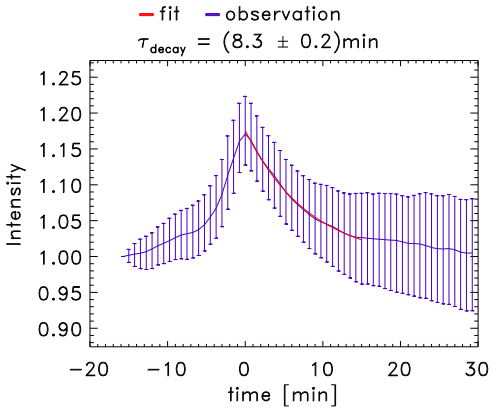

(a) Mean lightcurve of WLF points.

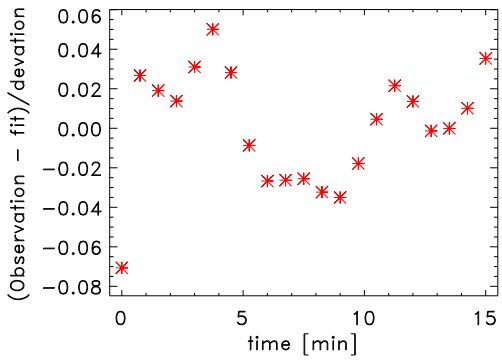

(b) Residuum difference.

Figure A.59: Mean lightcurve and residuum difference for the X1.3 solar flare on 2012 March 07 with the solar flare maximum at 01:14 UT.

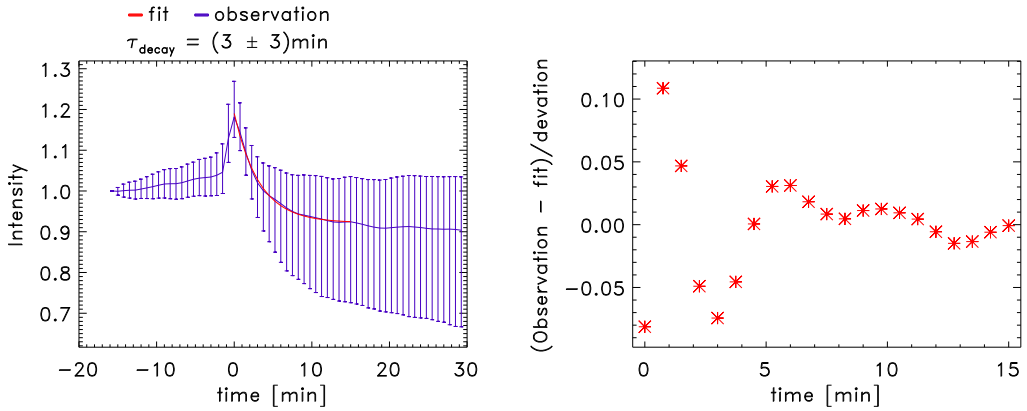

(a) Mean lightcurve of WLF points. (b) Residuum difference.

Figure A.60: Mean lightcurve and residuum difference for the M9.3 solar flare on 2011 July 30 with the solar flare maximum at 02:09 UT.

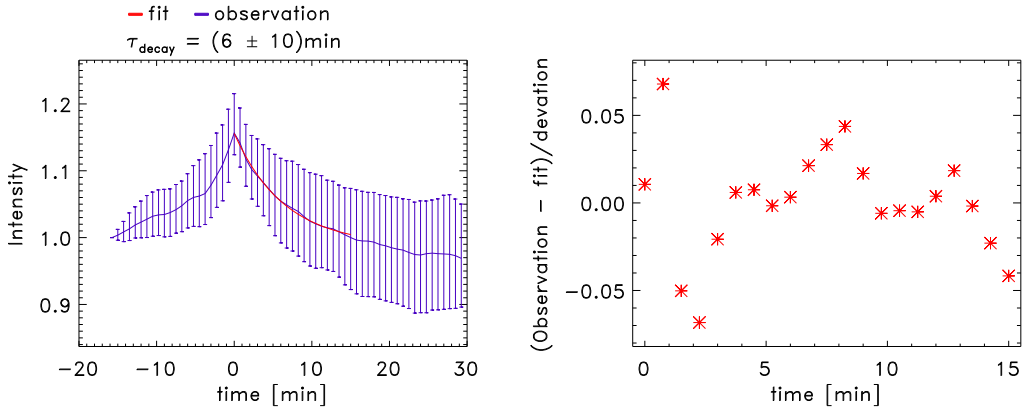

(a) Mean lightcurve of WLF points. (b) Residuum difference.

Figure A.61: Mean lightcurve and residuum difference for the M9.3 solar flare on 2011 August 04 with the solar flare maximum at 03:57 UT.

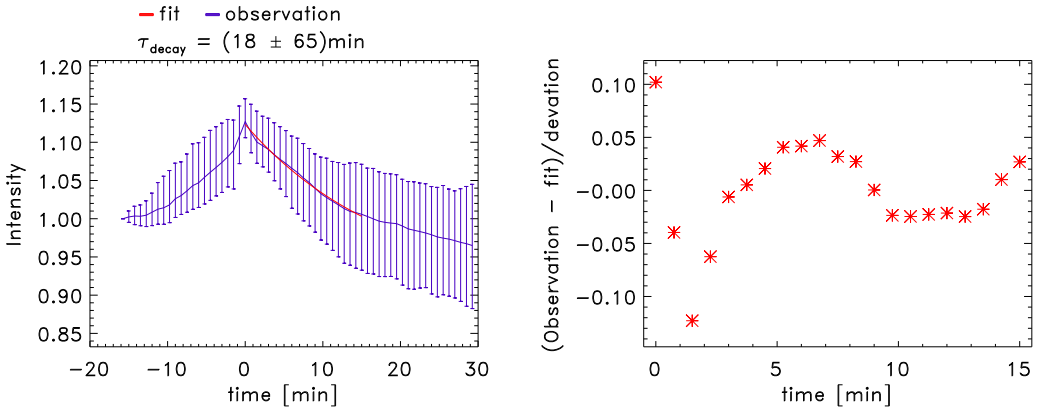

(a) Mean lightcurve of WLF points. (b) Residuum difference.

Figure A.62: Mean lightcurve and residuum difference for the M8.7 solar flare on 2014 October 22 with the solar flare maximum at 01:59 UT.

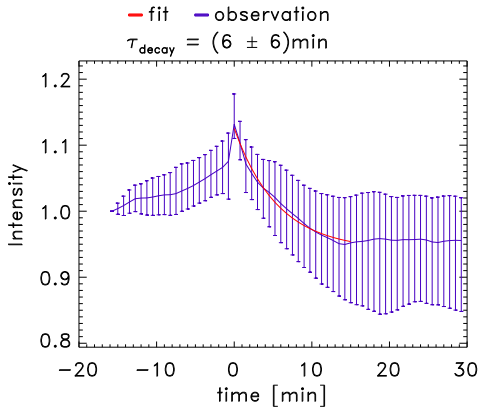

(a) Mean lightcurve of WLF points.

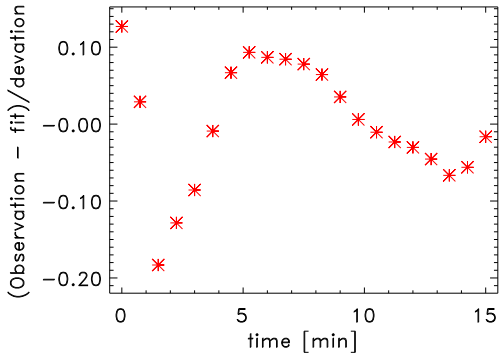

(b) Residuum difference.

Figure A.63: Mean lightcurve and residuum difference for the M7.9 solar flare on 2015 June 25 with the solar flare maximum at 08:16 UT.

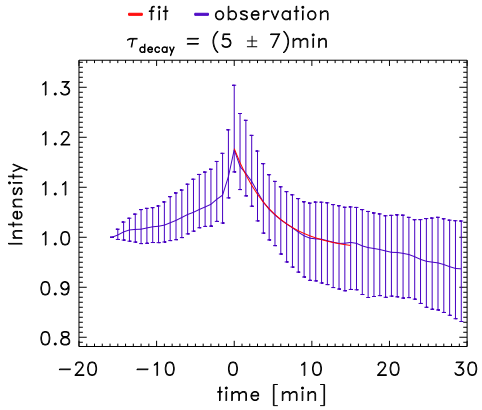

(a) Mean lightcurve of WLF points.

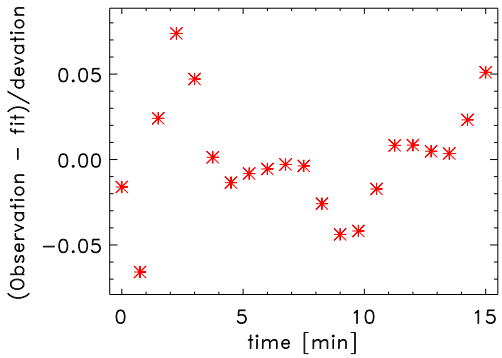

(b) Residuum difference.

Figure A.64: Mean lightcurve and residuum difference for the M7.2 solar flare on 2014 January 07 with the solar flare maximum at 10:13 UT.

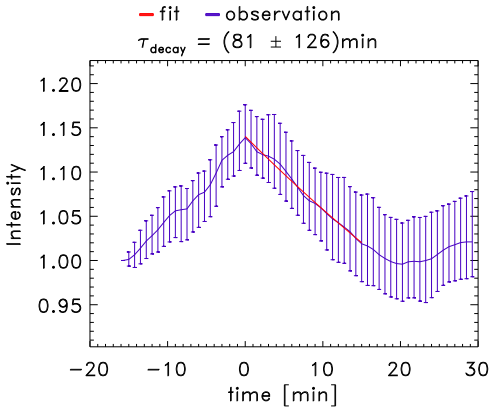

(a) Mean lightcurve of WLF points.

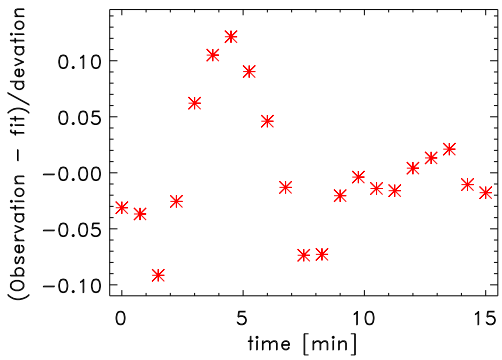

(b) Residuum difference.

Figure A.65: Mean lightcurve and residuum difference for the M7.1 solar flare on 2014 October 27 with the solar flare maximum at 00:34 UT.

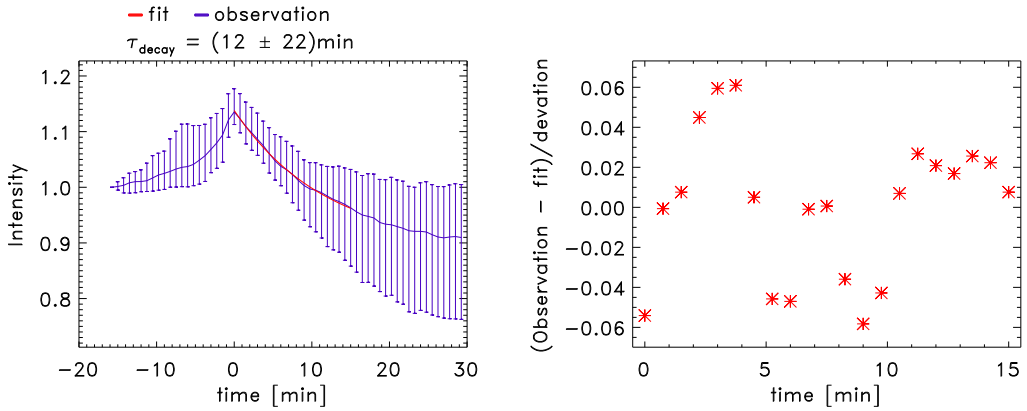

(a) Mean lightcurve of WLF points. (b) Residuum difference.

Figure A.66: Mean lightcurve and residuum difference for the M6.3 solar flare on 2012 March 09 with the solar flare maximum at 03:53 UT.

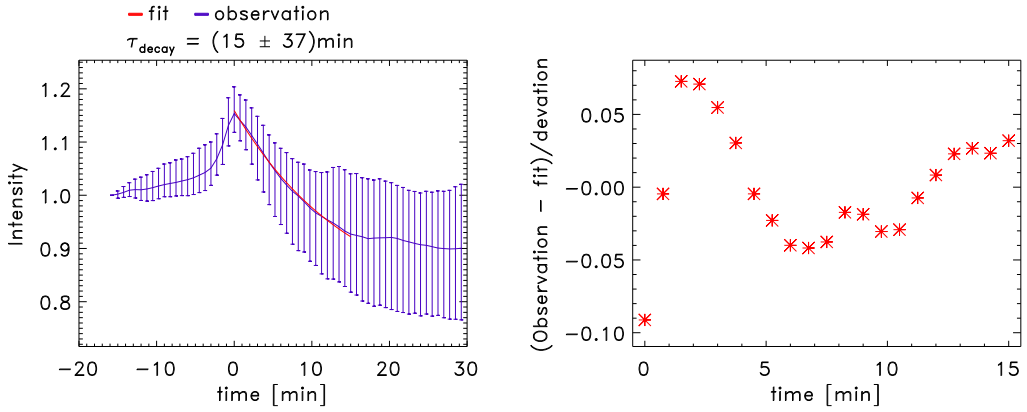

(a) Mean lightcurve of WLF points. (b) Residuum difference.

Figure A.67: Mean lightcurve and residuum difference for the M6.3 solar flare on 2013 November 01 with the solar flare maximum at 19:53 UT.

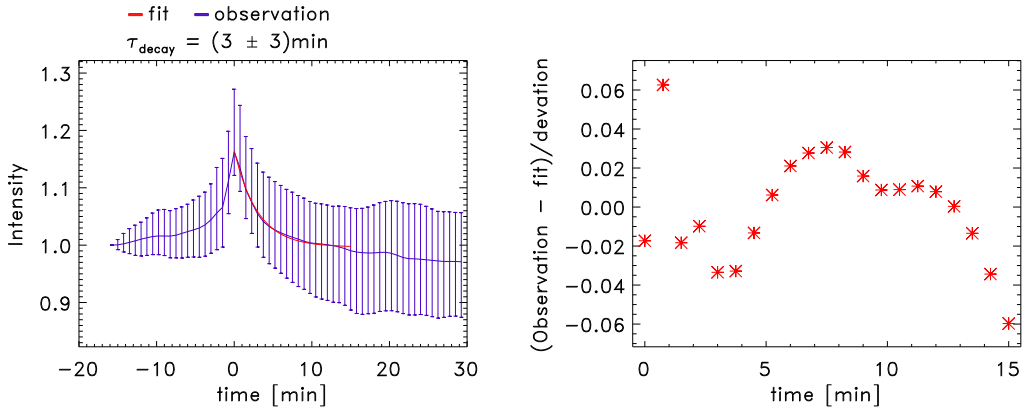

(a) Mean lightcurve of WLF points. (b) Residuum difference.

Figure A.68: Mean lightcurve and residuum difference for the M6.2 solar flare on 2012 July 05 with the solar flare maximum at 11:44 UT.

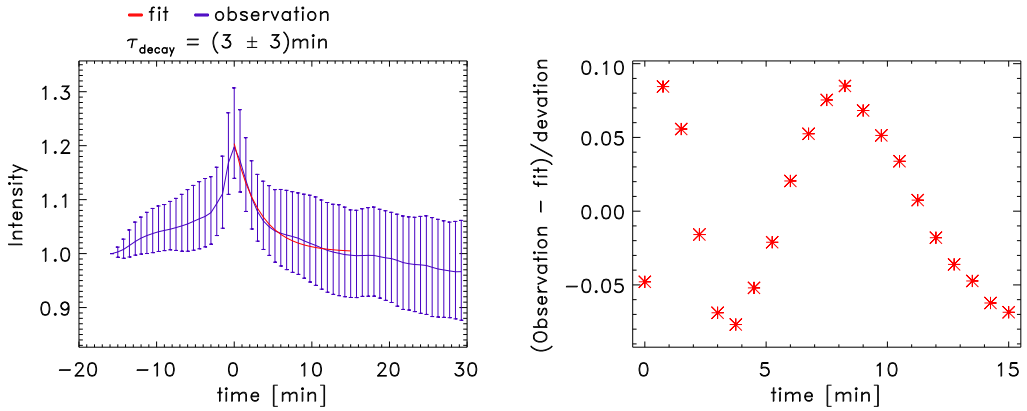

(a) Mean lightcurve of WLF points. (b) Residuum difference.

Figure A.69: Mean lightcurve and residuum difference for the M5.6 solar flare on 2015 August 24 with the solar flare maximum at 07:33 UT.

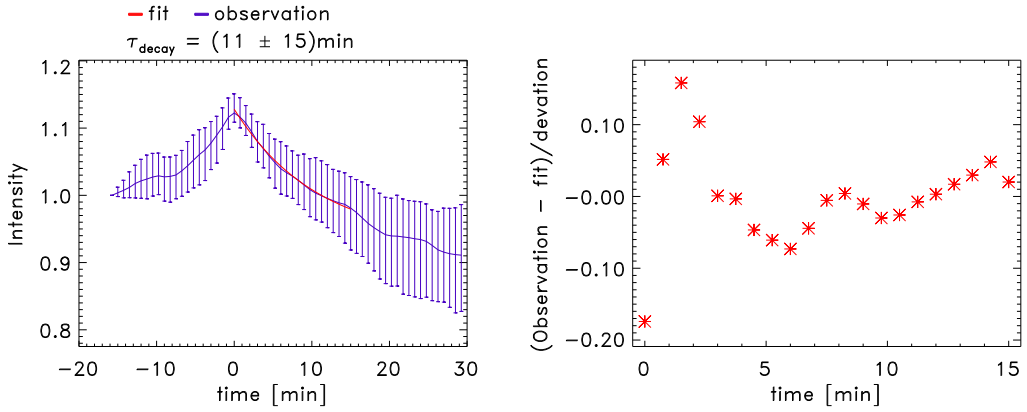

(a) Mean lightcurve of WLF points. (b) Residuum difference.

Figure A.70: Mean lightcurve and residuum difference for the M5.3 solar flare on 2011 September 06 with the solar flare maximum at 01:50 UT.

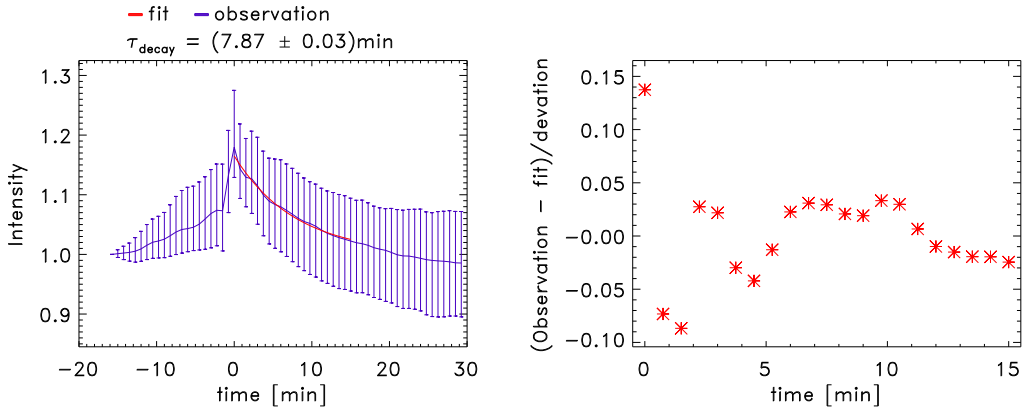

(a) Mean lightcurve of WLF points. (b) Residuum difference.

Figure A.71: Mean lightcurve and residuum difference for the M5.2 solar flare on 2014 February 04 with the solar flare maximum at 04:00 UT.

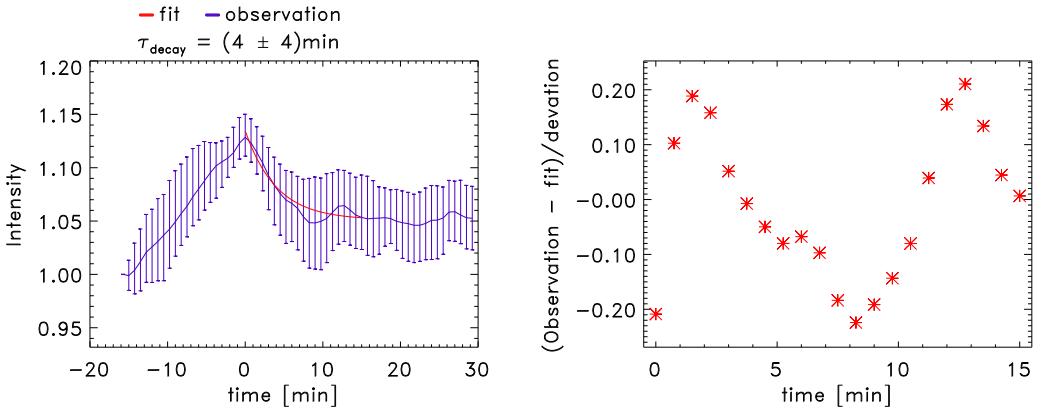

(a) Mean lightcurve of WLF points.

(b) Residuum difference.

Figure A.72: Mean lightcurve and residuum difference for the M5.1 solar flare on 2014 September 28 with the solar flare maximum at 02:58 UT.

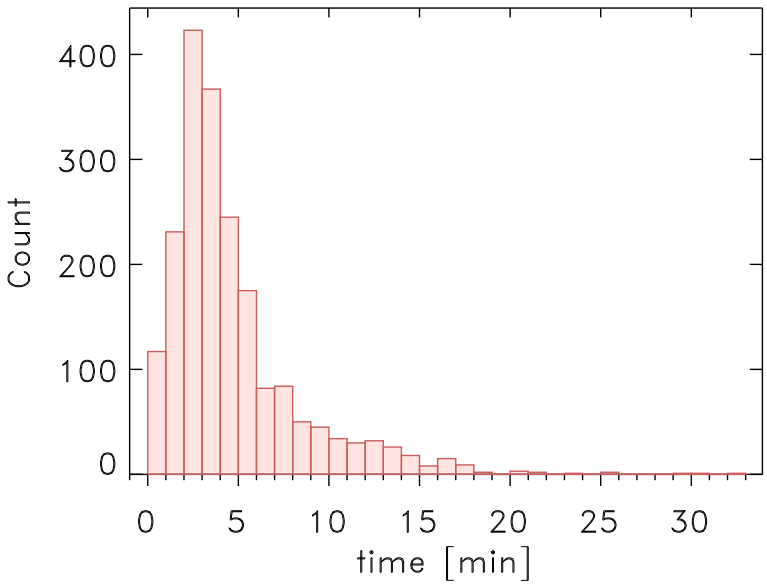

Figure A.73: Histogram of decay times of WLF points for the X9.3 solar flare on 2017 September 06 with the solar flare maximum at 12:02 UT.

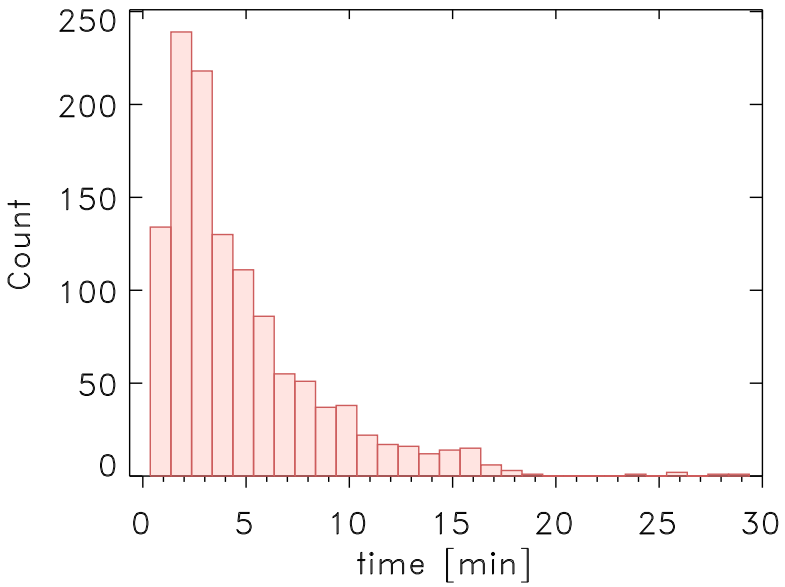

Figure A.74: Histogram of decay times of WLF points for the X5.4 solar flare on 2012 March 07 with the solar flare maximum at 00:24 UT.

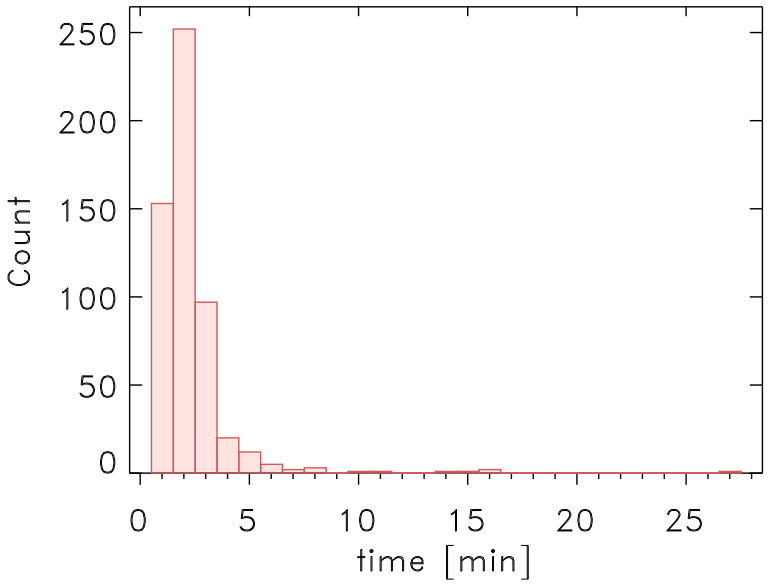

Figure A.75: Histogram of decay times of WLF points for the X3.3 solar flare on 2013 November 05 with the solar flare maximum at 22:12 UT.

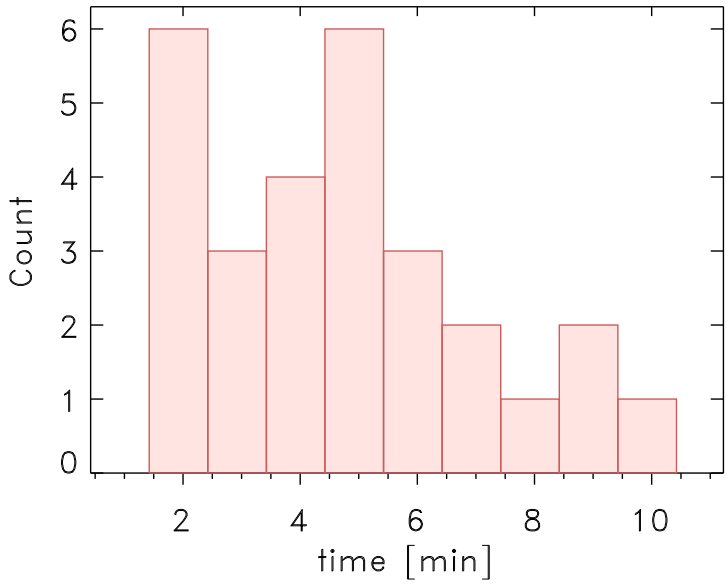

Figure A.76: Histogram of decay times of WLF points for the X3.1 solar flare on 2014 October 24 with the solar flare maximum at 21:41 UT.

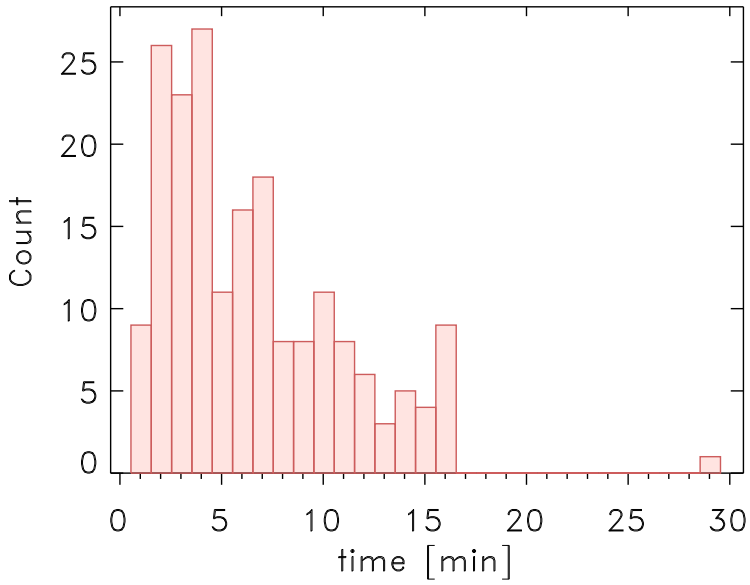

Figure A.77: Histogram of decay times of WLF points for the X2.2 solar flare on 2011 February 15 with the solar flare maximum at 01:56 UT.

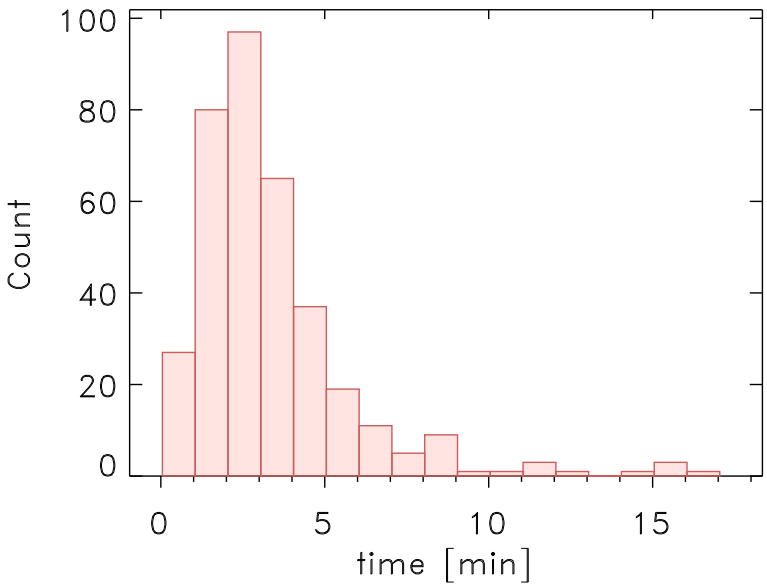

Figure A.78: Histogram of decay times of WLF points for the X2.1 solar flare on 2011 September 06 with the solar flare maximum at 22:20 UT.

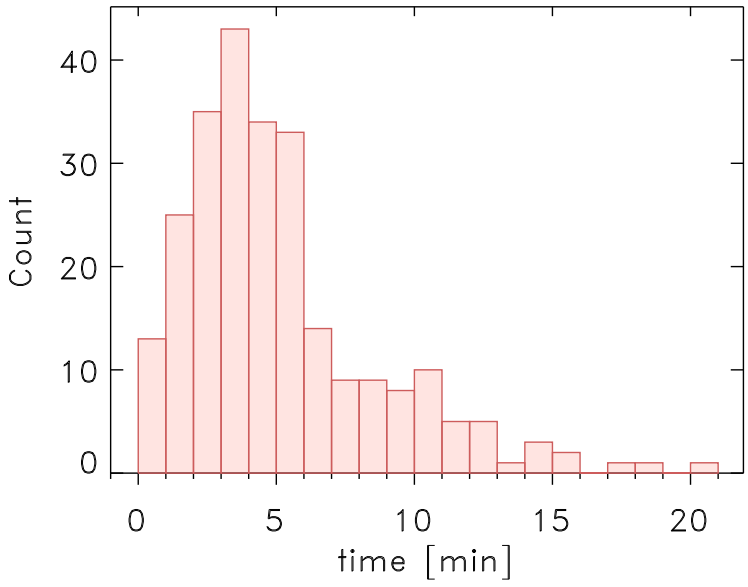

Figure A.79: Histogram of decay times of WLF points for the X2.0 solar flare on 2014 October 26 with the solar flare maximum at 10:56 UT.

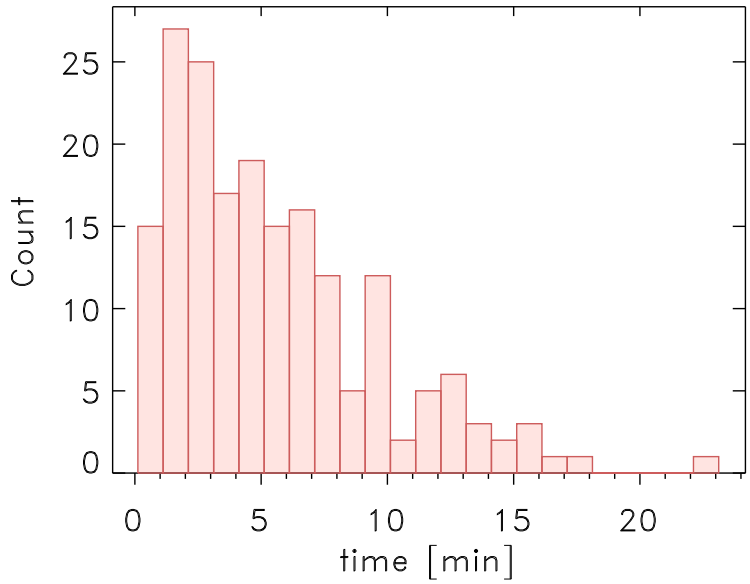

Figure A.80: Histogram of decay times of WLF points for the X1.8 solar flare on 2014 December 20 with the solar flare maximum at 00:28 UT.

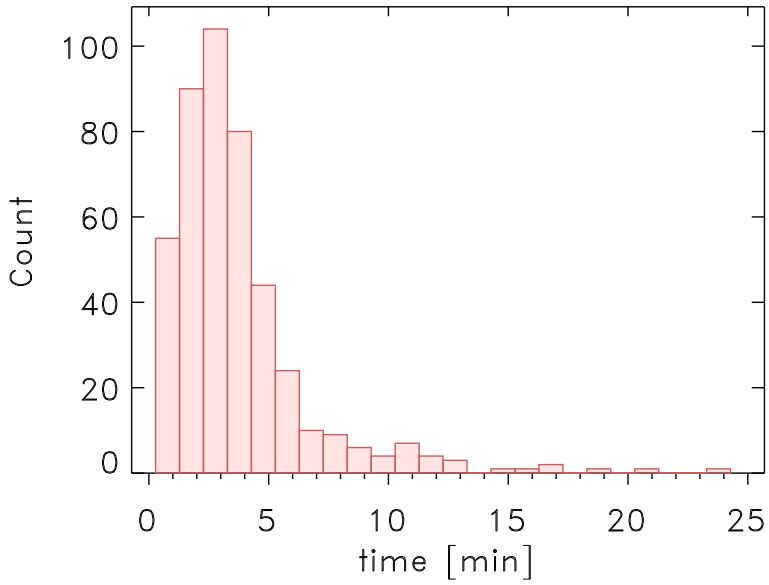

Figure A.81: Histogram of decay times of WLF points for the X1.8 solar flare on 2011 September 07 with the solar flare maximum at 22:38 UT.

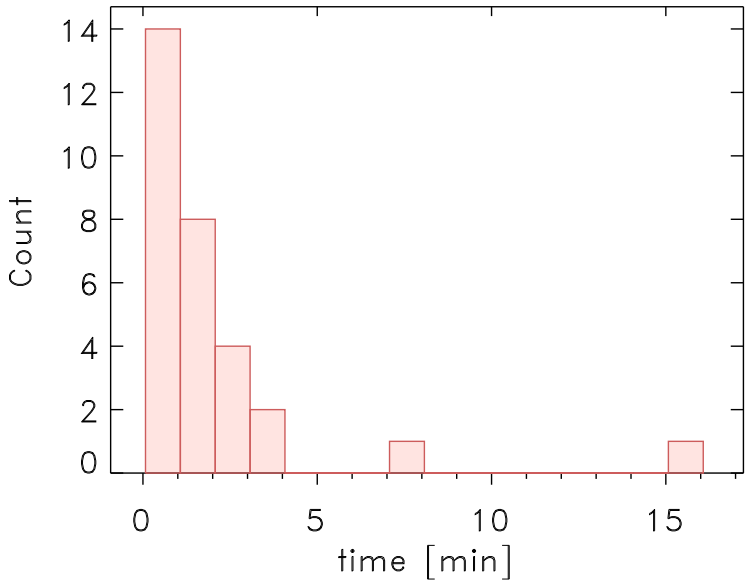

Figure A.82: Histogram of decay times of WLF points for the X1.6 solar flare on 2014 October 22 with the solar flare maximum at 14:28 UT.

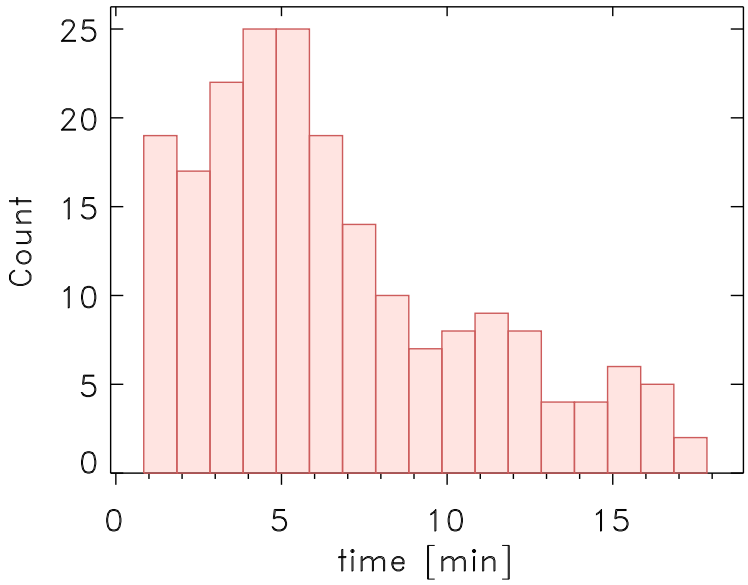

Figure A.83: Histogram of decay times of WLF points for the X1.3 solar flare on 2012 March 07 with the solar flare maximum at 01:14 UT.

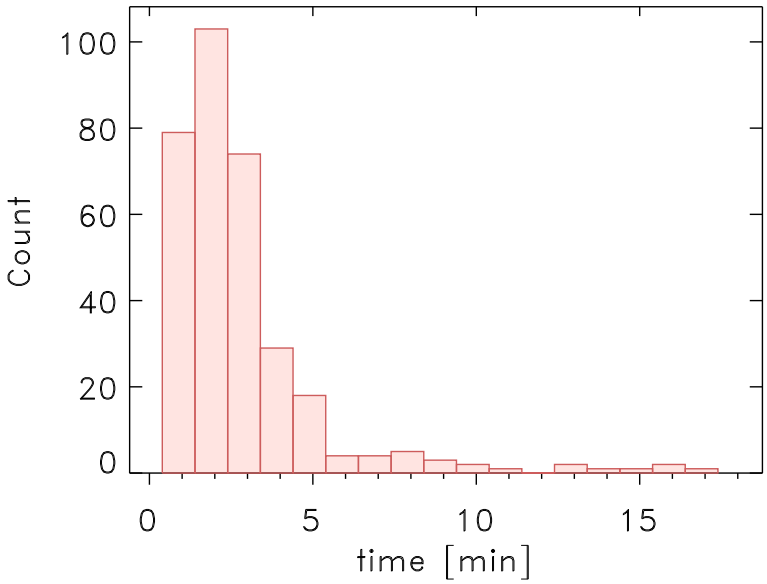

Figure A.84: Histogram of decay times of WLF points for the M9.3 solar flare on 2011 July 30 with the solar flare maximum at 02:09 UT.

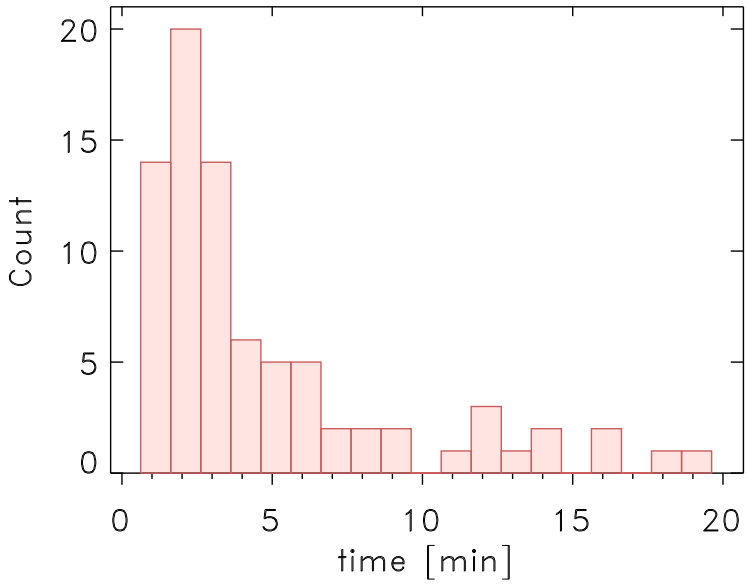

Figure A.85: Histogram of decay times of WLF points for the M9.3 solar flare on 2011 August 04 with the solar flare maximum at 03:57 UT.

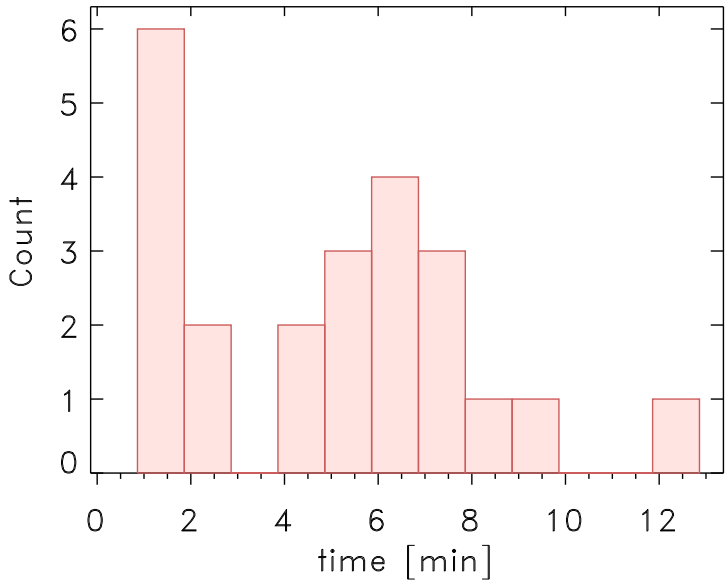

Figure A.86: Histogram of decay times of WLF points for the M8.7 solar flare on 2014 October 22 with the solar flare maximum at 01:59 UT.

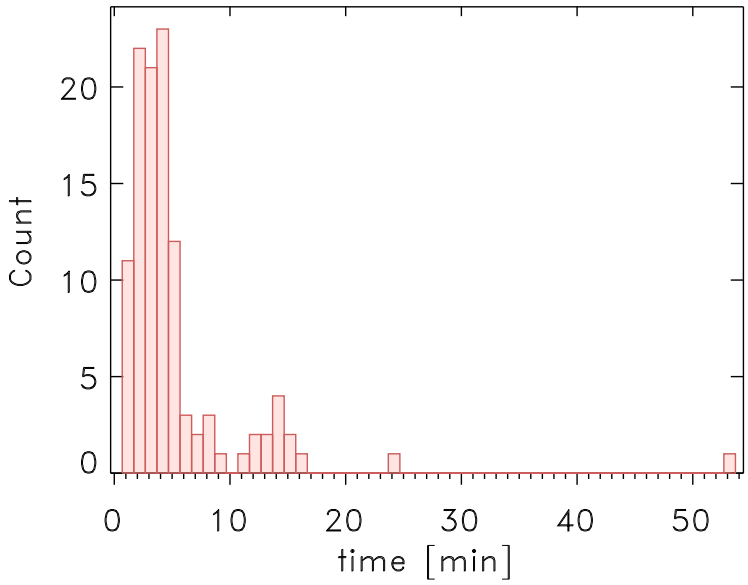

Figure A.87: Histogram of decay times of WLF points for the M7.9 solar flare on 2015 June 25 with the solar flare maximum at 08:16 UT.

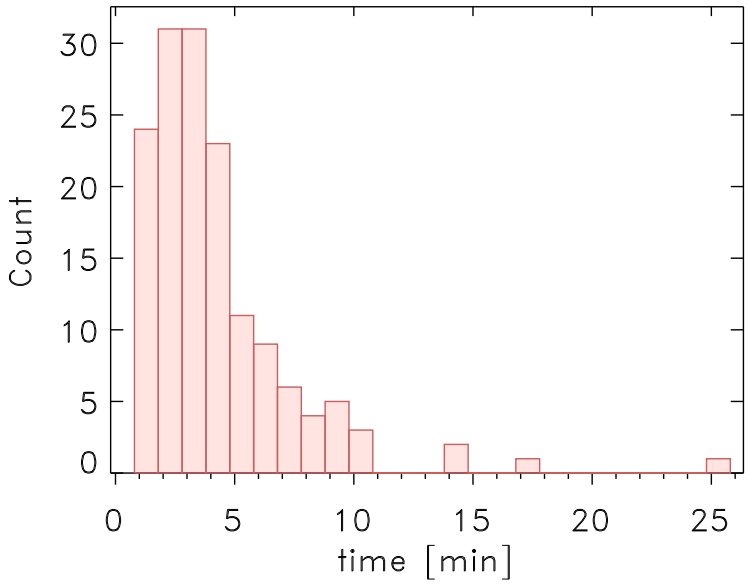

Figure A.88: Histogram of decay times of WLF points for the M7.2 solar flare on 2014 January 07 with the solar flare maximum at 10:13 UT.

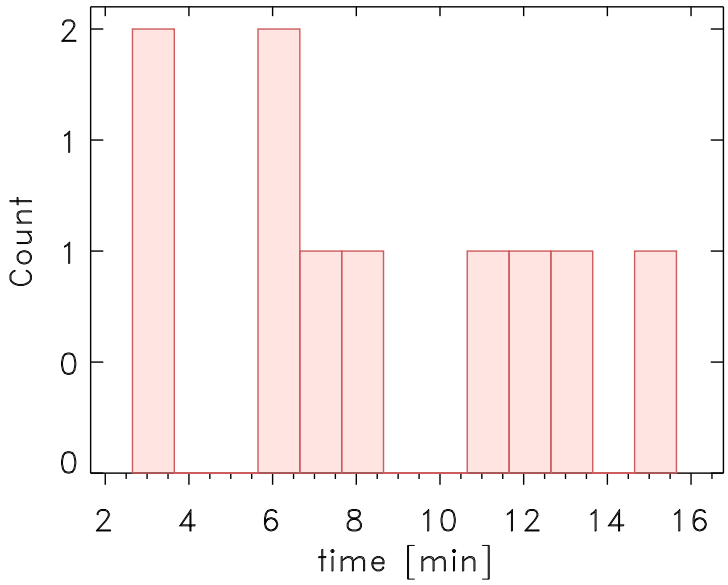

Figure A.89: Histogram of decay times of WLF points for the M7.1 solar flare on 2014 October 27 with the solar flare maximum at 00:34 UT.

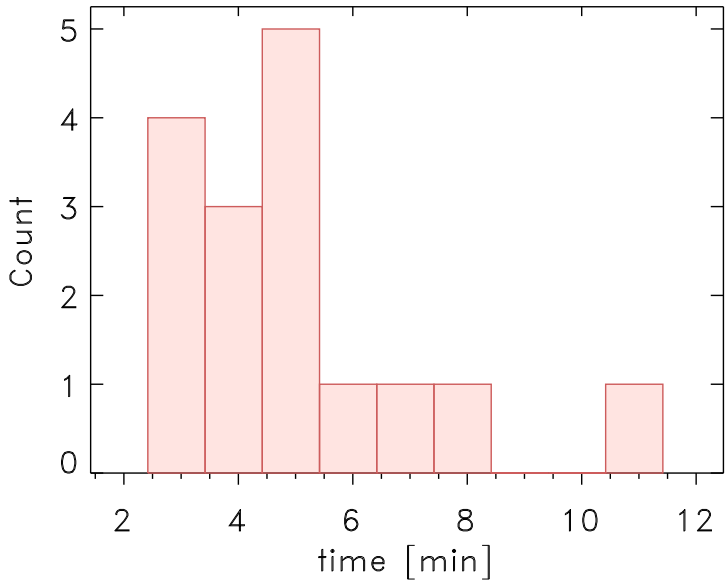

Figure A.90: Histogram of decay times of WLF points for the M6.3 solar flare on 2012 March 09 with the solar flare maximum at 03:53 UT.

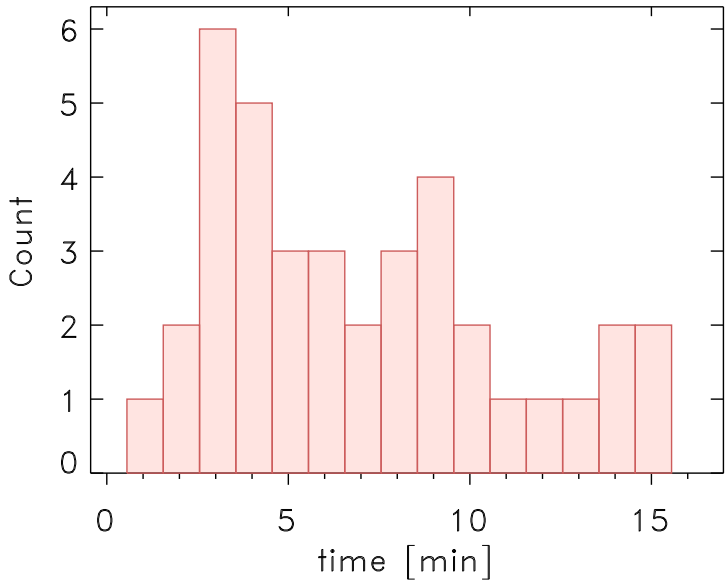

Figure A.91: Histogram of decay times of WLF points for the M6.3 solar flare on 2013 November 01 with the solar flare maximum at 19:53 UT.

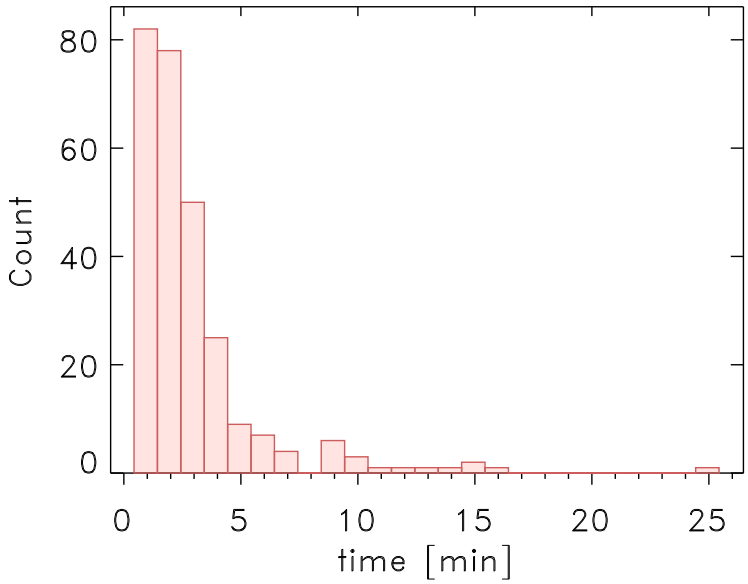

Figure A.92: Histogram of decay times of WLF points for the M6.2 solar flare on 2012 July 05 with the solar flare maximum at 11:44 UT.

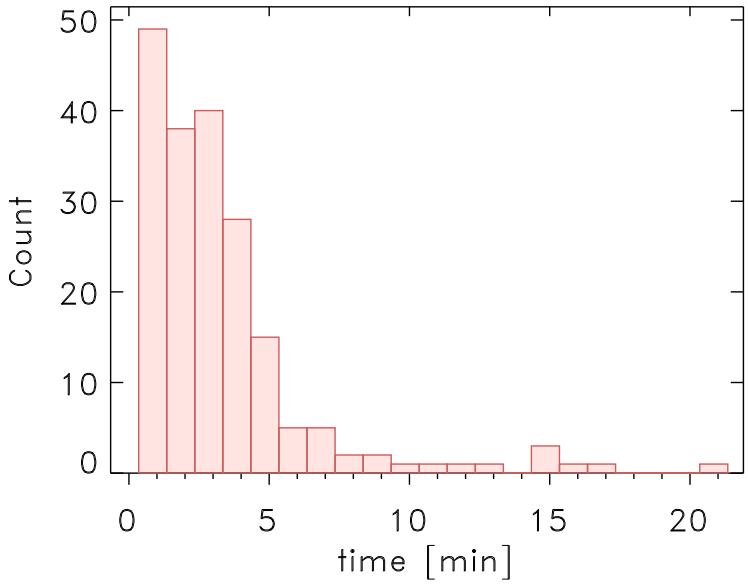

Figure A.93: Histogram of decay times of WLF points for the M5.6 solar flare on 2015 August 24 with the solar flare maximum at 07:33 UT.

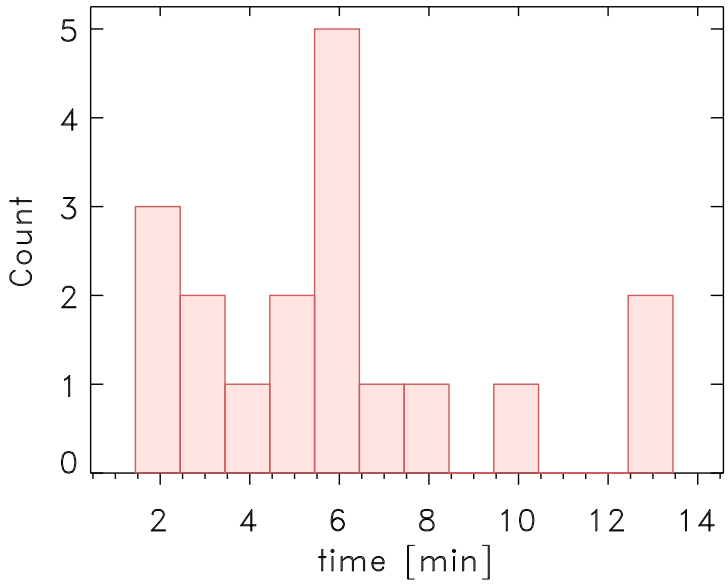

Figure A.94: Histogram of decay times of WLF points for the M5.3 solar flare on 2011 September 06 with the solar flare maximum at 01:50 UT.

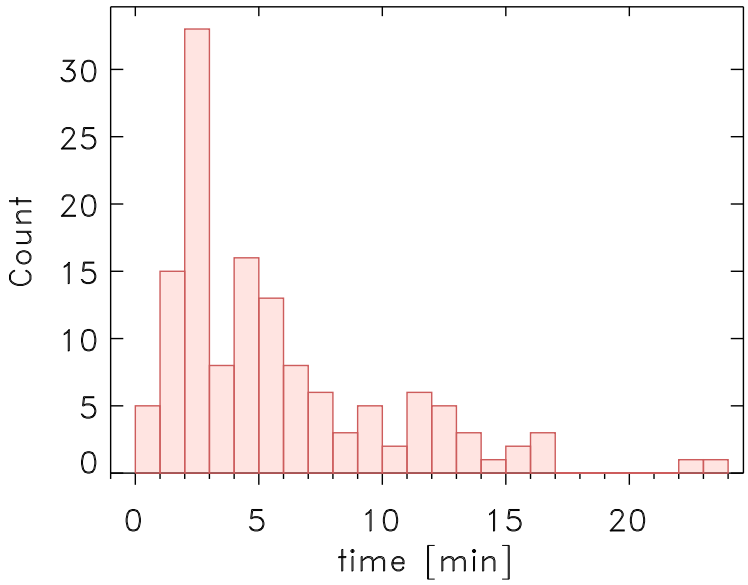

Figure A.95: Histogram of decay times of WLF points for the M5.2 solar flare on 2014 February 04 with the solar flare maximum at 04:00 UT.

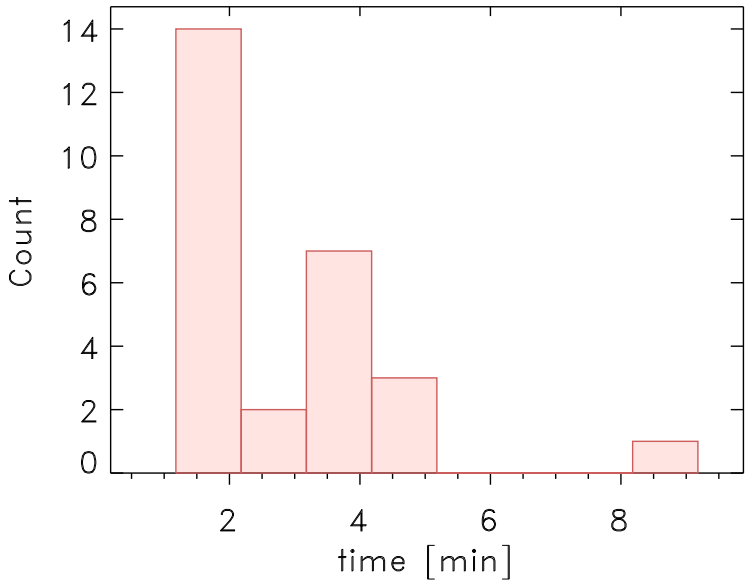

Figure A.96: Histogram of decay times of WLF points for the M5.1 solar flare on 2014 September 28 with the solar flare maximum at 02:58 UT.